STATISTICAL ANALYSIS OF DATA FROM THE SIMRAD MS70 MULTIBEAM SONAR

by

ARNE JOHANNES HOLMIN

THESIS

for the degree of

MASTER OF SCIENCE

(Master of statistics - data analysis)

UNIVERSITETET I BERGEN
Det matematisk-naturvitenskapelige fakultet

July 2008

Contents

Chapter 1

Introduction.

The aim for this master thesis is to do the ground work for a statistical analysis of four dimensional data, (three spatial dimensions and time), of fish schools, registered by the Simrad scientific multibeam sonar MS70, owned by the Institute of Marine Research (IMR) in Bergen, Norway. The sonar emits high frequent sound in $25 \cdot 20$ narrow beams from an array of transducers, as illustrated in Figure 1.1, and observes the echo from objects in the insonifying volume.

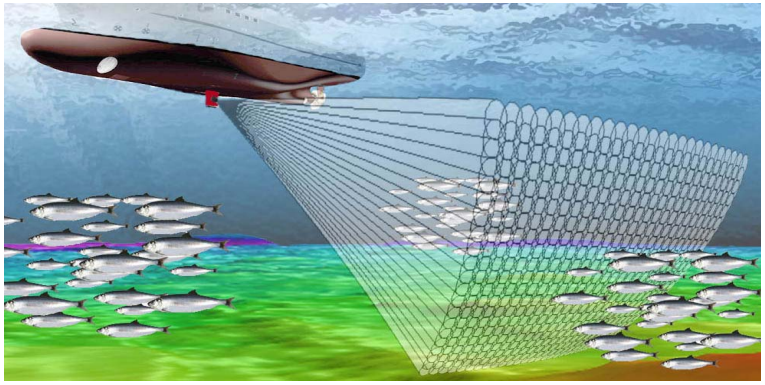

Figure 1.1: The 500 beams from the MS70 sonar. (Figure borrowed from "Prosedyre for operering av multistrålesonar MS70", by the Institute of Marine Research, Bergen, Norway.)

There are many advantages with multibeam sonars such as MS70, compared to ordinary echo sounders. One is that the sonars emit sound to the side of the research vessel, as seen in Figure 1.1, while echo sounders emit sound downwards. This allows for a larger sampling volume than for echo sounders, because the sea floor may restrict the sampling volume of the echo sounder to a larger degree than the sampling volume of the sonar. The insonifying volume of MS70 for the particular survey considered in this thesis, is a 45° by 60° segment of a sphere of radius approximately 500 meters. This means that we can observe schools typically at a distance 300 meters from the research vessel, which also reduces the problem of school avoidance. This problem was documented by (Gerlotto et al., 1999), where the density of fish schools at distances in the range $(30, 60)$ meters from a multibeam sonar, was almost twice the density in the range $(0, 30)$ meters.

The most obvious advantage however, is that the MS70 provide a series of three dimensional data sets in time, allowing for four dimensional observation of fish schools. This opens for a higher degree of reliability in both biomass estimation and school characterization. Hopefully there is enough information in data from a school observed by the MS70, to identify both the species and the number of fish to some degree of certainty.

In this thesis we consider two complementary approaches to the analysis. The first one is the individual approach (1), where we seek to fully describe the acoustic signal from one single fish, and then generalize to n fish. The second is the group level approach (2), involving statistical methods for characterizing the observed data, and the development in time of the data.

(1) - Individual approach.

The aim for the individual approach is to use acoustic theory to predict and explain the expected value and variation in the data values observed by the MS70 sonar. As a basis and inspiration for (1), we consider mathematical models for fish schools, called individual based models (IBM), consisting of a set of behaviour rules for individual fish. The first IBM was presented by (Parr, 1927), but more a important references is (Huth and Wissel, 1992), in which the movements of fish schools of 8 individuals are simulated, based on an IBM. The basic concept of IBMs is that the space around a fish is divided into four zones, in which a second fish affects the behaviour of the first fish. These are named the repulsion zone (a), the alignment zone (b), the attraction zone (c) and the searching zone (d), with increasing ranges from the reference fish. In simulations done by (Reynolds, 1987) the zone of alignment or parallel orientation, is replaced by a zone of velocity matching. A mathematical model that utilizes behaviour rules of this kind, is an IBM.

A great challenge is to link the specifications of the IMBs to the macroscopic properties of the fish school. In (Mirabet et al., 2007) the impact on school structure of different specifications for IBMs, were analyzed. The strength of repulsion, alignment and attraction were modeled as functions of distance from the fish, and 5 different sets of specifications of these functions were used to simulate 100 fish. The spatial structure of the schools were examined, and the results showed a significant impact on spatial structure from the different sets of functions. However, the sizes of fish schools studied or simulated using IBMs, seldom exceed 100 fish, which are far from the sizes of real fish schools. The school treated in this thesis for instance, may consist of several hundred thousand fish, so it is clear that the link between IBMs and large schools observed by multibeam sonars is not well understood. An effort on examining the link between

individual behaviour, and group-level properties, and encourage researchers to further explore this link, is done in (Parrish et al., 2002)

Our focus in this thesis will not be on IBMs, but rather on the acoustic signal scattered back to the receiver from individual fish. We still bear in mind the behaviour zones (a), (b), (c) and (d), which define an expected volume occupied by one fish in a school of a certain species. The degree of alignment of a species might also be possible to detect, through variables reflecting the parallel orientation of the fish in the school, and the will of the school to move in one direction (the determination of the school).

(2) - Group level approach.

By the second approach we seek to describe the properties of the school by variables reflecting its shape, movement, internal structure and development of shape and internal structure over time. Some preliminary investigations on school size and shape were performed by (Gerlotto et al., 1999). The results showed significant differences between the variables L_S/W_S and L_S/H_S, (where L_S, W_S and H_S are the mean length, width and height of a school), of fish schools observed in the Adriatic sea, and in the Catalan sea. Schools in the Adriatic sea were flatter and longer, and also had significantly larger volume. These variables and several others will be discussed as variables characterizing fish schools, in chapter 7, "Statistical analysis".

Connecting the approaches (1) and (2) is an important issue in the thesis, and it is our belief that many results of the statistical analysis rely on the results in the analysis of backscattering from individual fish. In particular the variance in the data from schools demand investigation on individual backscattering for proper interpretations. We also consider the expected acoustic signal from a single fish, and further generalized to n fish, to get an idea of which data values are to be expected from a school of a certain species. As the fish are generally seen from the side, the orientation of the fish has great impact on the individual and mean signal from schools, which is important in biomass estimation. We take orientation into account in the individual based analysis, and in the group level analysis, and a promising method might be to study the development of the signal from parts of schools over time. Rapid changes in the signal from a segment of a school is most likely to be an indication on rapid changes in the mean orientation of the fish in that segment, rather than fish leaving or joining the segment.

Contents of chapters.

Prior to the statistic analysis we do quite an extensive analysis, in order to represent the data in a three dimensional system of elementary unit volumes, called voxels, and transform these voxels into a global coordinate system, and finally into a coordinate system for the school. Some noise filtering is also required, because of frequent instrument noise. The thesis consists of 9 chapters, and we now briefly present the contents of the chapters:

Chapter 2, "Relevant acoustics", presents the acoustic variables and formulas used in later chapters, and can be seen as a chapter aiming to give the necessary acoustic background, rather than a part of the statistical analysis. For readers familiar to acoustic theory, the chapter may be skimmed, using it as a reference when acoustic properties are implemented later in the thesis.

Chapter 3, "Materials", introduces the research vessel and the properties of the MS70 sonar.

Chapter 4, "Interpretation of data", establishes the system of voxels used to represent the output from the MS70 sonar, and defines and calculates the volumes of the voxels, and the midpoints of the voxels subject to the refraction of sound in sea water.

Chapter 5, "Noise", briefly presents different types of noise encountered in the data, and especially treats high intensity instrument noise which appears quite frequently. An algorithm for removing this type of noise is established and used on the data.

Chapter 6, "Backscattering from individual fish", is the major chapter in the thesis, and traces the acoustic signal from the transducer to the fish, and back to the transducer for a fish of random position, size and orientation. The results are generalized to many fish, and interference effects between the individual acoustic signals are taken into account. Finally, the acoustic signal received in specific time intervals are simulated, and compared to the real data.

Chapter 7, "Statistical analysis", contains analyses of the data as transformed into the coordinate system of the school. The chapter concerns preliminary spatial statistical methods for characterization, involving principal component analysis, analysis of variation in the data, autocorrelation along beams, and analysis of the total acoustic backscattering from the school, all as variables in time.

Chapter 8, "Results", presents the results of chapter 7.

Chapter 9, "Discussion and future work", discusses the methods and results presented, as well as ideas for work that fell outside of the time frame of this thesis.

Appendix A, "Rotation matrices", presents the matrices used to transform point vectors from one coordinate system to another coordinate system, rotated around a mutual origin.

Appendix B, "Notation", lists all variables used in the text, sorted by the chapters in which the variables appear.

Appendix C, "Histograms of the different parts of the sonar equation from simulations", displays 7 histograms showing the randomness in different variables linked to the acoustic intensity from a fish, from simulations done in chapter 6.

The large amounts of data treated requires efficient programming, both to reduce the time usage and to comply with the memory limitations of the computer. For the survey treated in this there are 1319 voxels i each beam, resulting in $25 \cdot 20 \cdot 1319 = 659500$ values per time step. The school we will concentrate on is observed during 12 time steps (called pings), giving a total of almost 8 million values.

Chapter 2

Relevant acoustics.

In this chapter we present all acoustic concepts and formulas that are used in the rest of the thesis. The theory presented will mainly be used in chapters 4 and 6.

2.1 Basic acoustics.

A source radiating sound into a medium generates a pressure field in the medium that fluctuates with frequencies depending on the radiated sound and the acoustic properties of the medium. As the source vibrates, kinetic energy is transfered to the immediate surroundings so that the closest molecules are either pushed closer to its neighbours, or pulled away from its neighbours, according to the motion of the source. This generates a fluctuating pressure field close to the source, which in the next time step is compensated by longitudinal motion of molecules next to the directly affected molecules. In this way the sound propagates through the medium, and we can describe this propagation by the pressure $p(\mathbf{X}, t)$ at the point $\mathbf{X}$ in space at time t.

A sound wave moving through a medium will usually be spherical, analogous to the spherical surface rings in water after a jumping fish. Locally however, the wave can be regarded as plane, with propagation only in one direction. We express these two waves mathematically as

$$p(x,t) = Ae^{-i(\omega t - kx)} \qquad (plane) \tag{2.1}$$

and

$$p(r,t) = \frac{A}{r}e^{-i(\omega t - kr)} \qquad (spherical). \tag{2.2}$$

Here $\omega = 2\pi f$ is the angular frequency of the wave (f being the frequency), $k = \frac{2\pi f}{c}$ is the wave number, c is the speed of sound in the medium and r and x are in spherical and cartesian coordinates respectively. We also have the obvious relation $ck = \omega$. We name the complex pressure ampluitude of an acoustic wave P, and for the plane and spherical wave we have that $P = A$ and $P = A/r$ respectively. The complex expression can not be interpreted directly, and the real part of (2.1) and (2.2) must be used for all physical interpretations.

2.2 Acoustic intensity.

To derive an expression for acoustic intensity, we need to define specific acoustic impedance z, which is a measure of the acoustic pressure needed to give particles in a medium the speed u:

$$z \equiv \frac{p}{u}. \tag{2.3}$$

An important equation in acoustics is the linear Euler's equation, which is the acoustic analogy to Newton's second law in classical mechanics. It links the pressure gradient to the particle acceleration, and can be used to express u for a plane wave in the x-direction. For a plane wave it can be expressed as

$$-\frac{\partial p\,(x,t)}{\partial x} = \rho_0 \frac{\partial u(x,t)}{\partial t},$$

where ρ_0 is the equilibrium particle density (mass per volume). Used on (2.1), Euler's linear equation gives

$$ikAe^{-i(\omega t - kx)} = \frac{\rho_0}{-i\omega}u(x,t)$$

$$u(x,t) = \frac{A}{\rho_0 c} e^{-i(\omega t - kx)},$$

where we have assumed that $u(x,t)$ has the same mathematical form as $p(x,t)$. It is then easy to see that the specific acoustic impedance for a plane harmonic wave is

$$z = \frac{p}{u} = \rho_0 c, \tag{2.4}$$

where $\rho_0 c$ is the product of equilibrium density and speed of sound. For the spherical wave more thermodynamic and fluid dynamic equations are needed to find the particle speed u, (the equation of state and the equation of continuity). We will only present the end result here, noting that the radial propagation makes z complex:

$$z(r) = \rho_0 c \cos\phi_r e^{-i\phi_r}, \tag{2.5}$$

$$\cos\phi_r = \frac{kr}{\sqrt{1+(kr)^2}} \qquad \cot\phi_r = kr.$$

We now have the tools needed to derive the expression of acoustic intensity I, which is the power of the acoustic wave divided by the area on which work is done by the wave, averaged over one period $T = f^{-1}$. In mechanics power is expressed as $F \cdot u$, where F is the force and u is the speed, while pressure is defined as the ratio of force and the area on which the force works. Considering the specific acoustic impedance for a plane wave (2.4), we thus get

$$I = \frac{1}{T}\int_0^T pu \cdot dt = \frac{1}{T}\int_0^T \frac{p^2}{\rho_0 c} \cdot dt = \frac{P^2}{2\rho_0 c}. \tag{2.6}$$

This expression is valid both for plane and spherical waves. For a spherical wave I will naturally decay by the square of distance, while a plane wave will have constant acoustic intensity $I = A^2/2\rho_0 c$ (confronting (2.1) and (2.2)).

2.3 Pressure field from a simple source.

We consider a simple source represented by a sphere of radius a. The surface of the sphere is vibrating with complex speed $U_0 e^{-i\omega t}$, where U_0 is the speed amplitude of the surface, and the specific acoustic impedance is given by (2.5). If we evaluate both the specific acoustic impedance for a spherical wave (2.5) and the acoustic pressure from the source (2.2) at $r = a$, we get from (2.3) that

$$\frac{A}{a} e^{-i(\omega t - ka)} = \rho_0 c \cos\phi_a e^{-i\phi_a} \cdot U_0 e^{-i\omega t}$$

$$A = \rho_0 c U_0 a \cos\phi_a e^{-i(ka+\phi_a)}$$

$$\Downarrow$$

$$p(r,t) = \rho_0 c U_0 \frac{a}{r} \cos\phi_a e^{-i(ka+\phi_a)} e^{-i(\omega t - kr)}$$

$$= \rho_0 c U_0 \frac{a}{r} \kappa_a e^{-i(\omega t - kr)},$$

where ϕ_a refers to $r = a$. The constant $\kappa_a = \cos\phi_a e^{-i(ka+\phi_a)}$ is highly dependent on the size of the source, and the wavelength. From the relations $c = \lambda f$ and $k = \frac{2\pi f}{c}$, we have $k = \frac{2\pi}{\lambda}$, which makes ka small if $\frac{2\pi a}{\lambda}$ is small. It can be shown by complex calculations that in this case we may write $\kappa_a = ka$. However, in the case of the MS70 sonar, frequencies range from 75 KHz to 112 KHz, excluding this approximation.

To account for the shape of simple sources, we introduce its source strength Q. This can be defined as the integrated surface speed of the source,

$$Q = \int_{\text{surface}} \mathbf{u} \cdot \mathbf{n} \, dS,$$

where dS is a small surface element, and $\mathbf{n}$ is the normal vector on the surface. (The source strength is actually complex, but for our purposes we consider it real.) For the sphere with radius a, the source strength is $Q = U_0 4\pi a^2$, giving the pressure expressed in terms of Q:

$$p(r,t) = \rho_0 c \frac{\kappa_a}{4\pi a} \frac{Q}{r} e^{-i(\omega t - kr)}.$$

2.4 Pressure field from a line source.

We will later represent fish as line sources, giving a good approximation to the sound scattered from either the swim bladder, or from the whole fish if it does not have a swim bladder. To find the pressure field from the line source, we consider many simple sources on a line, and integrate the pressure dp from each simple source. This integration involves the angle of incidence γ to the line source, for the vector from the midpoint of the line source to a point in space. The length of this vector is r, while the vector from the simple source of length dx to the point in space has length r' (Figure 2.1). The source strength of each element of the line source will be $dQ = U_0 2\pi a dx$, where $2\pi a dx$ is the surface in contact with the radiation medium. We thus get the following integral for the pressure field of the line source:

$$p\left(r,\gamma,t\right) = \rho_0 c U_0 \frac{\kappa_a}{2} \int_{\frac{-L}{2}}^{\frac{L}{2}} \frac{1}{r'} e^{-i\left(\omega t - kr'\right)} dx.$$

In the exponent, r' must be approximated carefully by $r - x\sin(\gamma)$, while $\frac{1}{r'}$ will simply be set to $\frac{1}{r}$. This is because the difference between r and r' give the pressure field a beam pattern dependent on γ. Integration now yields:

$$\begin{aligned} p\left(r,\gamma,t\right) &= \rho_0 c U_0 \frac{\kappa_a}{2} \frac{1}{r} e^{-i(\omega t - kr)} \int_{\frac{-L}{2}}^{\frac{L}{2}} e^{-i\omega k x \sin\gamma} dx \\ &= \rho_0 c U_0 \frac{\kappa_a}{2} \frac{L}{r} e^{-i(\omega t - kr)} \left(\frac{\sin\left(\frac{1}{2} kL \sin\gamma\right)}{\frac{1}{2} kL \sin\gamma} \right). \end{aligned} \tag{2.7}$$

The pressure can thus be decomposed in an axial factor, and a directional factor with values in $[0,1]$:

$$p\left(r,\gamma,t\right) = P_{\mathrm{ax}}\left(r\right) H\left(\gamma\right) e^{-i(\omega t - kr)},$$

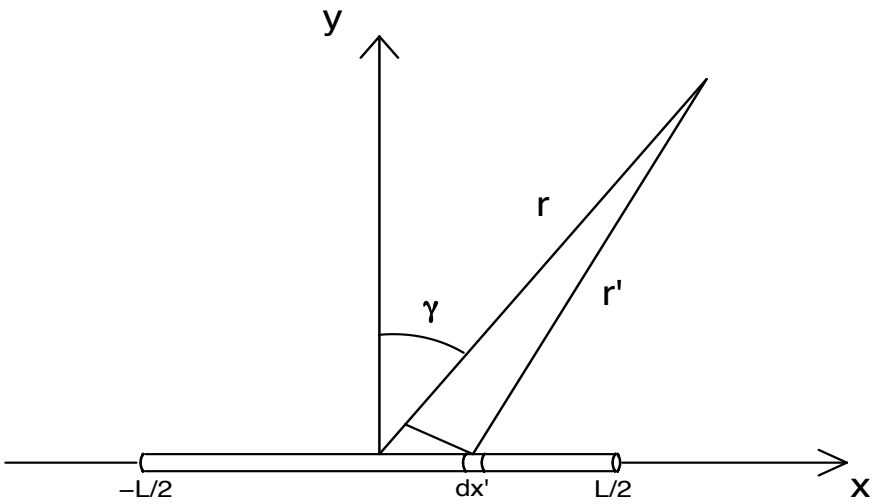

Figure 2.1: Integration of simple sources representing a line source.

where

$$P_{\text{ax}}(r) = \rho_0 c U_0 \frac{\kappa_a}{2} \frac{L}{r} \quad \text{and}$$

$$H(\gamma) = \left(\frac{\sin\left(\frac{1}{2} kL \sin\gamma\right)}{\frac{1}{2} kL \sin\gamma} \right) = sinc\left(\frac{1}{2} kL \sin\gamma\right) = j_0\left(\frac{1}{2} kL \sin\gamma\right).$$

The directional factor $H_F(\gamma)$ is called the sinc function, or the zeroth order spherical Bessel function of the first kind (denoted by $j_0(x)$), and is plotted against incident angle γ as the blue line in Figure 2.2. The nature of the Bessel function produces a surface of equal pressure amplitude as shown in Figure 2.3. The figure displays one major lobe, and three side lobes of lower intensity.

If the acoustic intensity is treated, the squared expression in (2.6) gives us the factorization

$$I(r,\gamma) = I_{\text{ax}}(r)\, B(\gamma)\,, \tag{2.8}$$

$$I_{\text{ax}}(r) = \frac{\left[P_{\text{ax}}(r)\right]^2}{2\rho_0 c} \quad \text{and} \quad B(\gamma) = \left[H(\gamma)\right]^2.$$

2.5 Pressure field from a baffled circular source.

The integration leading to the pressure field from a circular piston considers parallel line sources of variable length, which constitutes the piston. Every line source is evaluated at incident angle $\gamma = 0$, because of the symmetry of the circle. The integration will not be carried out here, and we only present the end result. It is reasonable that the directional factor will be related to a Bessel function, and we get the same kind of expression with a function divided by the argument of the function, as for the line source.

$$p(r,\gamma,t) = \rho_0 c U_0 \frac{\kappa_a}{2}\frac{a}{r} e^{-i(\omega t - kr)} \left(\frac{2J_1(ka\sin\gamma)}{ka\sin\gamma}\right) = P_{\text{ax}}(r)\, H(\gamma)\, e^{-i(\omega t - kr)}, \tag{2.9}$$

where a is the radius of the circular piston, γ is the incident angle with acoustic maximum, and κ_a is evaluated at the distance a. $J_1(x)$ is here the first order Bessel function of the fist kind, written by an upper case J, as opposed from the spherical Bessel function of the line source, which is written by a lower case j. As for the line source, (2.8) will be valid for the circular piston.

As a function of incident angle γ, the directional factor for the circular piston has lower side lobe level than that of the line source, as can be seen in Figure 2.2. Side lobe level for a circular piston will be approximately -17.5 bB independent on frequency f and radius a. The surface of equal pressure amplitude from a circular piston is shown in Figure 2.4.

It is common to describe the *beamwidth* by the angle where the acoustic intensity is reduced by 50% compared to maximum. This is often refered to as the -3 dB - angle.

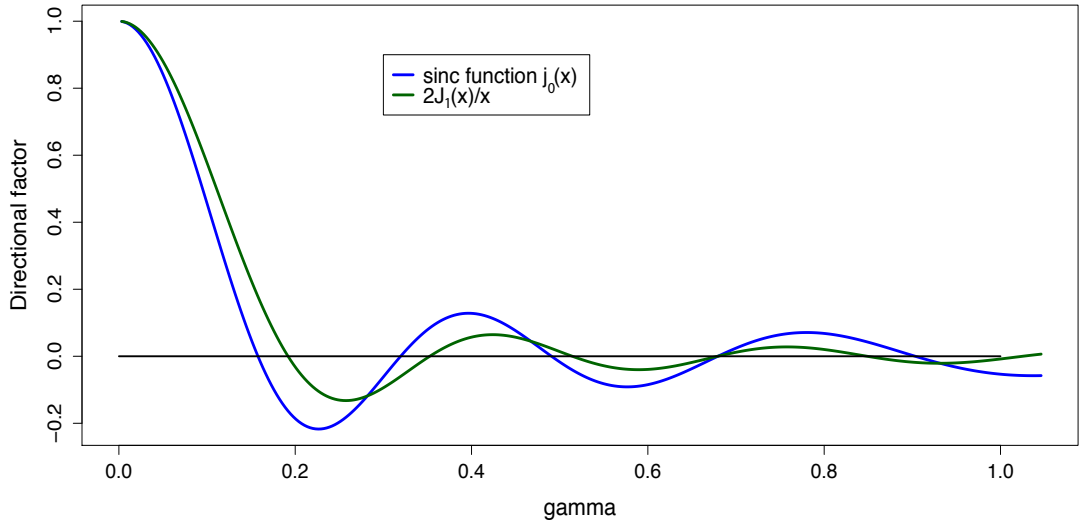

Figure 2.2: Directional factor for the pressure for a lines source (blue) and a circular piston (dark green) as functions of γ. Notice the notational distinction between the Bessel function J and the spherical Bessel function j

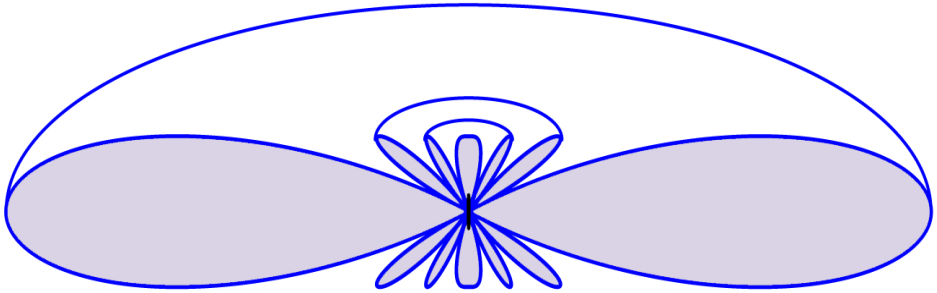

Figure 2.3: Surface of equal pressure amplitude from a line source.

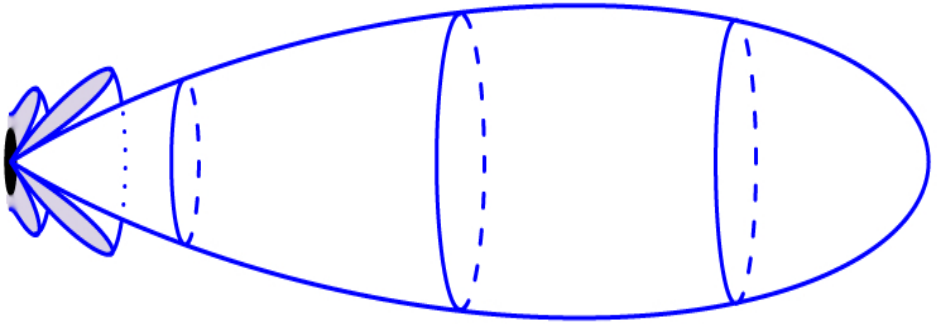

Figure 2.4: Surface of equal pressure amplitude from a circular piston.

2.6 Underwater acoustics.

2.6.1 Absorption and attenuation.

When traveling through a medium, the energy in a sound wave is inevitably absorbed. Different types of thermodynamic and molecular processes cause this absorption, but as a general concept we can summarize all losses in one absorption constant c_a.

The derivation of c_a can be illustrated by adding terms representing absorption to the Euler's equation (2.2). This will be analogous to adding terms of resistance to Newton's second law, reducing the acceleration. When solving this new lossy Euler's equation, (Navier-Stokes equation), with respect to the pressure p, assuming monofrequency sound, the result is pressure waves of the same form as the plane and spherical waves in (2.1) and (2.2), but with complex wave number $k_{complex} = k + ic_a$:

$$p(x,t) = Ae^{-c_a x}e^{-i(\omega t - kx)} \qquad (plane)$$

and

$$p(r,t) = \frac{A}{r}e^{-c_a r}e^{-i(\omega t - kr)} \qquad (spherical).$$

The derivation of these lossy pressure waves will not be shown here. When examining absorption and geometric attenuation, it is often useful to consider the acoustic intensity rather than the pressure:

$$I(x) = \frac{P^2}{2\rho_0 c} = \frac{A^2}{2\rho_0 c}e^{-2c_a x} = \frac{A^2}{2\rho_0 c}\cdot 10^{-\alpha x} \qquad (plane)$$

and

$$I(r) = \frac{P^2}{2\rho_0 c} = \frac{A^2}{2\rho_0 c}\frac{1}{r^2}e^{-2c_a r} = \frac{A^2}{2\rho_0 c}\cdot\frac{1}{r^2}\cdot 10^{-\alpha r} \qquad (spherical).$$

Here $\alpha = 2c_a/ln10 \approx 0.87c_a$, which is useful for decibel calculations. We see that the acoustic intensity is split into a constant factor and an absorption factor for the plane wave, and an additional geometric attenuation factor for the spherical wave. The constant factor $A^2/2\rho_0 c$ reflects the power of the source, and will be proportional to the backscattering ability of a fish, as used later in the thesis.

2.6.2 Refraction.

The speed of sound c in water is dependent on temperature, salinity and water pressure, and can be approximated by the empiric relation

$$c\left(T_W, S_W, P_W\right) = 1449.08 + 4.57T_W e^{-\left(\frac{T_W}{86.9}+\left(\frac{T_W}{360}\right)^2\right)} + 1.33\left(S-35\right)e^{-\frac{T_W}{120}} + 0.1522P_W e^{\left(\frac{T_W}{1200}+\frac{S_W-35}{400}\right)} + 1.46\cdot 10^{-5}P_W^2 e^{-\left(\frac{T_W}{20}+\frac{S_W-35}{10}\right)}.$$

Here T_W is temperature in the water in degrees Celsius, S_W is salinity in the water in parts per thousand and P_W is water pressure in atmospheres (1 atm=101325 Pa, where 1 Pa=1 kg per m^2.). Roughly speaking the speed of sound in water is linear with respect to salinity and pressure, and follows approximately $1.27S_W$ and $0.17P_W$. Water pressure increases linearly with depth as $P_W\left(z\right) = \rho_0 gz = 10085.14z$ Pa, where $\rho_0 = 1027$ kg/m^3 is the density of sea water at zero depth, and $g = 9.82\mathrm{m/s}^2$ is the gravitational acceleration in Norway. Expressed in atmospheres the depth dependency is approximately $-0.016z$ (Figure 2.5). The temperature dependence of c however, can not be considered linear, but follows roughly $4.4T_W - 0.08T_W^2$. Anyhow, we see that temperature has the greatest effect on c, with a rate of change about 20 times larger than that of pressure, and about 200 times larger than that of depth.

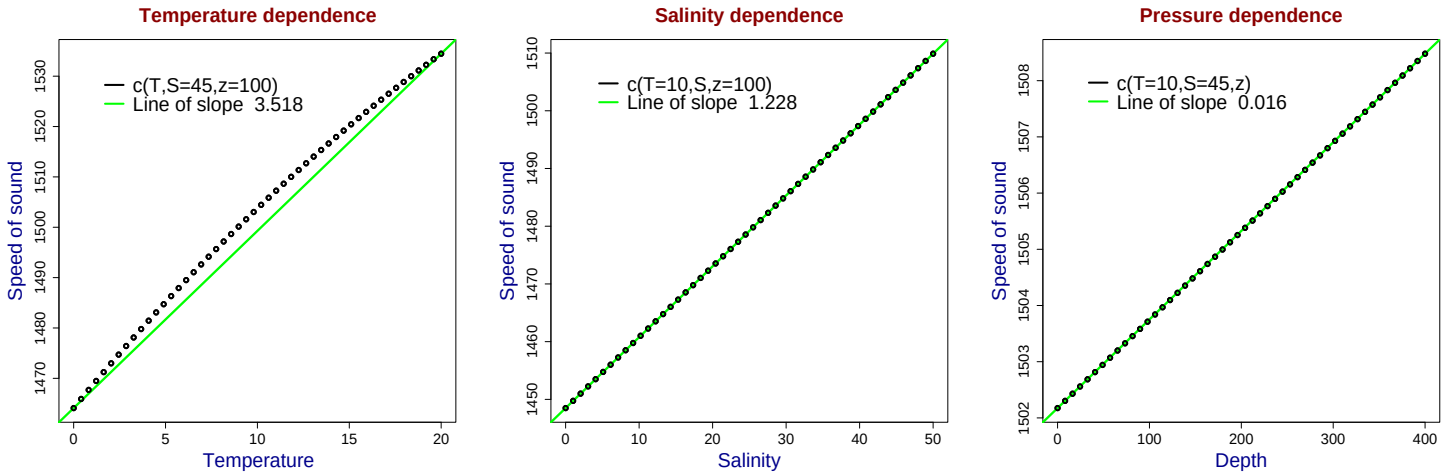

Figure 2.5: Speed of sound as a function of temperature T in Celsius (left), salinity S in parts per thousand (middle) and depth z in meters (right).

For acoustic surveys, salinity is unlikely to change very much, and the depth dependence is always present. The crucial variable affecting speed of sound, is thus the temperature profile with depth, which must be measured at, or close to the survey location. If we assume that for a given depth interval, the temperature changes linearly with depth, and that this temperature change is small enough to consider c to be linearly dependent on temperature, we can assign to the speed of sound a gradient $c(z) = \eta z$ in the interval, which can be either negative, zero or positive with respect to depth. We will show that these three situations will result in downwards refraction, straight sound rays, and upwards refraction respectively.

In Figure 2.6 we consider a small element of the sound ray having width b. (All symbols in the figure and the discussion based on the figure omited in the symbols list in Appendix B.) The upper portion of the ray moves the distance $l + \Delta l$, while the lower part only moves the distance l, due to the difference in speed of sound between the upper and the lower part. Many such elements of a sound ray will constitute a circular path, if the angle of the front of the element changes constantly. This will be approximately true for not too large changes in direction of the sound ray. The linear relationship between distance and speed leads to

$$\frac{\Delta l}{l} = \frac{c_1 - c_2}{c_2} = \frac{c_0 + \eta z_1 - (c_0 + \eta z_2)}{c_2} = \frac{\eta(z_1 - z_2)}{c_2} = \frac{\eta h}{c_2} = \frac{\eta b \cos\gamma}{c_2},$$

where c_0 is the speed of sound at $z = 0$, and other symbols are shown in Figure 2.6. As the sound ray moves along a circular path, and the distance l is small, the angle $\Delta\gamma$ can be approximated by both

$$\Delta\gamma \approx \frac{l}{r} \qquad \text{and} \qquad \Delta\gamma \approx \frac{\Delta l}{b},$$

where r is the radius of the circular path. We thus get this expression for r:

$$r = b\frac{l}{\Delta l} \approx \frac{c(z)}{\eta \cos\gamma}, \tag{2.10}$$

where we have replaced c_2 by the speed of sound $c(z)$ for a thin sound ray at depth z. From (2.10) we see that as the angle γ between the sound ray and horizontal approaches 90°, or as the speed gradient η approaches zero, the circle gets infinitely large, and $\gamma = 90°$ or $\eta = 0$ implies no refraction. The situations with speed gradient η and $-\eta$, has the same circle, only with differently located centers.

The circular path of a sound ray is displayed in Figure **??**. Using simple trigonometry, we get the following four equations, which fully

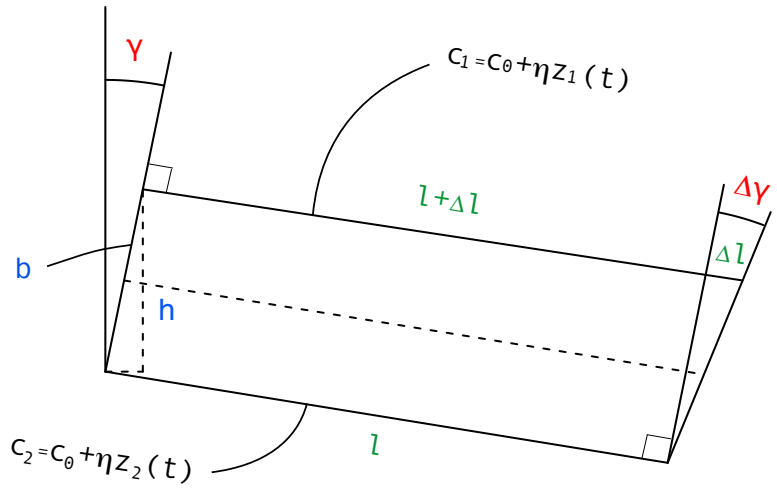

Figure 2.6: Refraction of a small element of a sound ray. The direction of the ray changes from γ to $\gamma + \Delta\gamma$, from the upper part of the ray moving Δl further than the lower part.

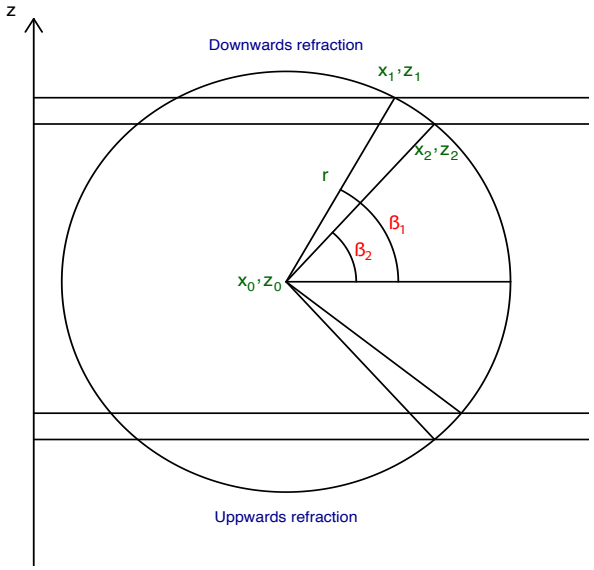

Figure 2.7: The circular path of a sound ray caused by the constant speed gradient in the depth interval (z_1, z_2). Given that we know the initial condition x_1, z_1 and β_1, and the speed of sound c_1 and c_2 at the depths z_1 and z_2, we can fully describe this circular path.

describe the path in the given depth interval (variables in blue are known):

$$z_1 = z_0 + r\sin\beta_1 \qquad x_1 = x_0 + r\cos\beta_1$$

$$z_2 = z_0 + r\sin\beta_2 \qquad x_2 = x_0 + r\cos\beta_2$$

For a sequence of depth - speed of sound combinations, we can then start out with the initial position and direction of the sound ray of interest, and iteratively calculate the path of the ray. This will be done in chapter 4, where we define the system of voxels to be used in the thesis.

2.7 Acoustic backscattering.

When sound from the transducer strikes an object, the object scatters the sound in all directions. If the object is not a simple source, so that the scattered sound has a directional factor, the intensity $I_S(r', \theta', \phi')$ of the scattered signal, (with subscript denoting the source), is a function of distance r' from the source, and the direction angles θ' and ϕ' in some spherical coordinate system defined for the object. In Chapter 6 we will define the coordinate system of a fish as the spherical/cartesian coordinate system centered at the middle of the fish, with y-axis along the direction of the fish, and with horizontal x-axis. Many variables in fisheries acoustics describe the ability of an object to scatter sound, and consistent definitions of these variables are given in (MacLennan et al., 2002). We will refer to these definitions when defining the variables used in this master thesis:

If we do not know the properties of the object scattering the sound, we may assume that the echo is generated by a simple source described earlier in this chapter. A simple source radiates equally in every direction, and has thus a constant directional factor $H(\theta', \phi') = 1$. Imagining a spherical simple source that radiates the same intensity in some direction as the object does, we can define the differential scattering cross section $\sigma(\theta', \phi')$ of the object. This will be the acoustic intensity from the object in the given direction, integrated on the unit sphere centered at the object, and divided by the acoustic intensity $I_T(r)$ striking the object at the distance r from the transducer.

$$\sigma(\theta', \phi') = \frac{4\pi I_S(r' = 1, \theta', \phi')}{I_T(r)}, \tag{2.11}$$

where 4π is the area of the unit sphere. We have here assumed that no energy is lost in the signal at $r' = 1$. The definition of $\sigma(\theta', \phi')$ differs from (MacLennan et al., 2002) by the factor 4π.

The acoustic power scattered by the simple source scattering the same amount of sound in the given direction as the object does, (with subscript denoting the source), is $\Pi_s = I_T(r)A_s(\theta', \phi')$, where $A_s(\theta', \phi')$ is the cross sectional area of the scattering sphere (not to be confused with the pressure amplitude of a plane wave given in (2.1)). The acoustic intensity from the simple source at the distance $r' = 1$ will thus be $I_S(r' = 1, \theta', \phi') = I_T(r)A_s(\theta', \phi')/4\pi$. The differential scattering cross section becomes

$$\sigma(\theta', \phi') = \frac{4\pi \dfrac{I_T(r) A_s(\theta', \phi')}{4\pi}}{I_T(r)} = A_s(\theta', \phi').$$

We see that we can interpret $\sigma(\theta', \phi')$ as the cross sectional area $A_s(\theta', \phi')$ of a spherical bubble of air, scattering the same acoustic intensity in the direction (θ', ϕ') as the object does.

From $\sigma(\theta', \phi')$ we can now define the optimal scattering cross section σ_0, by factorizing the acoustic intensity into an axial factor and a directional factor as was done in (2.8):

$$\sigma(\theta', \phi') = \frac{4\pi \left(I_S(r' = 1)\right)_{\text{ax}} B_S(\theta', \phi')}{I_T(r)} = \sup\left(\sigma(\theta', \phi')\right) B_S(\theta', \phi') \equiv \sigma_0 B_S(\theta', \phi'), \tag{2.12}$$

where $\left(I_S(r' = 1)\right)_{\text{ax}}$ is the intensity in the directions having $\gamma = 0$. We also define the spherical backscattering cross section σ_{sp} according to the definition in (MacLennan et al., 2002):

$$\sigma_{sp} = \sigma(\theta'_R, \phi'_R),$$

where (θ'_R, ϕ'_R) is the direction of the receiver.

The target strength TS is simply a logarithmic version of σ_{sp}, and is in (MacLennan et al., 2002) defined as

$$\text{TS} = 10 \log\left(\frac{\sigma_{sp}}{4\pi}\right) = 10 \log\left(\frac{I_S(r' = 1, \theta'_R, \phi'_R)}{I_T(r)}\right).$$

We see that TS is a typical decibel quantity, and for objects far from the transducer, the argument in the logarithm is the ratio of incoming and outgoing acoustic intensity at the distance 1 meter from the object, in the direction of the transducer/receiver.

To measure echo ability per unit volume (m^3), scattering strength S_v is used:

$$\mathrm{S}_v = 10\log\left(\sum_V \frac{I_S\left(r'=1,\theta'_R,\phi'_R\right)}{I_T(r)}/V\right) = 10\log\left(\sum_V \frac{\sigma_{sp}^{(i)}}{4\pi V}\right), \tag{2.13}$$

where V is some volume of interest, and $\sigma_{sp}^{(i)}$ is the spherical backscattering cross section of fish number i in the volume. The scattering strength is a logarithmic density measure, and we will attempt to link this to the density of small simple sources of a certain size. If we imagine representing the scattering strength by N bubbles of air, of cross sectional area b, we get:

$$\mathrm{S}_v = 10\log\left(\frac{N\cdot b}{4\pi V}\right) \qquad \Longrightarrow \qquad B \equiv \frac{N}{V} = \frac{4\pi}{b}10^{S_v/10}. \tag{2.14}$$

Combining (2.13) and (2.14) we get the connection between total spherical backscattering cross section and B-value:

$$\sum_V \sigma_{sp}^{(i)} = \sum_V \sigma_0^{(i)} B_S(\theta'_R,\phi'_R) = bBV, \tag{2.15}$$

where $B_S(\theta'_R,\phi'_R)$ and B are fundamentally different, as they represent the directional factor if the acoustic intensity and the number of bubbles of air of cross sectional area b respectively. The variable B is simply a linear measure of the density of echo ability, as opposed to the logarithmic measure S_v. A suitable size of these bubbles would be $b = 1\ mm^2 = 10^{-6}\ m^2$. In chapter 6 we will see that due to interference effects B will only be the *expected* density of uniformly distributed bubbles.

Chapter 3

Materials

3.1 Research vessel.

The data set analyzed in this master thesis is from the research vessel G.O.Sars owned by the Institute of Marine Research (IMR) and the University of Bergen (UIB) in Norway. G.O.Sars is equiped with the MS70 scientific multibeam sonar, and the particular survey we are investigating was done on the 25. of January 2006, outside Røst to the west of Bodø in Northern Norway. The coordinate system of the research vessel is defined by the manufacturer of the sonar, as a right hand system with the x-axis in the direction of the vessel, y-axis pointing straight out on the starboard side of the vessel, and z-axis in the opposite direction of the mast of the vessel. In this thesis however, we will for simplicity define the coordinate system of the vessel as having x-axis to the starboard side of the vessel, y-axis in the direction of the vessel, and z-axis in the direction of the mast of the vessel.

3.2 MS70 scientific multibeam sonar.

The MS70 sonar is a multibeam sonar manufactured by Simrad Horten AS, in Horten, Norway, and is mounted on the port side of the research vessel G.O.Sars. It consists of $32 \cdot 25 = 800$ elements, radiating sound at frequencies in the range (70 kHz, 112 kHz). Using 6 computers, the elements are weighted to construct 500 narrow beams located on 25 fans, of 20 beams radiating in the same vertical plane (vertical fans). The 25 vertical fans are rotated from $-30°$ to $30°$, with $0°$ being straight out on the port side of the vessel. Within a vertical fan, the beams are tilted downwards from $0°$ to $45°$, but the entire system of the 500 beams can be tilted up to $10°$ more downwards. We may also consider 20 horizontal fans, consisting of 25 beams, but as we will see in Chapter 4, the beams in these horizontal fans do not radiate in the same plane, but in curved planes. All beams in a horizontal fan will radiate sound at the same

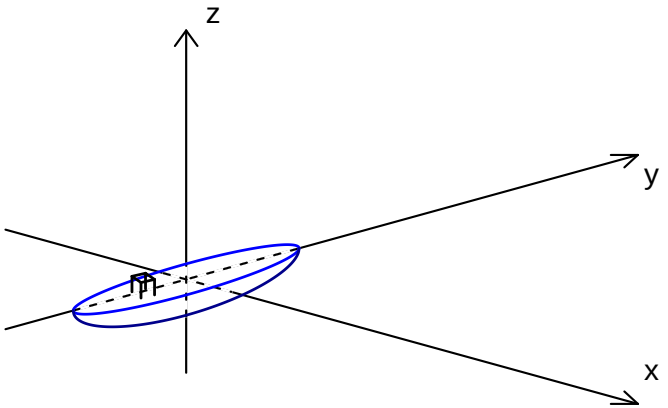

Figure 3.1: The coordinate system of the research vessel, as defined in this thesis.

frequency, and the upper fan has the lowest frequency, but rising with depth.

Because of the different frequencies of the horizontal fans, it is possible to weight the elements vertically at reception as well as at transmission, giving a narrower beam vertically than horizontally. The beam width defined at the end of section 2.5, varies among the beams, and is dependent on frequency. For the data in this thesis the beam widths are in the range $(6.111902°, 6.962585°)$ horizontally and in the range $(2.602462°, 4.395848°)$ vertically.

The vertical weighting at reception also reduces the side lobe levels. It is given by the manufacturer that the first side lobe level is -25 dB horizontally and -35 dB vertically, relative to acoustic maximum of the beams. This implies that side lobe levels vary with θ_b (subscript b denoting the beam) in a spherical coordinate system having z-axis along acoustic maximum of the beam (i.e. θ_b is the angle in the x-y-plane). An ideal circular piston will have side lobe level equal to -17.5 dB, independent of θ_b, so it is clear that the beam patterns in MS70 is more complex than the first order Bessel function. In chapter 6, we will approximate the directional factor for the beams in MS70 by the first order Bessel function of the circular piston, and by a second order polynomial function, when investigating the stochastic effect of randomness in the size, position and orientation of fish.

The 500 beams are numbered with the pairs of values (i, j), $i = 1, \ldots, I = 25$ and $j = 1, \ldots, J = 20$, where i is the number of the beam in the horizontal fan, counted from left to right as seen from above, and j is the number of the beam in the vertical fan number i, as

counted from below. This means that beam number (1,1) is located in the bottom left corner of the volume, as seen from the transducer. The manufacturer has also assigned to the beams, a set of rotation angles (α_i, β_j), so that

$$\begin{aligned} \alpha_i &= -30^\circ, -30^\circ + \Delta\alpha, \ldots, -30^\circ + (i-1)\,\Delta\alpha, \ldots, 30^\circ \quad \text{and} \\ \beta_j &= -45^\circ, -45^\circ + \Delta\beta, \ldots, -45^\circ + (j-1)\,\Delta\beta, \ldots, 0^\circ, \end{aligned} \tag{3.1}$$

where $\Delta\alpha = 60^\circ/24$ and $\Delta\beta = 45^\circ/19$. Beam number (1,1) will thus have rotation angles $(\alpha_1, \beta_1) = (-30^\circ, -45^\circ)$, while beam number (13,20) has rotation angles $(\alpha_{13}, \beta_{20}) = (0, 0)$. If the sonar is tilted additionally, we call the tilt angle $\tau \in [-10^\circ, 0^\circ]$.

Sound pulse durations are specified by the manufacturer in the range 2 ms to 10 ms, but the data set examined in this master thesis were produced using 0.512 ms. This provides higher density in the radial direction, but might have some disadvantages regarding noise. One image produced by one sound pulse, is called a ping. The distance in time between pings vary, but is of course restricted by the time used by the sound pulse on the way out from the transducer and back. For the data treated in this thesis, pings are separated in time by ca 5 seconds.

3.2.1 Unit vectors of the beams.

The MS70-sonar is mounted on the port side of the research vessel, which implies that beam number (13,20) points in the opposite direction as the x-axis of the vessel, and has unit vector $\mathbf{d}_{13,20} = -\mathbf{e}_x = (-1, 0, 0)$. If the sonar is tilted by the angle τ, $\mathbf{d}_{13,20} = (-\cos\tau, 0, -\sin\tau)$. To find the unit vector $\mathbf{d}_{i,j}$ for an arbitrary beam (i, j), we rotate the coordinate system of the vessel by the angle $-\alpha_i$ counter clockwise around the z-axis, and then by the angle β_j counter clockwise around the y-axis. This is called an z-y-rotation, and is the same as first finding the right vertical fan, and then tilt within the vertical fan. The minus sign in α_i arises from the way the angle is defined, since a beam with positive α_i actually is rotated *clockwise* around the z-axis. In the rotated coordinate system, the beam now has unit vector equal to $-\mathbf{e}_x = (-1, 0, 0)$, unless the sonar is tilted additionally.

The simplest way to perform this rotation is by multiplying the unit vector $\mathbf{d}_{i,j}$ of the acoustic maximum of the beam in question by a rotation matrix $\mathbb{A}_{zy}(-\alpha_i, \beta_j)$ given in Appendix A:

$$-\mathbf{e}_x = \mathbb{A}_{zy}(-\alpha_i, \beta_j) \cdot \mathbf{d}_{i,j},$$

where the subscript zy refer to the z-y-rotation. To rotate back to the coordinate system of the vessel, we use the (A) to write:

$$\mathbf{d}_{i,j} = \mathbb{A}_{yz}(-\beta_j, \alpha_i) \cdot -\mathbf{e}_x.$$

We have now established the unit vectors along the maximum of each beam, and by multiplying these vectors by the distance r from the transducer, we get an arbitrary point on these maxima. This will be useful later, since we will mainly work with points on these maxima.

3.3 Sonar Explorer.

To identify the values in the data set coming from a school, the segmentation procedure in the Sonar Explorer was used. This is an application software for three dimensional visualization, tracking, and segmentation of fish schools observed by the MS70 sonar, and is developed by (Balabanian et al., 2007). The algorithm used to identify the values belonging to the school, is presented in chapter 7. To avoid high intensity noise from affecting the segmentation, median smoothing was performed on the data during the segmentation.

3.4 Statistical analysis.

For the statistical analysis, plotting and other treatment of the data, the free statistical software R was used. R contains a wide range of statistical methods, and provides the user with a simple programming language for developing own methods.

Chapter 4

Interpretation of data.

The acoustic signal received in a unit time interval $(t, t+\Delta t)$ for a specific beam, contains primarily information about the echo ability of objects in a volume limited by the time interval and the narrowness of the beam. In this chapter we define a system of three dimensional unit volumes called voxels, which are mutually exclusive, and which are constructed so that the information given by the data, about the echo ability in each voxel, is maximized. We also calculate the volume of the voxels, and the path of sound rays when accounted for refraction in sea water.

4.1 Representation of echo ability from voxels.

The acoustic pressure experienced by one of the elements in the MS70 sonar, will be a continuous function of time, and ideally a sine function. Acoustic intensity was defined in chapter 2, to be the time average of the product of pressure and particle speed during one period, so we clearly need at least one period $T = f^{-1}$ to get a measure of the received intensity. We will here show that intensity received in the time intervals $(0, \tau_p), (\tau_p, 2\tau_p), \ldots, ((k-1)\tau_p, k\tau_p), \ldots, ((K-1)\tau_p, K\tau_p)$ reflects the echo ability in spherical shells centered at the sonar, where τ_p is the duration of the signal with subscript referring to the "ping" and $k = 1, \ldots, K$. The shells can further be divided into almost rectangular voxels, using the strong directivity of the beams from the MS70 sonar. As the sonar emits spherical waves, the acoustic intensity is reduced as the square of distance r, and the signal to noise ratio falls of accordingly. The total number of sampling intervals are restricted to K because of this.

4.1.1 Radial partitioning.

In Figure 4.1, we consider the backscattered signal from a small object at the distance h from the sonar. The object will experience the sound pulse in time interval $(h/c, h/c+\tau_p)$, and the echo from the object will strike the sonar in the time interval $(2h/c, 2h/c+\tau_p)$. This implies that unless we have that $2h/c = k\tau_p$, for integers $k = 0, \ldots, K$, the energy from the object will be shared by two consecutive time intervals. For objects located at distances $h = c\tau_p(k-1/2)/2$, the echo will be shared equally between time intervals $((k-1)\tau_p, k\tau_p)$ and $(k\tau_p, (k+1)\tau_p)$. These distances define the spherical shells of the radial partitioning.

For the specific object in Figure 4.1, a proportion $1 - h'/(\tau_p/2)$ of the total signal from the object is received during the second time interval, while $h'/(\tau_p/2)$ is received during the third time interval, where $h' = h\%(\tau_p/2)$. If the object was located $3(\tau_p/2)/2$ from the sonar, it would contribute equally to the second and the third time interval. The coloured spikes at the right of Figure 4.1 is the proportion of the signal from an object at some distance, that is received in the time interval of the respective colour. For the object at distance h in the figure, the dark blue interval receives a bit more of the signal from the object than the turquoise time interval does. This allocates the object to the third spherical shell/voxel, as seen far to the right of the figure. Beginning at $r = 0$, we get these $K+1$ surfaces defining the spherical shells constituting the radial partitioning:

$$0, r_2 - \frac{\Delta r}{2}, \ldots, r_K - \frac{\Delta r}{2}, r_K + \frac{\Delta r}{2} \tag{4.1}$$

where

$$r_k = \frac{c\tau_p/2}{4}, \frac{c\tau_p}{2}, \frac{2c\tau_p}{2}, \ldots, \frac{c\tau_p(k-1)}{2}, \ldots, \frac{c\tau_p(K-1)}{2}$$

for $k = 1, \ldots, K$ and $\Delta r = c\tau_p/2$. For the data treated in this thesis, the maximum range of the sonar is set to $K = 1319$, but noise dominates the data for k larger than 1000. For the speed of sound $c = 1481\ m/s$, and pulse duration $\tau_p = 5.12 \cdot 10^{-4}$, given for the data set considered in this thesis, the thickness of spherical shells are $\Delta r = 0.379$ m.

A radial partitioning of this kind will result in an overlap between the signal received in consecutive time intervals, giving a correlation between neighbouring voxels in beams. This will be shown in chapter 6.

4.1.2 Angular partitioning.

Although incorrect, we assume that the 500 beams have the same directional factor, as a function of direction, so that we can partition the spherical shells established above, into voxels in a simple and reasonable way. In chapter 3, we presented rotation angles α_i and β_j

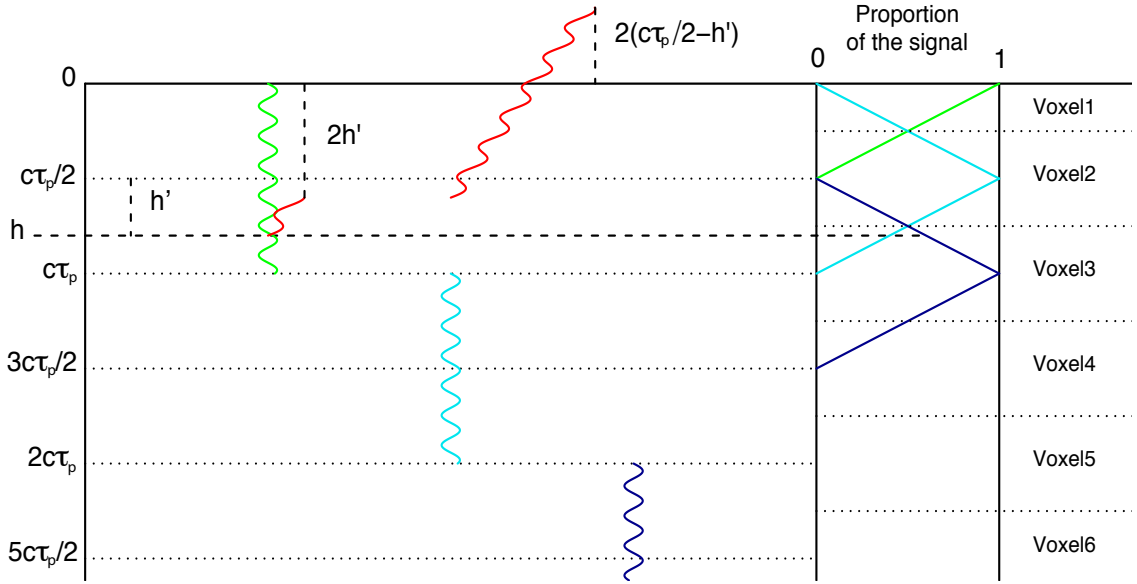

Figure 4.1: Backscattering received during time intervals $[t_1, t_2)$, $[t_2, t_3)$ and $[t_3, t_4)$, from an object located a distance h from the transducer. h' is equal to $h\%(c\tau_p/2)$. During the second time interval $[t_2, t_3)$, the transducer receives the fraction $1 - h'/(c\tau_p/2)$ of the signal scattered by the object, while the fraction $h'/(c\tau_p/2)$ is left to the third time interval.

for unit vectors along acoustic maximum for the $25 \cdot 20$ beams, given by (3.1). A natural way to do the partitioning would be $26 + 21$ surfaces given by

$$\begin{aligned} &\alpha_1 - \frac{\Delta\alpha}{2}, \alpha_2 - \frac{\Delta\alpha}{2}, \ldots, \alpha_I - \frac{\Delta\alpha}{2}, \alpha_I + \frac{\Delta\alpha}{2} \quad \text{and} \\ &\beta_1 - \frac{\Delta\beta}{2}, \beta_2 - \frac{\Delta\beta}{2}, \ldots, \beta_J - \frac{\Delta\beta}{2}, \beta_J + \frac{\Delta\beta}{2} \ , \end{aligned} \tag{4.2}$$

where

$$\alpha_i = -30^\circ, -30^\circ + \Delta\alpha, \ldots, -30^\circ + (i-1)\,\Delta\alpha, \ldots, 30^\circ \quad \text{and}$$

$$\beta_j = -45^\circ, -45^\circ + \Delta\beta, \ldots, -45^\circ + (j-1)\,\Delta\beta, \ldots, 0^\circ\ ,$$

and where $i = 1, \ldots, I$ and $j = 1, \ldots, J$, and for the MS70 sonar $I = 25$ and $J = 20$. As before $\Delta\alpha = 60^\circ/24$ and $\Delta\beta = 45^\circ/19$. The partitioning from the α-surfaces and the β-surfaces are shown separately in Figure 4.2 and Figure 4.3. When combined, the r- α- and β-surfaces defines the system of voxels. As in the radial case, the angular partitioning results in smoothing of the data.

We define the thickness of a voxel as the thickness of the respective spherical shell. The width and height of voxels will be related to α_i and β_j as $r \sin \Delta\alpha_i$ and $r \sin \Delta\beta_j$. Thus the width and height of voxels range up to 21.8 meters and 20.7 meters respectively. Unless the school is very close to the research vessel, voxels will have shapes almost like thin rectangular plates, of thickness 0.379 meters, and width and height typically around 10 meters. The midpoints of voxels will thus be like pearls on strings radiating out from the transducer, rather than points on a regular rectangular grid.

4.1.3 Volume of the voxels.

The volume of the voxels can be found using the surfaces above, by first considering an open spherical sector defined by the angles $\alpha_i - \Delta\alpha/2$ and $\alpha_i + \Delta\alpha/2$. Figure 4.2 shows half of such a sector, and the volume of an open spherical sector is known to be

$$V_{\text{sph.sct.}}\,(r_k) = \frac{2}{3}\pi r_k^2 \left(z_{jk} + \frac{\Delta z}{2} - \left(z_{jk} - \frac{\Delta z}{2} \right) \right) = \frac{2}{3}\pi r_k^3 \left(\sin\left(\beta_j + \frac{\Delta\beta}{2} \right) - \sin\left(\beta_j - \frac{\Delta\beta}{2} \right) \right),$$

where $z_{jk} = r_k \sin\beta_j$ is seen from Figure 4.2. The radial partitioning now results in a strip like part of a spherical shell with volume $V_{\text{sph. sct.}}(r_k + \Delta r/2) - V_{\text{sph. sct.}}(r_k - \Delta r/2)$, for two neighbouring radial distances $r_k - \Delta r/2$ and $r_k + \Delta r/2$. The α-partitioning will simply divide the strip by the factor $\Delta\alpha/2\pi$, giving us the volume of a voxel as a function of β_j and r_k:

$$V_{ijk} = \frac{\Delta\alpha}{3} \left[\left(r_k + \frac{\Delta r}{2} \right)^3 - \left(r_k - \frac{\Delta r}{2} \right)^3 \right] \left(\sin\left(\beta_j + \frac{\Delta\beta}{2} \right) - \sin\left(\beta_j - \frac{\Delta\beta}{2} \right) \right). \tag{4.3}$$

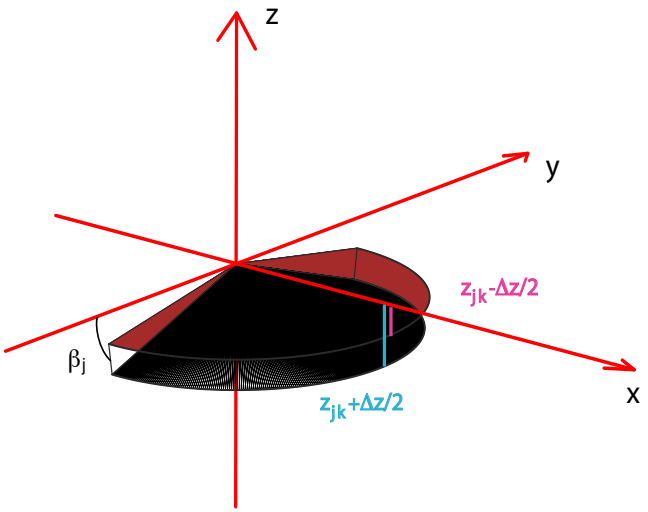

Figure 4.2: Partitioning by conical surfaces from α_i in (4.2).

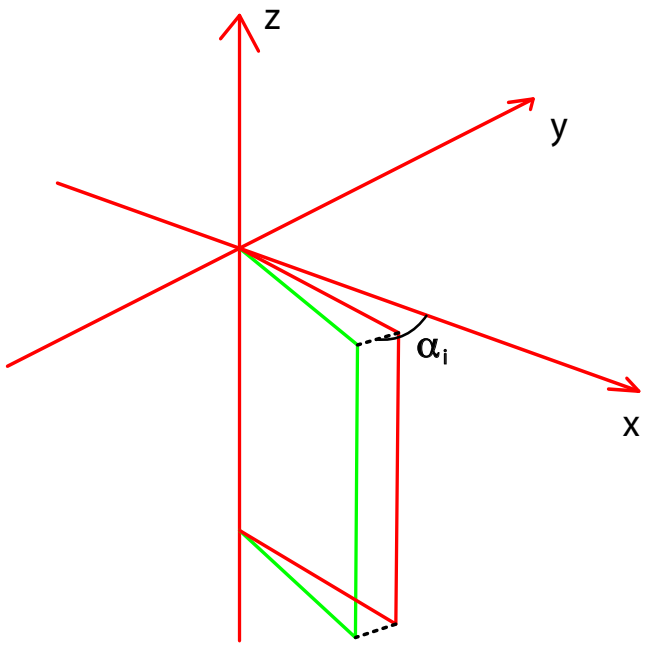

Figure 4.3: Partitioning by plane surfaces from β_j in (4.2).

4.2 Refraction.

Ideally, sound waves move along straight lines, but as shown in chapter 2, temperature- and pressure-changes in the sea, results in refraction of the sound beams. We have found the resulting path of the sound beams, using the iterative algorithm presented in section 2.6.2 on the data set (Røst, 25.01.2006) treated in this thesis. Some computer programming were required to implement the algorithm, which will not be presented here. Figure 4.4 shows the actual path of the beams in the vertical fan having $i = 13$ (straight out on the port side of the vessel), as estimated by the algorithm. We see that the temperature mainly changes in the interval (-25,-60) meters, so that the beams that stay the longest in this interval will be refracted the most. The plot shows that even a small gradient in temperature (1 °C in 35 meters) refracts the beams up to one third of the distance between beams, explaining the importance of winter surveys.

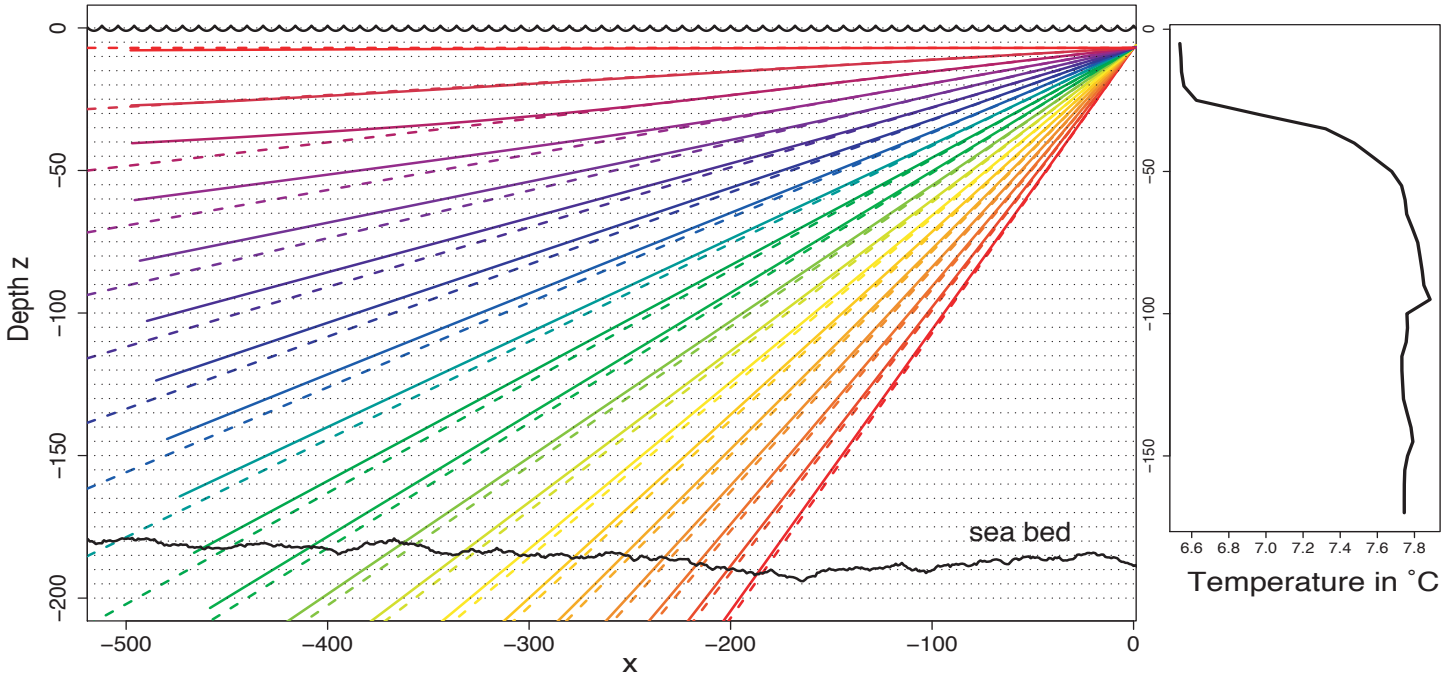

Figure 4.4: Refraction of sound beams in the vertical fan of $i = 13$. Dashed lines are paths for the beams without refraction.

4.3 Transformation to S_v.

The raw output from the MS70 sonar must be transformed by a procedure provided by the manufacturer. This procedure is presented on pages 110-111 in (Eliassen et al., 2003). The resulting values, for the data set treated in this thesis, shows however inconsistencies with what would be expected for the S_v-values (defined in section 2.7) from MS70.

Linear S_v-values seems to have a much more extreme distribution than the exponential distribution, which is what would be expected for several small objects uniformly positioned in a voxel, as will be shown in chapter 6. In addition the logarithmic values are far to low to be explained by known effects. The solution of this problem might be to simply scale the S_v-values by the factor $1/2$. This seems to solve the problem, as seen in Figure 4.5, but thorough investigation of the transformation procedure must be done to justify this scaling.

It is usual to limit the S_v-values to the range $(0, -120)$ dB, which has also been done in the data treated in this thesis. Because of the factor $1/2$, our data are thus limited to the range $(0, -60)$ dB. As we will use $b = 1$ mm$^2 = 10^{-6}$ m^2, the B-values will be in the range $(1, 10^6)$, where $B = 1$ corresponds to one bubble of air of size $b = 1$ mm^2 per cubic meter.

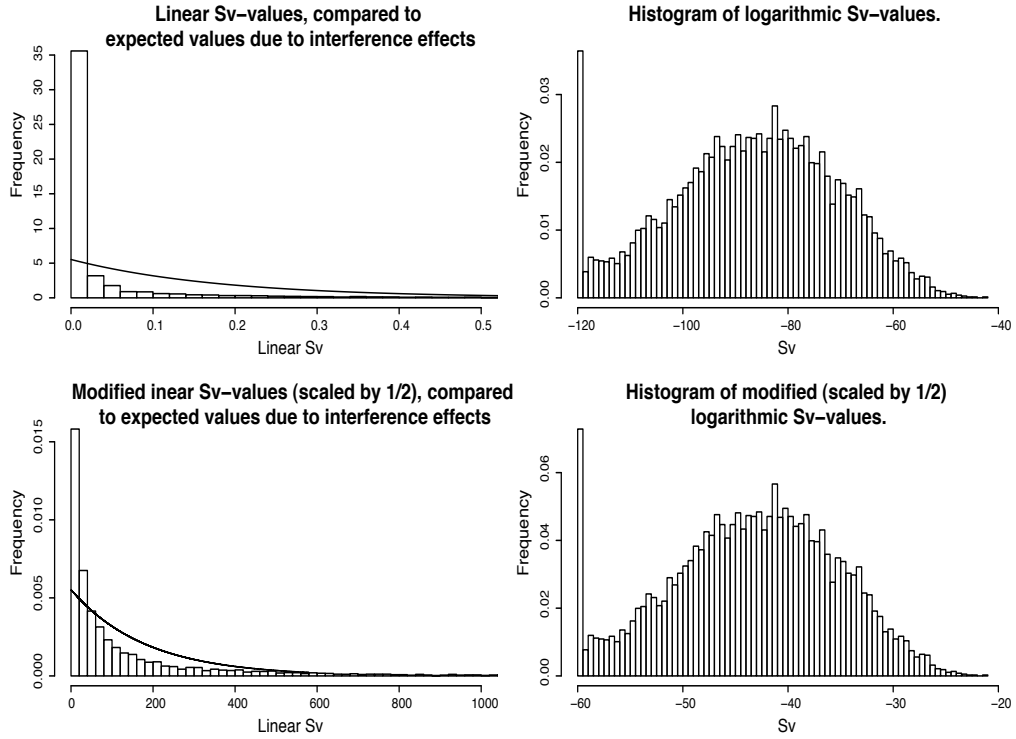

Figure 4.5: Histograms of data from voxels identified as belonging to a school, by the segmentation procedure in the Sonar Explorer. The upper left histogram shows poor fit to the expected variation from interference effects from several fish in a voxel. The upper right histogram shows that most of the values are far below what would be expected for a school, which is between -40 and -50 dB. In the lower histograms S_v-values are divided by 2.

Chapter 5

Noise.

B-values (defined in (2.14)) from the MS70 sonar, can be considered to be of three different types: (1) values from regioins with little or no fish, (2) values from regioins contained in schools, and (3) acoustic and instrument noise. In this chapter we briefly discuss the types of noise that occur in data from MS70, and present an algorithm for removing unnaturally high values, caused by errors in the data stream from the sonar.

5.1 Acoustic noise.

The most obvious sources of acoustic noise are the surface, the bottom, and the transducer itself and the propeller of the vessel. At large distances from the transducer, the attenuation and absorption of the sound reduce the signal so much that the general background noise becomes dominant (see section 2.6.1 for definition of attenuation and absorption).

Noise from the surface.

Because of waves, the surface of the sea is highly irregular, so a sound ray that hits the surface will have a significant noise component in the reflection angle. We thus lose track of the rays, both on the way out from the transducer, and on the way back. The motion of the surface waves also produce bubbles of air in a layer of some thickness depending on the restlessness of the sea. A school located near the surface would thus be subject to significant noise, and might be very difficult to analyze. As described in section 2.6.2 and simulated in the end of the previous chapter, the path of sound rays from MS70 depends on the refraction on the sea, and the depth and tilt angle of the sonar. Based on the resulting depth of the school, we then decide whether the entire school should be excluded

from the analysis. The school treated in this thesis has a minimum depth of ≈ 70 meters, based on the segmentation of the school done by the Sonar Explorer, so surface noise will be insignificant in the analysis.

Bottom noise.

Because of the irregularity of the sea bed, some of the sound will be reflected towards the transducer, giving a bottom noise. An example of this noise is given in Figure 5.1, where the school is plotted in green, and the bottom noise is plotted in orange. As for the surface noise, we decide whether the entire school should be analyzed or not, by its distance to the sea bed. Values from voxels within some distance from the sea bed should not be trusted, but as seen in Figure 5.1, the bottom noise and the school treated in this thesis are clearly separated.

Vessel and transducer noise.

The engine and propeller of the vessel produce noise, which may reflect back to the receiver from fish and other objects in the sea. However, the noise from the vessel is likely to affect the behaviour of fish, rather than the acoustic signal itself. Hence, we rather consider the noise from the transducer, which is caused by the extremely high sound level radiated (more than 206 dB). In Figure 5.1 this is displayed in red. We see that the transducer noise does not extend far into the sound volume, so an exclusion of the nearest 50 meters will be sufficient for avoiding this type of noise.

Background noise at large distances from the transducer.

In Figure 5.1 we clearly see the long distance background noise, caused by the weakening of the signal on the way out from the transducer and on the way back. This is most apparent for the first plots, which are of beams with greater angle with horizontal (more downwards pointing beams). This is because these beams are reflected from the sea bed on the way out from the transducer. The reflection results in a wakening and scattering of the signal, and values for ranges beyond the the bottom, should anyhow not be trusted.

5.2 Instrument noise.

Having excluded the surface zone, the bottom zone, the zone closest to the transducer and values beyond the sea bed, we can concentrate on noise caused by the instrument itself. Sometimes packets are lost in the data stream, which causes voxels to get unnaturally high values. These artificial values appear mainly as sequences along beams, which we call high intensity beams (HIB), but can also appear as walls. In this chapter we only consider HIBs, and in the next section we present an algorithm for removing these HIBs.

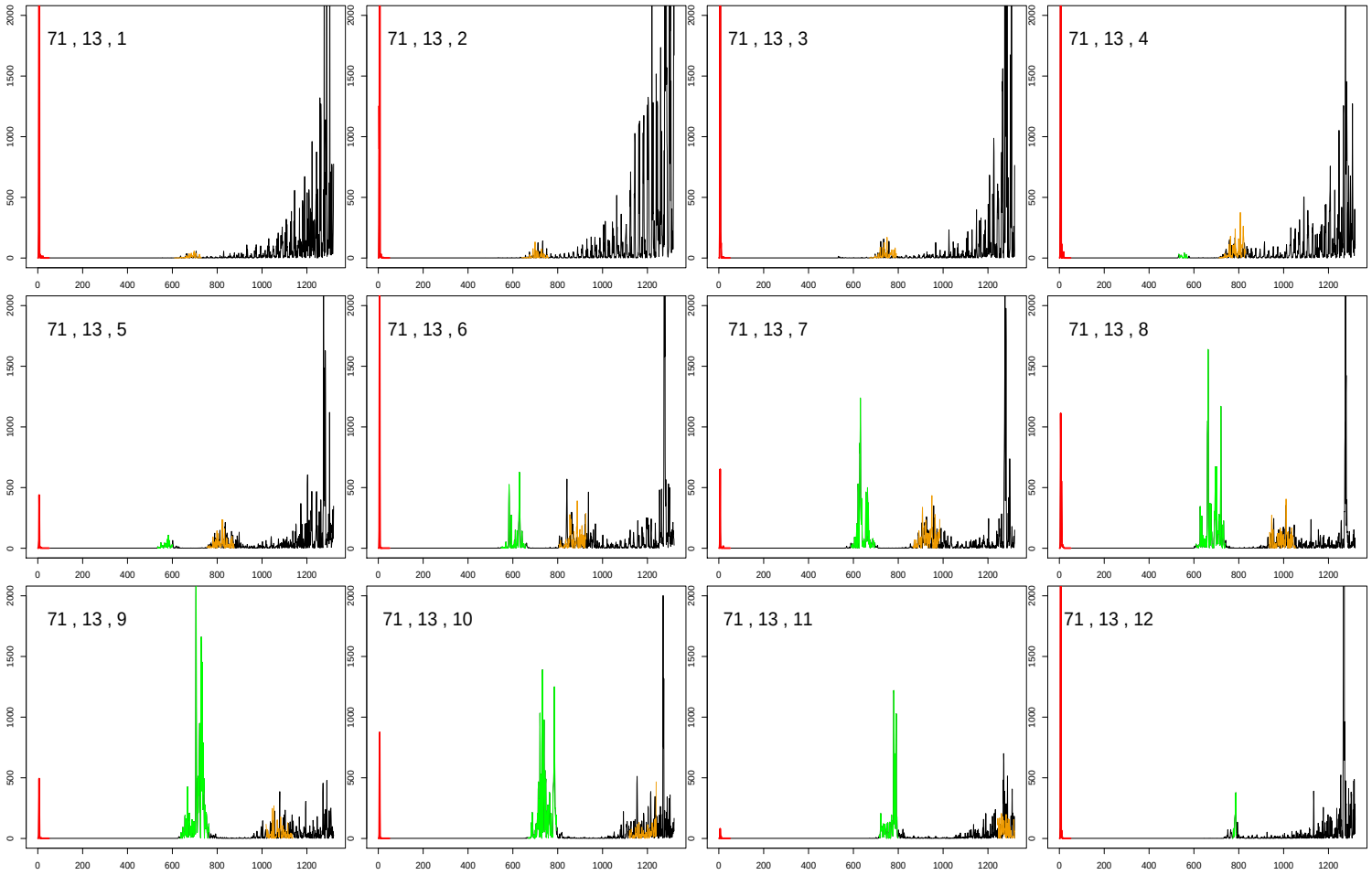

Figure 5.1: An example of noise from the transducer (red) and bottom noise (orange) in the data from MS70. Beams number $(13, 1), (13, 2), \ldots, (13, 12)$ for ping number 71 are plotted. B-values are on the y-axes, and the numbers k of the voxels in the beams are on the x-axes. The school is plotted in green.

5.3 Removal of high intensity beams.

There exists methods developed by the Institute of Marine Research in Bergen, Norway, that consider the ratios of voxels to the mean or median of the voxels in the neighbouring beams at the same distance from the transducer. When this ratio is larger than some predefined level, the value is replaced by the corresponding mean or median of neighbour values. The method we will present here is of a somewhat simpler nature, as it considers ordinary values and not ratios to the neighbouring values. We name the method the "HIB-algorithm".

5.3.1 The HIB-algorithm.

As a premiss for the HIB-algorithm, we have that the nature of the instrument noise is that it involves extremely high B-values. We thus assume that the HIBs differ clearly from ordinary school values. The algorithm involves the following three steps:

1. For the total number N of voxels in question, define a cut point C, and the corresponding empirical probability q that a value is larger than C:

$$q = \bar{Y} = \frac{1}{N}\sum_i Y_i \,, \qquad \text{where} \qquad Y_i = \begin{cases} 1 & B_i > C \\ 0 & B_i \leq C \end{cases},$$

   and B_i is the B-value for voxel number i, $i = 1, \ldots, N$. The cut point C must be chosen large enough so that ordinary b-values from schools are not detected. The lower C the greater chance of identifying school values as HIBs, and the larger C the greater chance of missing values that actually are HIBs. If HIBs are not too frequent, the value of q will be low.

2. Define a minimum number h of consecutive events $B_i > C$ along beams, that permits the sequence of B-values to be classified as a HIB.

   To do this we consider the two variables Z and W, which for an integer n, and a beam of L voxels, are defined as:

$$Z = \sum_{i=1}^{L} Y_i$$

$$W = \text{Number of sequences of } B\text{-values} > C, \text{ of lengths} \geq n.$$

We have that $Z \sim binomial(L, q)$, but we need to find the conditional distribution of W given that $Z = z$:

When $z < n$, the only option is $W = 0$. If $z = n$, sequences of n consecutive B-values larger than C, can appear in $L - n + 1$ different ways. The total number of ways the B-values can be distributed throughout the beam, gives us the probability that $W = 1$ when $z = n$:

$$\mathrm{P}(W = 1|Z = n) = \frac{L - n + 1}{\left(\begin{array}{c} L \\ n \end{array} \right)}.$$

For $z > n$ we consider the probability that $W \geq 1$. If we have a sequence of exactly n consecutive B-values larger than C, we can say that these values occupy $n + 2$ voxels. This is true everywhere along the beam except at the two ends, where the sequence occupy only $n+1$ voxels. We assume that L is large, and approximate by saying that the sequence occupy $n+2$ voxels everywhere. The rest of the B-values that are larger than C, which we call s, are free to be positioned anywhere else than in the occupied voxels. The number of voxels not occupied by the sequence is $L - n - 2$. This scenario can happen in $L - n + 1$ ways, as before.

However, generally there can be $n + d$ consecutive B-values that are larger than C, where $d = 0, \ldots, s$. In this case the sequence occupies $n + d + 2$ voxels (everywhere else than on the ends), and the $s - d$ remaining B-values that are larger than C, are free to be positioned anywhere throughout the $L - n - d - 2$ remaining voxels. Summed up we get the conditional probability that $W \geq 1$ given $Z = z$ as:

$$\mathrm{P}(W \geq 1|Z = z) \approx \sum_{d=0}^{s} \frac{(L - n + 1 - d) \left(\begin{array}{c} L - n - 2 - d \\ s - d \end{array} \right)}{\left(\begin{array}{c} L \\ n + s \end{array} \right)}, \qquad z \geq n.$$

To find the marginal probability that $W \geq 1$, we multiply with $\mathrm{P}(Z = z)$ and sum up to get:

$$\mathrm{P}(W \geq 1|n) \approx \sum_{z=n}^{\infty} \mathrm{P}(W \geq 1|Z = z)\mathrm{P}(Z = z).$$

If we have that $z \geq 2n$, the probability that we get more than one sequence of n or more consecutive B-values that are larger than C, will be much smaller than the probability of having only one such sequence. This is because the value of q usually is small, unless there are many HIBs. We thus approximate the expected number EW of sequences in an arbitrary beam by $\mathrm{P}(W \geq 1|n)$. For a series of pings that we wish to use the HIB-algorithm on, we let N_B be the number of beams, so that the total expected number of sequences is $N_B\mathrm{P}(W \geq 1|n)$

If we define a maximum number M of sequences that we accept as incorrectly classified HIBs, we get

$$h = \min(n : N_B\mathrm{P}(W \geq 1|n) < M).$$

3. Identify all non partial sequences along beams, of voxels satisfying $B_i > C$, and if the length of a sequence is $\geq h$, identify it as HIBs.

4. For a predefined number b, replace all detected HIBs and the b values on both sides of the HIBs, by the median or mean of the voxels in the neighbouring beams, at the same distance from the transducer.

Although HIBs are recognized by large B-values, the voxels in a HIB may start from normal values, and grow into large values, so that a HIB might contain normal values. An example of this is shown in Figure 5.2. The red graph is the beam having a HIB, while neighbouring beams are plotted in other colours. At $k \in (450, 590)$ B-values of the neighbours are below the limit $B = 1$, (see section 4.3), so B-values are set to 1. The HIB starts at $k \approx 470$, and has small B-values until it blends in with the school, and accelerates into extremely high B-values. We thus see the need for the "overlap number" b.

Choosing an appropriate cut point C is a crucial matter, and involves the risk of either passing HIBs through the filter, or classifying normal values as HIBs. Based on Figure 5.2, the value $C = 10000$ would discover the HIB, and accept the school, so we will use this cut point in our filtering of HIBs. The overlap number b also affects the performance of the HIB-algorithm. A large value will have better chance of removing the entire HIB if it also contains moderate values that still are large compared to the neigbouring beams. In Figure 5.2 we see that the HIB extends almost 200 voxels to the left, so for this particular HIB the appropriate value of b would be 200. In the following implementation of the HIB-algorithm, we used $b = 100$ since a value of 200 might be unnecessary large for other HIBs.

The choice of the value of M also has an effect on the performance of the HIB-algorithm. A low value results in a large value of h, so that shorter HIBs may not be detected. A large value of M causes the number h to be small, so that high values that are caused by randomness in the B-values are wrongly identified as HIBs. When implementing the HIB-algorithm we used $M = 0.1$.

5.3.2 Using the HIB-algorithm.

We implemented the HIB-algorithm on the data treated in this thesis, using cut point $C = 10000$, which gave $q = 0.000132$. The overlap number b was set to 100, and M was set to 0.1. We concentrated on the 12 pings which contains the school treated in later chapters, and only the voxels having $k \in (101, 1100)$ were treated, to avoid the transducer noise and the massive background noise at the far end of the sonar volume. The resulting minimum identification length h was 2, so that single B-values larger than 10000 were passed through the filter, but sequences of more than one B-value larger than 10000 were identified as HIBs, and replaced by the median of the neighbouring B-values. Figure 5.3 displays HIBs before and after filtration, in black and red respectively. Beam number (18,9) for ping 71 is plotted with the y-axis limited to the range (0,500), to show the result of the HIB-algorithm.

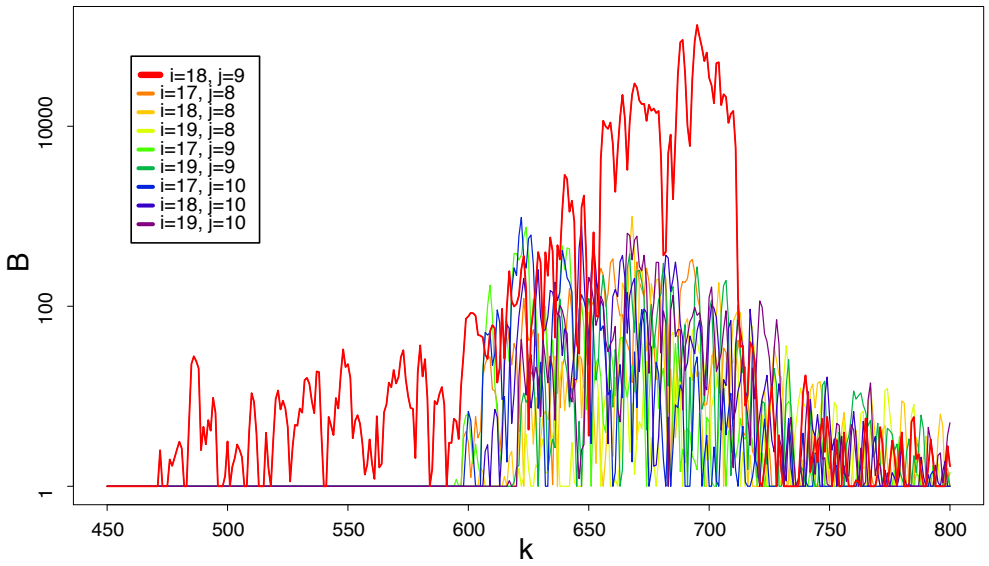

Figure 5.2: A HIB in beam number (18,9) for ping number 71, plotted in red. The 8 surrounding beams are plotted in other colours. The HIB starts outside of the school, and extends throughout the school. We see that the HIB blends in with the school for $k \in (610, 650)$.

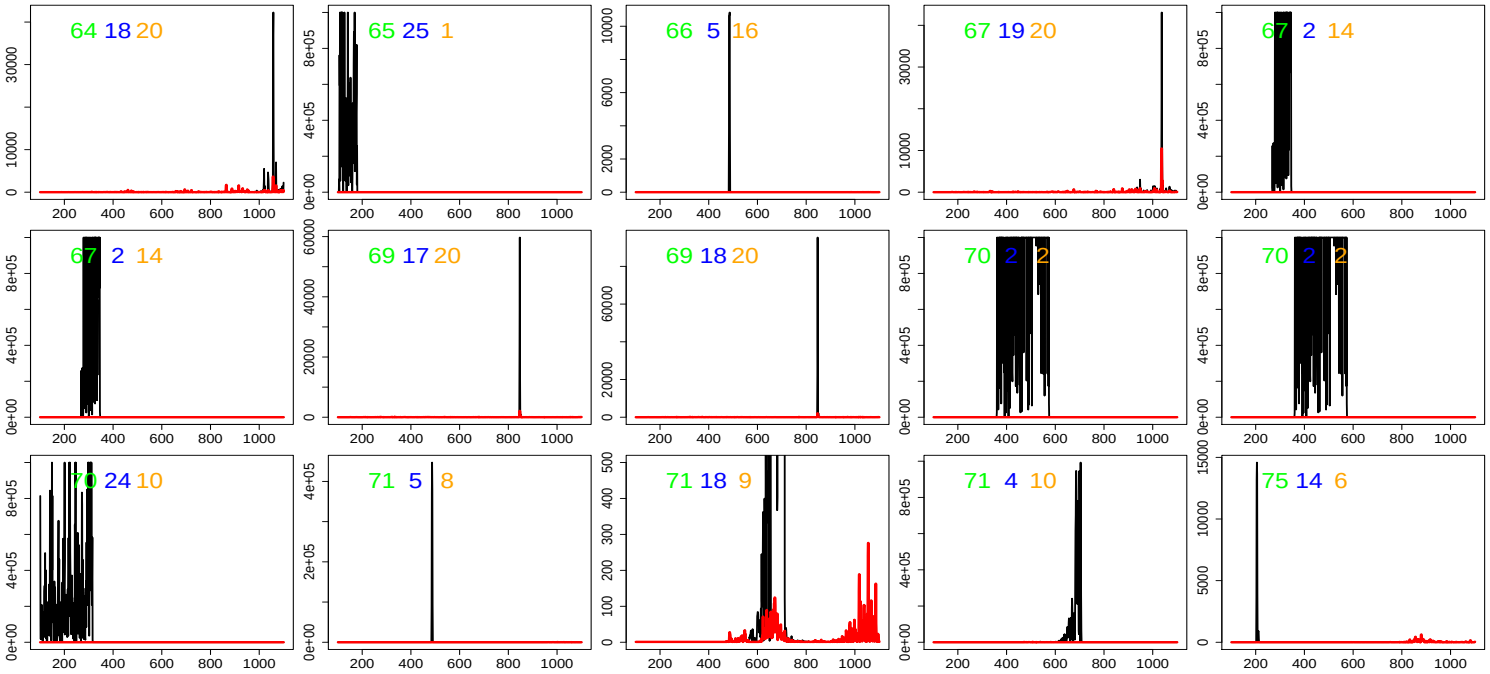

Figure 5.3: The HIB-algorithm used on data from MS70. Values before filtering are plotted in black, and values after are plotted in red.

Chapter 6

Individual backscattering model.

6.1 Backscattering from individual fish.

One approach to analyzing the B-values (confront (2.13)) in datasets from multibeam sonars, is to look at the individual backscattering from fish. In this chapter we reveal the sources of variation in the data from schools, aiming to explain the variation in the real data from a school observed by the MS70 sonar. The histogram of all B-values identified as belonging to the school treated in this thesis is shown in Figure 6.1. The shape of the plot has similarities with the exponential distribution (plotted in red), but appears more *extreme* than this distribution. Without knowledge of the acoustics behind the B-values, one could believe that this shape of the histogram was caused only by the distribution of fish in the school. We would then have few fish in most of the voxels, and many fish in just a few of the voxels. However, this conflicts with the individual based models (IBMs) discussed in Chapter 1, where fish has preferred distances to neighbouring fish in a school. To explain this inconsistency we will analyze the randomness in the B-values, caused by random size, position and orientation of individual fish, and interference between acoustic signals from several fish. We will see that the interference generally dominates the randomness, providing a probability distribution for the B-values close to the exponential distribution.

Figure 6.2 shows the plot of the randomly chosen beam number $(6, 10)$ for ping 12, together with the moving average of 15 values along the beam centered at each voxel. The beam cuts through the school at an angle $23.68°$ with horizontal, as calculated from (3.1). Because of the randomness in the B-values, the moving average values will estimate the acoustic backscattering ability of the objects in the voxles better than the individual B-values. The variations in the moving average values must be caused either by (i) changes in the number of fish in the voxels, by (ii) changes in size, position and orientation of the fish, by (iii) randomness in the moving average values, or by a combination of the three. Because of the angle $23.68°$, the beam will gradually encounter the school, and gradually leave the school, so lower values are expected at the beginning and at the end of the beam in Figure 6.2. If we assume that fish in the school interact

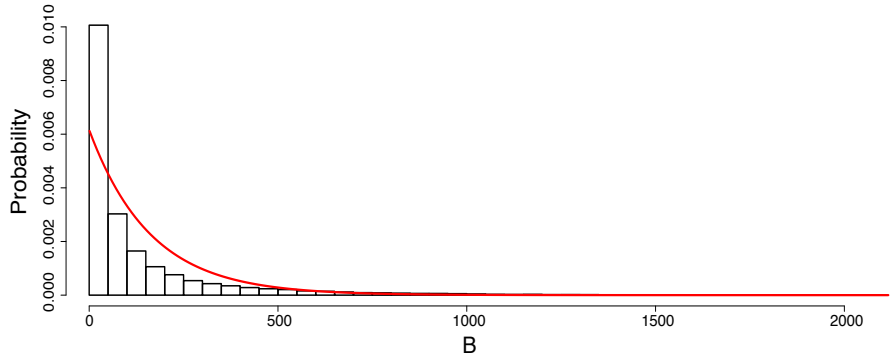

Figure 6.1: Histogram of all B-values in the school. The red line is the exponential distribution of mean equal to mean of the B-values.

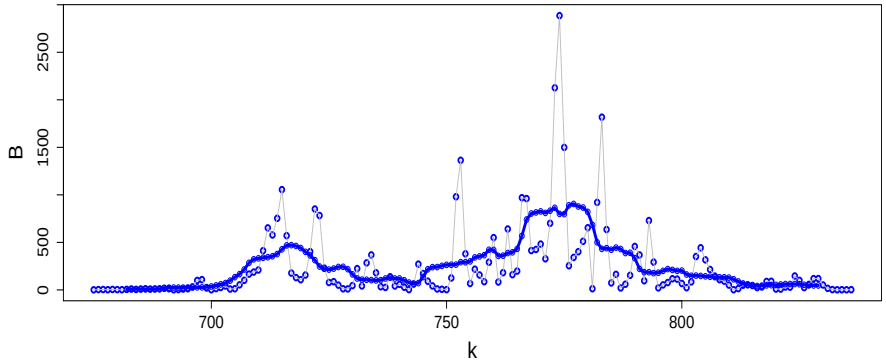

Figure 6.2: Plot of the values identified as belonging to the school in beam number $(6, 10)$ for ping number 12. Moving average values of 15 values along the beam centered at each voxel are plotted in blue.

according to the rules defined in an IBM, as given in Chapter 1, other variations must be related to (ii) and (iii). Assuming that the B-values are exponentially distributed, the coefficient of variation (ratio of standard deviation and mean) of the moving average values is 1/15, so that variations larger than this randomness must be caused by (ii). However, a school might be patchy, so that (i) may still contribute to the variations in the moving average values, even inside the school.

In this chapter we will first concentrate on the backscattering from one fish, and then generalize to more than one fish, taking interference effects into account. Using a model for the acoustic backscattering from more than one fish, and the specification of voxels done in chapter 4, we will perform computer simulations aiming to quantify the randomness in the B-values from the MS70 sonar. We also simulate the autocorrelation between neighbouring voxels in beams, based on this model.

6.1.1 One fish in the sound field of a transducer.

The acoustic intensity from a fish at the receiver is a function of the acoustic properties of the transducer, the acoustic properties of the fish, the position of the fish with respect to the transducer, and the position of the receiver with respect to the fish. The intensity that strikes the fish produces a scattered sound field radiating from the fish, with a specific beam pattern, as seen in Chapter 2. Figure 6.3 shows a situation where a transducer radiates sound that is scattered by a an object formed as a line. This gives a beam pattern from the line source which suggests that the orientation of the fish is relevant for the intensity at the receiver. We will in this section try to create a stochastic model describing the intensity received from the backscattering produced by a single fish.

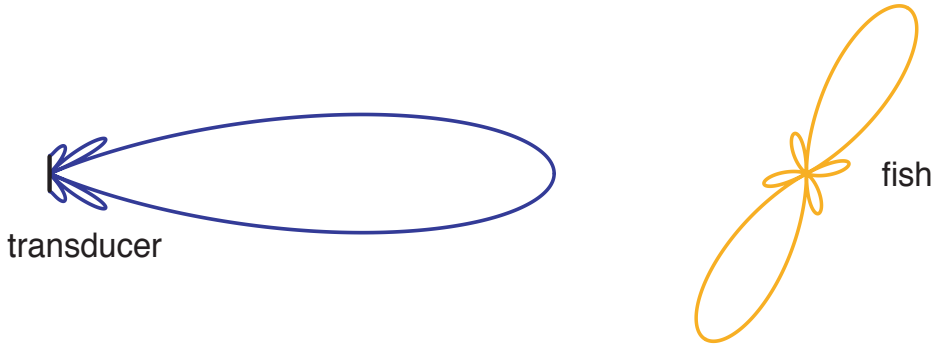

Figure 6.3: Beam pattern for the acoustic pressure from the transducer and beam pattern for the acoustic pressure of the scattered sound from a line source representing the fish. In the figure, maximum pressure will strike the fish, but the maximum of the pressure from the fish will miss the receiver.

One may claim that every species has its own specific beam pattern. Given the acoustic energy striking the fish per second, the length S of the fish and the frequency f of the sound, this will be a spatial function of orientation $\Omega = (\alpha^F, \beta^F)$ of the fish, specific for each species. We define orientation as the angles $\theta = \alpha^F$ and $\phi = \beta^F$ of the unit vector in the direction of the fish (from the tail to the nose), as represented in the coordinate system of the vessel (Figure 6.5). This definition might be a bit unnatural, since the fish primarily moves in the global coordinate system of the sea, but calculations are simpler with this definition, and transformations from the global coordinate system to the coordinate system of the vessel will be done in Chapter 7. The acoustic energy striking the fish per second will in turn be a function of the length S of the fish, the position $\mathbf{X} = (X_X, Y_X, Z_X) = (r, \theta, \phi)$ of the fish, and the orientation Ω of the fish. We wish to describe these two functions, regarding them as stochastic functions of the the stochastic variables S, $\mathbf{X}$ and Ω.

Firstly we define the two coordinate systems to be used in the discussion, one for the research vessel and one for the fish, displayed in Figure 6.4 and Figure 6.5. The coordinate system of the vessel is simply the cartesian/spherical coordinate system with the direction of the vessel along the y-axis, and with a horizontal x-axis. The fish has a similarly defined coordinate system (indexed with prime), where the orientation Ω defines the y'-axis, and the x-axis is horizontal. This means that the fish is unable to roll, which simplifies the transformations between the two coordinate systems. Both the directions of the vessel and the fish has spherical angles $(\theta, \phi) = (\pi/2, \pi/2)$, and $(\theta', \phi') = (\pi/2, \pi/2)$ respectively. The rotation of the coordinate system of the fish with respect to that of the vessel, is an z-x-rotation, and we call the rotation angles (a, b).

Since the y'-axis is defined to be in the direction of the fish, we need some attention to find a relation between the angles (a, b) of the rotation, and the angles (α^F, β^F) of the orientation of the fish. Because the fish has orientation $(\pi/2, \pi/2)$ when heading in the same direction as the vessel, additional rotations a and b give us the orientation (α^F, β^F) of the fish. However, the rotation b is defined in the opposite direction of ϕ in the coordinate system of the vessel, so we end up with the connection $(\alpha^F, \beta^F) = (\pi/2, \pi/2) + (a, -b)$. Summed up, the coordinate system of the fish is a translation $\mathbf{X}$ and an z-x-rotation by the angles $(a, b) = (\alpha^F - \pi/2, \pi/2 - \beta^F)$ of the coordinate system of the vessel. A point vector $\mathbf{v}$ in the coordinate system of the vessel, transformed into the coordinate system of the fish, is thus

$$\mathbf{v}' = \mathbb{A}_{zx}\left(\alpha^F - \pi/2, \pi/2 - \beta^F\right)(\mathbf{v} - \mathbf{X}), \tag{6.1}$$

where the rotation matrix $\mathbb{A}_{zx}(a, b)$ is defined in Appendix A.

Applying this transformation we can find the angles θ' and ϕ', from the angles θ and ϕ. We consider the unit direction vector $\mathbf{d} = (1, \theta, \phi)$ of the position of the fish, which in the coordinate system of the fish, before the fish has been rotated, will be $\mathbf{d}'_0 = -\mathbf{d}$ (looking at the vessel from the fish). Rotation then gives us:

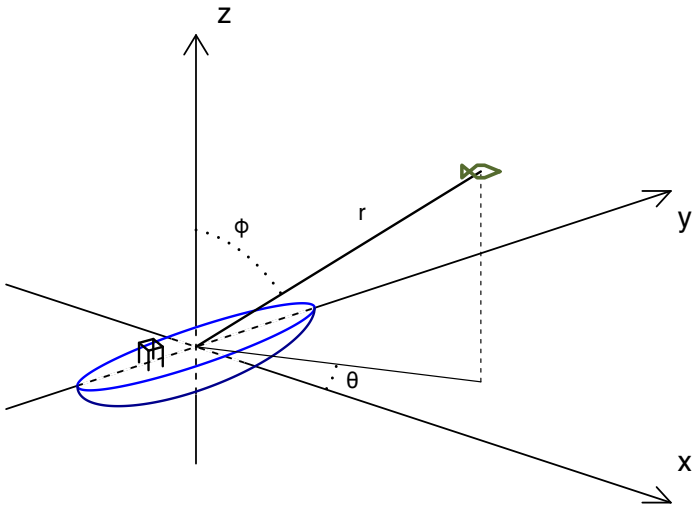

Figure 6.4: The coordinate system with respect to the research vessel. The position vector $\mathbf{X} = (X_X, Y_X, Z_X) = (r, \theta, \phi)$ is located in the air for illustrative purposes. Unless $\mathbf{X}$ is the position of a flying fish, Z_X will be negative.

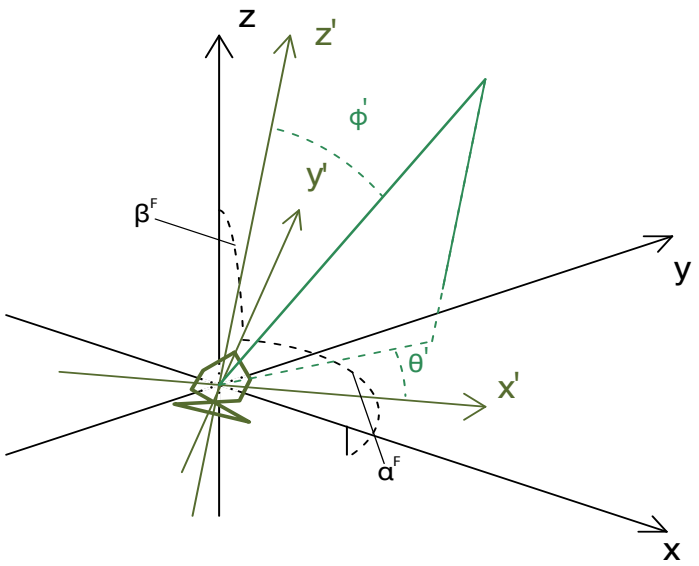

Figure 6.5: The orientation $\Omega = (\alpha^F, \beta^F)$ of the fish.

$$\mathbf{d}' = \mathbb{A}_{zx}\left(\alpha^F - \pi/2, \pi/2 - \beta^F\right)\mathbf{d}'_0$$

$$\Downarrow$$

$$\theta' = \operatorname{atan}\left(\frac{d'_y}{d'_x}\right) \qquad \phi' = \operatorname{atan}\left(\frac{\sqrt{d'^2_y + d'^2_y}}{d'_z}\right). \tag{6.2}$$

If the fish has a swim bladder, this will be the main source of the echo from the fish. Swim bladders are usually oblong, along with the rest of the fish, so in any case we may consider the echo from the fish to be the result of an oblong object. In the next section we will thus look at the theoretical pressure field from a line source, representing the fish. In this case we need the angle γ' of incidence to the line source, which is the angle between a point vector, and the plane perpendicular to the direction of the fish/swim bladder. We solve this task by rotating the coordinate system of the fish an additional $-\pi/2$ around the x-axis, thus representing the point vector $\mathbf{d}_0$ in a system with z-axis along the direction of the fish. The resulting rotation matrix $\mathbb{A}_\gamma = \mathbb{A}_{zx}\left(\alpha^F - \pi/2, -\beta^F\right)$ gives us then the point vector $\mathbf{d}^\star$, which transformed from cartesian to spherical coordinates provides us with the angle between the fish direction, and the point vector in question (direction of the sonar). Subtracting this angle from $\pi/2$ then results in γ':

$$\mathbf{d}^\star = \mathbb{A}_\gamma \mathbf{d}'_0 \qquad \Rightarrow \qquad \gamma' = \frac{\pi}{2} - \operatorname{atan}\left(\frac{\sqrt{(d^\star_x)^2 + (d^\star_y)^2}}{d^\star_z}\right). \tag{6.3}$$

For a fish with swim bladder, there may be a tilt angle τ between the swim bladder and the direction of the fish, so that we need to add τ to the angle β^F in all rotations.

6.1.2 Directional factor.

The main source of acoustic echo from a fish is the swim bladder. Because of the large difference in density to the surrounding flesh of the fish, there is almost total reflection at this boundary. For fish without swim bladder the flesh and bones produce a much weaker echo.

Because the swim bladder/fish is an oblong object, we may represent the fish as a cylindrical line source, with pressure amplitude given by (2.7):

$$p\left(r',\gamma'\right) = \rho_0 c U_0 \frac{\kappa_a}{2}\frac{L}{r}\left(\frac{\sin\left(\frac{1}{2}kL\sin\gamma'\right)}{\frac{1}{2}kL\sin\gamma'}\right),$$

for the distance r and the angle γ' with the plane orthogonal to the line source (with prime referring to angle with respect to the fish/line source), where $\rho_0 c$ is the specific acoustic impedance of the ocean, U_0 is the speed amplitude of the surface of the pulsating line source, a and L are the radius and length of the line source and $\kappa_a = \cos\phi_a e^{-i(ka+\phi_a)}$ is explained in section 2.3. Since the transducer in the MS70 sonar is also the receiver, we will use r to represent distances in the coordinate system of the fish (instead of r').

The directional factor defined in section 2.4, (with subscript denoting the fish),

$$H_F\left(\gamma'\right) = \frac{\sin\left(\frac{1}{2}kL\sin\gamma'\right)}{\frac{1}{2}kL\sin\gamma'}, \tag{6.4}$$

produces a beam pattern as the one from the line source in Figure 6.3, and increases in complexity as the length of the fish or/and the wave number $k = \frac{2\pi f}{c}$ increases. This increase in complexity of the sound field is documented by (Towler et al., 2003), where 425 mm walleye pollock, and 134 mm capelin was exposed to sound of 38 kHz and 120 kHz frequency. Smaller fish and lower frequency results in a less complex directional factor, and the fish increasingly resembles a point source.

To represent the fish by the simple line source model would however not be completely accurate. The beam pattern could instead be found numerically, by integrating the contributions from many small plane surface elements on the swim bladder. In this chapter we will still use the line source model, since it is simple, and reflects much of the acoustic properties of the fish/swim bladder. In general, the oblongness of the fish/swim bladder provides higher intensity perpendicular to the direction of the fish/swim bladder, as provided by the line source model.

As claimed in the beginning of section 6.1.1, every species has a specific beam pattern. The differences between species are caused by differences in the tilt angle τ of the swim bladder, by differences in the shape and size of the fish/swim bladder, and by the fact that some species do not have a swim bladder. We thus consider the directional factor as being an empirical function $H_F(\theta', \phi')$ of the angles θ' and ϕ' in the spherical coordinate system of the fish displayed in Figure 6.5. As in the theoretical case, $H_F(\theta', \phi')$ should be dependent on wave number k and length S of the fish. In practice one would like to simplify the directional factor, maybe by some combination of polynomial functions.

For fish with swim bladders there is also a depth dependence. The swim bladder volume has been shown to decrease with depth, due to compression from the hydrostatic pressure and diffusion through the walls of the swim bladder. We will later show that this dependence

follows Boyle's law for volume and pressure in an enclosed system at constant temperature. The compression will of course reduce the amount of acoustic energy scattered by the fish, but may also affect the directional factor of the fish. However, we will here assume that the effect of depth compression on the directional factor is negligible, as (Ona, 2003) provide evidence that the endpoints of the swim bladder are fixed.

Throughout the thesis we mainly consider the acoustic intensity, so referring to (2.8) we express the directional factor in terms of the acoustic intensity:

$$B_F\left(\theta',\phi'\right) = B_F\left(\theta',\phi',k,S\right) = \left[H_F\left(\theta',\phi',k,S\right)\right]^2 \qquad \text{(empirically)}. \tag{6.5}$$

$$B_F\left(\gamma'\right) = B_F\left(\gamma',k,S\right) = \left[H_F\left(\gamma',k,S\right)\right]^2 \qquad \text{(theoretically)}. \tag{6.6}$$

where the length S of the fish represents the length of the line source. Obviously every fish of the same size and species may not have the exact same directional factor, because of individual differences in the configuration of the fish. However we assume that these differences are negligible.

6.1.3 Maximum amplitude.

We turn our attention to the line source representing the fish, and examine the axial pressure amplitude at a distance r from the fish:

$$P_{ax}\left(r\right) = \frac{-i}{2}\rho_0 c U_0 \frac{a}{r} kL.$$

The axial pressure $P_{ax}(r)$ can be regarded as the strength of the source compared to the radiation medium, divided by the distance r from the source. The analogous interpretation of the axial *intensity* will be the power of the source compared to the medium, divided by the squared distance r^2 from the source. If we name the acoustic energy scattered per second from a real fish as $E/\Delta t = \Pi$ (the power), this will be equal to the surface integrated intensity from the fish on the sphere having $r = 1$:

$$\Pi = \oint_{r=1} I_F\left(r,\theta',\phi'\right) ds = I_{max}(1) \oint_{r=1} B\left(\theta',\phi',k,S\right) ds = \psi(k,S) I_{max}(1), \tag{6.7}$$

where $I_F\left(r,\theta',\phi'\right)$ is the acoustic intensity from the fish, $I_{max}(1)$ is the maximum acoustic intensity from the fish on the unit sphere in the lossless case (where we have dropped the subscript F for simplicity), and $\psi(k,S)$ is the surface integral of the directional factor at $r=1$. Since the directional factor $B\left(\theta',\phi',k,S\right)$ for the fish is dependent on the wave number k and the size S of the fish as given in (6.5) and (6.6), $\psi(k,S)$ also poses these dependencies. For a simple source ψ is simply the area 4π of the unit sphere (where we omit the dependency on k and S to ease notation), and for all other beam patterns $\psi < 4\pi$.

The maximum acoustic intensity at the distance r from the fish will thus be

$$I_{max}\left(r\right) = \frac{I_{max}\left(1\right)}{r^2} = \frac{\Pi}{\psi r^2}.$$

This expression for the maximum acoustic intesity is only true in the lossless case. As stated in section 2.6.1 the transmission loss due to absorption in the sea will reduce intensity exponentially. We write this as

$$I_{\max}\left(r\right) = \frac{\Pi}{\psi r^2} \cdot 10^{-\alpha r},$$

where α is the absorption coefficient specific for the properties of the radiation medium (as defined in section 2.6.1).

The energy scattered by the fish per second, will be equal to the product of acoustic intensity at the fish from the transducer, and cross sectional area $A_s(Z_X,\Omega)$ of an imaginary object of air scattering the same amount of sound as the fish does. Because the fish/swim bladder is an oblong object, $A_s(Z_X,\Omega)$ is dependent on orientation Ω. If the fish has a swim bladder, there will also be a dependency on depth Z_X due to compression of the swim bladder. If we define an optimal cross sectional receiving area A_0 at depth $Z_X = 0$, a depth compression factor η_c, and an orientation factor η_Ω, we can write $A_s(Z_X,\Omega) = A_0\eta_c\eta_\Omega$:

$$\Pi = I_T A_s(Z_X,\Omega) = I_T(r)A_0\eta_c\eta_\Omega, \tag{6.8}$$

where I_T is the intensity from the transducer at the fish. Combining (6.7) and (6.8), we get

$$\frac{A_0\eta_c\eta_\Omega}{\psi} = \frac{I_{max}(1)}{I_T}.$$

From the definition of optimal scattering cross section in (2.12), we see that the ratio $I_{max}(1)/I_T(r)$ is equal to $\sigma_0/4\pi$, so we can express the maximum acoustic intensity from the fish in terms of σ_0:

$$I_{\max}(r) = \frac{I_T A_0\eta_c\eta_\Omega}{\psi}\frac{10^{-\alpha r}}{r^2} = \frac{I_T\sigma_0}{4\pi}\frac{10^{-\alpha r}}{r^2}, \tag{6.9}$$

where the optimal scattering cross section is

$$\sigma_0 = \frac{4\pi A_0\eta_c\eta_\Omega}{\psi}. \tag{6.10}$$

In the following section we will express η_c as a function of depth Z_X, η_Ω as a function of position $\mathbf{X}$ and orientation Ω, and A_0 as a function of size S of the fish, all related to the species of the fish.

6.1.4 Acoustic intensity scattered by the fish.

A_0 as a function of size S.

The fish size has an important effect on the optimal cross sectional receiving area A_0 of the imaginary object of air scattering the same amount of sound as the fish does. Since the swim bladder is the main source of acoustic scattering, we will concentrate on this in the following.

Acoustic scattering from the swim bladder is dependent on the frequency and intensity of the received sound, the shape of the swim bladder, and the size of it compared to the wavelength of the received sound. The effect on scattering from frequency and size, is different for frequencies below, at or above resonance frequencies. For herring with swim bladder dimensions a=0.5 cm and L=4 cm, the first resonance frequency will be approximately $f_1 = c_{\text{swimbladder}}\frac{2}{L} \approx 4200$ Hz, which is far below the frequencies used in the MS70 sonar (75 - 112 KHz). (This can be shown by examining a rectangular cavity, but will not be done in this thesis). We will thus concentrate on the size dependency for high frequencies, where the frequency itself has little effect on the acoustic scattering.

As a simple relation, we propose that as the size S of the fish changes, the volume of the swim bladder changes threefold, and the optimal cross sectional area of the swim bladder changes twofold. A fish of size twice the size of another fish, will have four times the cross sectional swim bladder area as the little fish. If the fish in question lacks swim bladder, the optimal cross sectional area of the *fish* changes twofold as S changes, so generally we have that

$$A_0 = \varepsilon S^2,$$

where ε is a proportional coefficient specific for each species. This relation is a special case of the empirical equation (1) in (Love, 1977) (setting the exponent of the ratio of fish length and wavelength equal to 2).

η_c as a function of depth Z_X.

As mentioned above, there is a depth dependence on the size of swim bladder due to compression and diffusion. (Gorska and Ona, 2003a) proposes that this dependence, in the case off herring, follows Boyle's law,

$$pV = \text{constant} \qquad \Longrightarrow \qquad V\left(Z_X\right) = V_0 \frac{p_0}{p\left(Z_X\right)},$$

with $p_0 = 101325$ Pa (Pascal) being pressure at sea level and V_0, volume of the swim bladder for a fish at the surface. If we assume that the swim bladder is cylindrical, with radius a and length L, we can write this as

$$\pi\, a\left(Z_X\right)^2 L\left(Z_X\right) = \pi a_0^2\, L_0 \frac{p_0}{p\left(Z_X\right)}.$$

The compression can be decomposed to length compression and radial compression, so we rewrite the ratio $p_0/p\left(Z_X\right)$. The pressure in sea water follows the relation $p(Z_X) = p_0 + \rho_0 g Z_X$, where gravity outside the coast of Norway is approximately $g = -9.82 m/s$, and where ρ_0, the density of sea water, is $1027 kg/m^3$ on average, but depending on salinity and temperature. We end up with

$$a\left(Z_X\right)^2\ L\left(Z_X\right) = a_0^2\, L_0 \frac{p_0}{p_0 + \rho g Z_X} = a_0^2 \left(\frac{1}{1 - 0.0995 Z_X}\right)^{2\gamma_a} \cdot L_0 \left(\frac{1}{1 - 0.0995 Z_X}\right)^{\gamma_L}, \tag{6.11}$$

where a_0 and L_0 are the radius and length of the swim bladder at depth $Z_X = 0$, and γ_a and γ_L are compression factors satisfying $2\gamma_a + \gamma_L = 1$.

The Boyle's law relationship was investigated by (Ona, 1990), where herring was traced at varying depths. The results displayed a reduction in swim bladder volume that exceeded what would be expected from Boyle's law. This deviation from theory was explained as diffusion through the walls of the swim bladder, but in this discussion we will discard that effect, and assume the strict depth dependence stated in (6.11).

The cylinder assumption assures us that the depth compression is independent on ϕ' in the coordinate system of the fish. In practice an ellipsoid might be more accurate, giving different compression factors in all three directions. Using the cylinder model we get the factor to compensate for depth compression

$$\eta_c = \left(\frac{1}{1 - 0.0995 Z_X} \right)^{\gamma_A}, \tag{6.12}$$

where $\gamma_A = \gamma_a + \gamma_L$. If we assume that $\gamma_a = \gamma_L = 1/3$, (6.12) becomes

$$\eta_c = \left(\frac{1}{1 - 0.0995 Z_X} \right)^{2/3}.$$

For fish without swim bladder the compression due to hydrostatic pressure will of course not have an effect, resulting in γ_A being close to 0.

η_Ω as a function of position X and orientation Ω.

Since the swim bladder as well as the fish, is an oblong object, orientation of the fish affect the cross sectional area of either the swim bladder, or the fish itself if it does not have a swim bladder. We discuss the case were the fish has a swim bladder, and as before we assume that it is cylindrical, but in addition we say that the ends of the cylinder are rounded by hemispheres. This way the *cross sectional area* of the swim bladder will always be the cross sectional area of the sphere with radius a, added a projected rectangle of width $2a$ and length depending on the orientation. If we project the vector between the two centers in these hemispheres, called $\mathbf{h}$, onto the plane perpendicular to the position vector $\mathbf{X}$, we get the length of this rectangle.

As mentioned before, the swim bladder can make a tilt angle τ with respect to the orientation of the fish. We define this tilt angle to

increase as the swim bladder points downwards compared to the orientation of the fish. The spherical coordinates of the vector $\mathbf{h}$ are thus $(L - 2a, \alpha^F, \beta^F + \tau)$.

The simplest way to get the length of the desired projected rectangle is to project $\mathbf{h}$ onto $\mathbf{X}$, and then use the resulting triangle to find the length of the projection (see Figure 6.6). Projection of $\mathbf{h}$ onto $\mathbf{X}$ is given by the dot product:

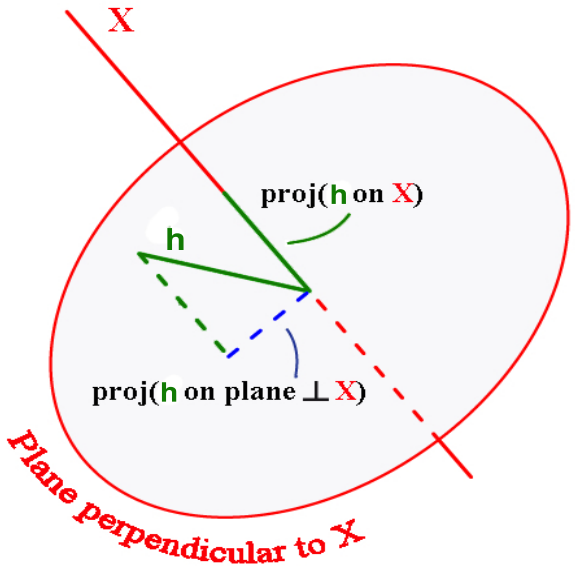

Figure 6.6: Projection of a vector $\mathbf{h}$, onto the plane perpendicular to the vector $\mathbf{X}$.

$$\text{proj}\,(\mathbf{h} \text{ on } \mathbf{X}) = \frac{\mathbf{h} \cdot \mathbf{X}}{|\mathbf{X}|} = \frac{(X_h, Y_h, Z_h) \cdot (X_X, Y_X, Z_X)}{\sqrt{X_X^2 + Y_X^2 + Z_X^2}}$$

$$= \frac{(L-2a)\sin\left(\beta^F + \tau\right)\cos\alpha^F \cdot r\sin\phi\cos\theta + (L-2a)\sin\left(\beta^F + \tau\right)\sin\alpha^F \cdot r\sin\phi\sin\theta + (L-2a)\cos\left(\beta^F + \tau\right) \cdot r\cos\phi}{r}$$

$$= (L-2a)\left[\sin\left(\beta^F+\tau\right)\cos\alpha^F\sin\phi\cos\theta+\sin\left(\beta^F+\tau\right)\sin\alpha^F\sin\phi\sin\theta+\cos\left(\beta^F+\tau\right)\cos\phi\right].$$

Pythagoras leads us then to the relation

$$\text{proj}\left(\mathbf{h}\text{ on plane }\perp\text{ to }\mathbf{X}\right)^2+\text{proj}\left(\mathbf{h}\text{ on }\mathbf{X}\right)^2=(L-2a)^2,$$

with the result

$$\text{proj}\left(\mathbf{h}\text{ on plane }\perp\text{ to }\mathbf{X}\right)=(L-2a)\sqrt{1-\left(\sin\left(\beta^F+\tau\right)\cos\alpha^F\sin\phi\cos\theta+\sin\left(\beta^F+\tau\right)\sin\alpha^F\sin\phi\sin\theta+\cos\left(\beta^F+\tau\right)\cos\phi\right)^2}.$$

We now assume that the cross sectional swim bladder area corresponds to $A_S(Z_X,\Omega)$ of the imaginary object of air scattering the same amount of sound as the fish does, so that

$$A_S(\alpha^F,\beta^F,\tau,\theta,\phi)=\pi a^2+2a\cdot(L-2a)\sqrt{1-\left(\sin\left(\beta^F+\tau\right)\cos\alpha^F\sin\phi\cos\theta+\sin\left(\beta^F+\tau\right)\sin\alpha^F\sin\phi\sin\theta+\cos\left(\beta^F+\tau\right)\cos\phi\right)^2},$$

where we have omitted the dependency on depth Z_X. If we express the length L of the swim bladder as a multiple of the radius a, $L=b\cdot a$, we end up with a factor η_Ω for the projection of the swim bladder onto the plane perpendicular to the position vector $\mathbf{X}$:

$$\eta_\Omega=\frac{\pi+2\,(b-2)\sqrt{1-\left(\sin\left(\beta^F+\tau\right)\cos\alpha^F\sin\phi\cos\theta+\sin\left(\beta^F+\tau\right)\sin\alpha^F\sin\phi\sin\theta+\cos\left(\beta^F+\tau\right)\cos\phi\right)^2}}{\pi+2\,(b-2)},\tag{6.13}$$

which only holds for $b\geq 2$, and where we have divided by $A_0=\pi a^2+2a\,(L-2a)=a^2(\pi+2\,(b-2))$, the cross sectional area of the

swim bladder at optimal incidence. We call this factor the "aspect factor".

For fish without swim bladder we assume that this factor has an analog form, but where A_0 is the cross sectional area of an the imaginary swim bladder object of air scattering the same amount of sound as the fish does (imaginary swim bladder).

6.1.5 Acoustic intensity from the transducer at the fish.

The position of the fish strongly affects the acoustic intensity experienced by the fish. In section 2.5, we presented the pressure from a circular piston in (2.9):

$$p\left(r,\gamma\right)=\rho_0 c U_0 \frac{\kappa_a}{2}\frac{a}{r}\left(\frac{2J_1\left(ka\sin\gamma\right)}{ka\sin\gamma}\right)=P_{ax}\left(r\right)H\left(\gamma\right),$$

for the distance r and the angle γ to the normal vector of the piston. U_0 is the speed amplitude of the surface of the piston, $\rho_0 c$ is the specific acoustic impedance of the ocean, a is the radius of the circular piston, and J_1 is the Bessel function of the first kind.

However, the beams in the MS70 sonar are created by weighting neighbouiring elements, in order to get narrow beams and weak side-lobes. The resulting directional factor will be a function of θ^T and ϕ^T (with superscript T referring to the transducer), in a spherical coordinate system centered at the transducer (one of the 500 elements of the sonar), with z-axis along acoustic maximum, and horizontal x-axis. Accounting for the absorption of the sea and geometric attenuation, we write the acoustic intensity in a beam as

$$I_T\left(r,\theta^T,\phi^T\right)=I_0 B_T\left(\theta^T,\phi^T\right)\frac{10^{-\alpha r}}{r^2}, \tag{6.14}$$

where I_0 is the acoustic intensity at the distance $r=1$ on the axis defined by $\phi^T=\gamma=0$, and $B_T(\theta^T,\phi^T)=[H_T(\theta^T,\phi^T)]^2$.

The real directional factor $B_T\left(\theta^T,\phi^T\right)$ will differ from the theoretical directional factor $B_T\left(\gamma\right)$ by much lower side lobe levels, and by the fact that it is dependent on both θ^T and ϕ^T. If the position $\mathbf{X}$ of the fish is known we get θ^T and ϕ^T for the beam number (i,j) by the rotation matrix $\mathbb{A}_{yxy}(-\pi/2,-\alpha_i,\beta_j)$, where α_i and β_j are defined in (3.1), and the notation for the rotation matrix is explained in Appendix A. In this chapter we will concentrate on the theoretical directional factor, as it possesses the same qualities as the real directional factor does. A useful approximation to the directional factor of a circular piston is the parabola shown in Figure 6.7.

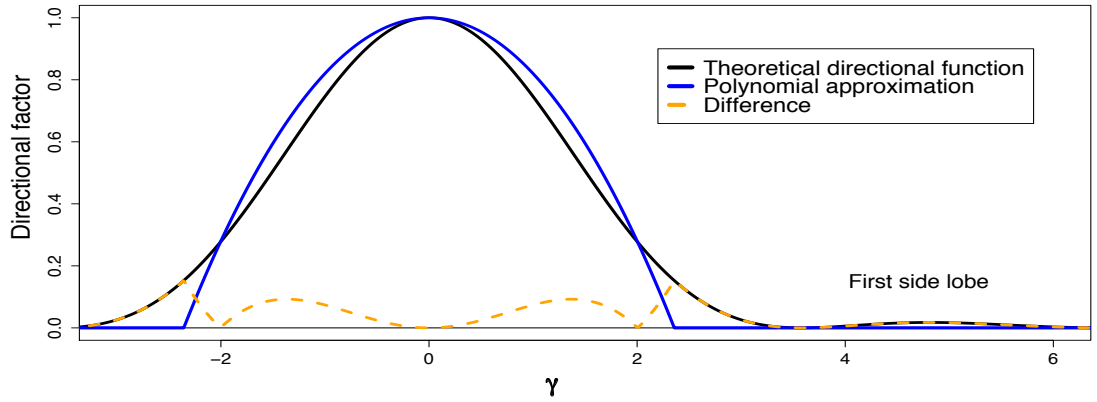

Figure 6.7: The theoretical directional factor of a beam in MS70, together with a polynomial function found to match the Bessel function by visual ispection.

6.1.6 Summary for one fish.

We have now established all relations concerning the acoustic intensity $I_E(S, \mathbf{X}, \Omega)$ of the signal from the fish at the receiver, as functions of the size S, the position $\mathbf{X}$, and the orientation Ω of the fish. From the product of maximum acoustic intensity and directional factor in (2.8), and from (6.9) and (6.14), we have that

$$I_E(S, \mathbf{X}, \Omega) = I_{max}(r)\, B_F\left(\theta', \phi'\right),$$

where

$$I_{max}(r) = \frac{I_T A_0 \eta_c \eta_\Omega}{\psi} \frac{10^{-\alpha r}}{r^2} \quad \text{and} \quad I_T = I_0 B_T\left(\theta^T, \phi^T\right) \frac{10^{-\alpha r}}{r^2}.$$

Combined, these three relations give us the *sonar equation*

$$I_E(r,\theta',\phi') = I_0 \frac{10^{-2\alpha r}}{r^4} B_T\left(\theta^T,\phi^T\right) B_F\left(\theta',\phi'\right) \eta_\Omega \frac{A_0}{\psi} \eta_c, \tag{6.15}$$

where

$$A_0 = \varepsilon S^2,$$

$$\eta_c = \left(\frac{1}{1-0.0995 Z_X}\right)^{\gamma_A},$$

$$\eta_\Omega = \frac{\pi + 2\left(b-2\right)\sqrt{1-\left(\sin\left(\beta^F+\tau\right)\cos\alpha^F\sin\phi\cos\theta + \sin\left(\beta^F+\tau\right)\sin\alpha^F\sin\phi\sin\theta + \cos\left(\beta^F+\tau\right)\cos\phi\right)^2}}{\pi + 2\left(b-2\right)},$$

and

$$\psi = \psi(k,S) = \oint_{r=1} B\left(\theta',\phi',k,S\right) ds.$$

The elements in the sonar equation that are related to the fish, can be regarded as stochastic, even if S, $\mathbf{X}$ and Ω are known exactly. The beam pattern $B_F\left(\theta',\phi',k,S\right)$ from the fish is dependent on the shape, size and tilt of the swim bladder, and physiological configuration of the rest of the fish, which all vary among fishes of similar size and species. The depth dependence of the fish may also involve individual differences, affecting the depth relation to the acoustic cross sectional area given by η_c. The optimal receiving cross sectional area A_0 may vary among fishes of similar size and species, and finally, the response to orientation may involve some noise, mainly due to differences in the tilt angle τ of the swim bladder.

In the following however, we will look at what happens when S, $\mathbf{X}$ and Ω are indeed stochastic variables. The aim is to identify the largest sources of variation from this randomness.

6.2 Randomness in the backscattering from one fish.

In this section we seek to examine the effect of randomness in S, $\mathbf{X}$ and Ω, on the variability of the total signal from one fish. This can later be generalized to more than one fish, and the aim for the discussion is to reveal the randomness in the B-values defined in (2.14), from the MS70 sonar. We consider the different parts of the sonar equation (6.15), and examine the squared coefficient of variation $v^2 = \sigma^2/\mu^2$ related to each part, where σ^2 is the variance and μ is the expected value of each part.

6.2.1 Subvolume for a random fish.

We consider the acoustic intensity received by beam number (i, j), in the kth time interval, which reflect the echo ability of the objects located in voxel number (i, j, k). Voxel number (i, j, k) is spatially defined by the surfaces in (4.1) and in (4.2), but as seen in Figure 4.1 in Chapter 4, the specific beam receives signals from objects located in the radial range $[r_k - \Delta r, r_k + \Delta r]$, which is twice as wide as the radial range of a voxel. The fraction of acoustic energy received in time interval number k, from a small object at the distance r from the transducer, is given by

$$\eta_r = \begin{cases} 1 - |r - r_k| & r \in [r_k - \Delta, r_k + \Delta r] \\ 0, & \text{else} \end{cases}, \tag{6.16}$$

so that $\eta_r \in (0, 1)$. The factor η_r can be added to the sonar equation (6.15).

The strong directivity of the beams of the MS70 sonar allowed us to define the system of voxels in Chapter 4. It will also allow us to limit the volume of interest when talking about the acoustic intensity received in the kth time interval. Even though the real beam pattern is wider horizontally than vertically, we will consider the theoretical directional factor $B_T(\gamma)$, given by (2.8) and (2.9). We approximate the directional factor by a parabola function as shown in Figure 6.7, given by

$$g(\gamma) = \begin{cases} 1 - \epsilon\gamma^2 & \gamma \in \left[0, \epsilon^{-1/2}\right] \\ 0 & \text{else} \end{cases}. \tag{6.17}$$

This expression defines the range of γ of interest, where ϵ must be chosen from some criterion of goodness of fit. As seen in Figure 6.7, this range may not cover the side lobes of the beam, and even not the main lobe entirely. We will bear in mind that there can be fish with γ outside of $[0, \epsilon^{-1/2}]$, contributing to the signal received in time interval k, for beam number (i, j). In Figure 6.7 the Bessel function was found using frequency $f = 75000$Hz, speed of sound in sea water $c = 1500$m/s, and length of the line source $L = 0.195$m,

producing a -3 dB opening angle close to 3°. By visual inspection a was chosen to be 0.18, giving the range $\gamma \in [0, 2.36°]$. We will use these choices when simulating the signal from one fish, later in this chapter.

The subvolume defined by (6.16) and (6.17) is named S_{ijk}. Observe that S_{ijk} is larger than the volume of the corresponding voxel, defined in Chapter 4, leading to a smoothing of the data discussed later in this chapter. Fish outside of S_{ijk}, which are not considered by the parabola approximation, will enhance this smoothing.

6.2.2 Probability distribution of X, S and Ω.

Distribution of X.

If the entire subvolume S_{ijk} is *inside* the school, it will be completely surrounded by fish. In individual based models of fish schools, fish react to the behaviour of neighbouring fish according to certain rules described in Chapter 1. Because there is a limited range of communication between fish, it is common in IBMs to limit the number of neighbours affecting the behaviour of one fish. (Huth and Wissel, 1992) performed simulations of a school of 8 fish, behaving in accordance to an IBM, in addition to some randomness in the movement and orientation of the fish. One result was that the number of fish affecting the behaviour of one fish, had little effect on the structure of the school, once this number exceeded 4. This means that fish *inside* the school pays little attention as to which fish densities that exist beyond the 4 nearest neighbours. According to this it would be a reasonable assumption that fish are distributed quite regularly within S_{ijk}, as long as the subvolume is completely surrounded by fish, so that we can approximate the position of a fish by the uniform distribution.

This assumption will be valid when considering only one of the fish in the subvolume. When there are more than one fish present in S_{ijk}, fish number m will have a smaller and more complex volume to position itself in than the previous fish, since the volume of choice is restricted by the desire to avoid collision with other fish. However, the space occupied by a fish would be small compared to the rest of the subvolume S_{ijk}, unless the school is very dense, so the uniform distribution of the three dimensional position vector $\mathbf{X}$ of a given fish, will be considered generally valid.

If only parts of the subvolume contains the school, the assumption of uniformly distributed position will not be valid. This situation will be quite frequent in the case of the MS70 sonar, and especially for fish schools located far out in the insonified volume. For the parabola approximation used in the previous section, and for the school treated in this thesis, which is located around 300 meters from the sonar, the height and width of the subvolumes will be typically 20 meters. The beam plotted in Figure 6.2, makes the angle 23.68° with horizontal, so that it gradually will intercept the school. For this reason the assumption of uniformly distributed spatial positions of fish will be invalid for parts of the beam. In the discussion of randomness in the signal from one fish we will still assume fish positions to be uniformly distributed, as this simplifies the discussion.

In the sonar equation the variables related to $\mathbf{X}$ are distance the r from the transducer, depth Z_X and angles (θ^T, ϕ^T) of the fish.

Because of the short range in r for S_{ijk} ($2\Delta r \approx 0.78$ meters), and the narrow range of angle γ, we assume r to be uniformly distributed between $r_k - \Delta r/2$ and $r_k + 3\Delta r/2$. The other two variables needs a bit more attention.

If the shape of the subvolume S_{ijk} were an upright cuboid (vertical side walls, and horizontal top and bottom sides), the horizontal cross sectional area would be constant, and the depth Z_X of a fish would clearly be uniformly distributed given that $\mathbf{X}$ is uniformly distributed. However, S_{ijk} is shaped like a cylinder with with slightly curved top and bottom sides, and small height (0.379 meters), as seen in Figure 6.8. The 500 cylinders are tilted by angles found from the unit vectors of the beams, defined in Chapter 3. The probability

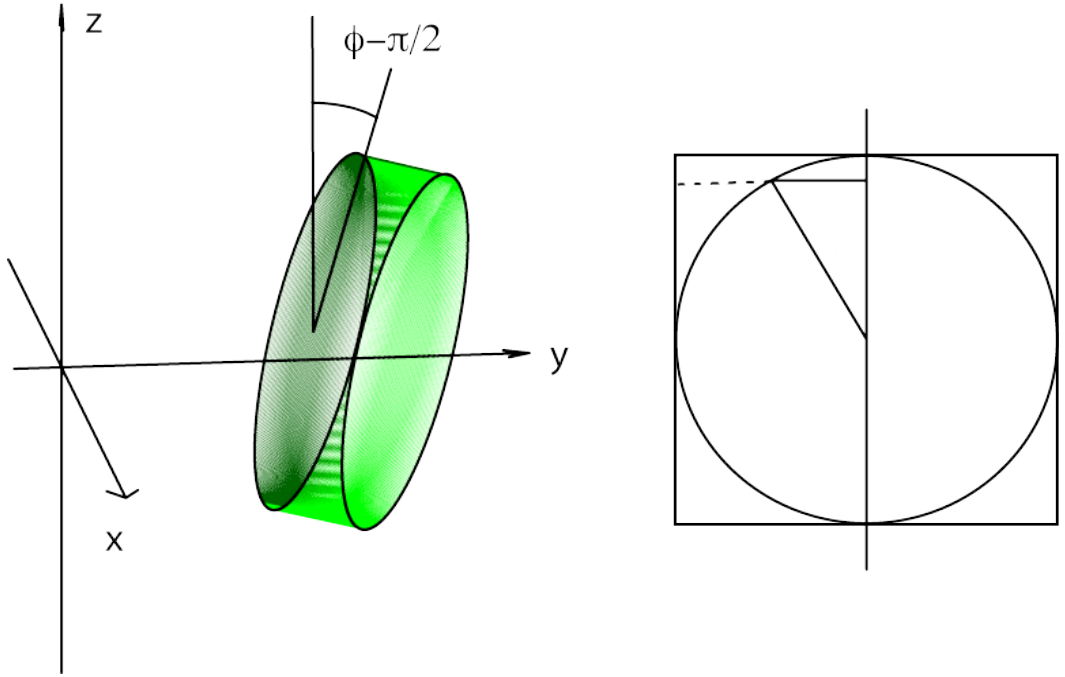

Figure 6.8: The subvolume S_{ijk} as seen from the side (left), and the square approximation to the circle (right).

that $Z_X \leq z$, in the subvolume S_{ijk}, will be the volume of the part of the subvolume corresponding to $Z_X \leq z$, divided by the volume of the entire subvolume. However, we will approximate this distribution with the uniform distribution, corresponding to approximating the circle with the square, as shown in Figure 6.8. The fit is poor for the upper and the lower part of the subvolume, but at these parts

the acoustic intensity from the transducer is at the lowest, so the effect of the mismatch will be small.

To find the probability distribution of the angle γ with the axis of acoustic maximum of the beam, we consider the area of a circle of radius γ, centered at this axis. We define the range of γ as $[0, \gamma_{max}]$, where $\gamma_{max} = \epsilon^{-1/2}$ in case of the parabola approximation. The cumulative probability distribution of γ will then be the area of the circle of radius γ, divided by the area of the circle of radius γ_{max}. Differentiation provides us with the probability density function of γ:

$$F(\gamma) = \frac{\pi\gamma^2}{\pi\gamma_{max}^2} \quad \rightarrow \quad f(\gamma) = \frac{2}{\gamma_{max}^2}\gamma, \quad \gamma \in [0, \gamma_{max}]. \tag{6.18}$$

Distribution of S.

The length S of a schooling fish is usually assumed as being normally distributed. In (Ona, 2003) the empirical mean and standard deviation for the length of herring were found to be 31.8 cm and 1.4 cm, from 28 trawl samples taken in 1997, and 33.2 cm and 2.4 cm, from 19 trawl samples taken in 2000, both in the Vestfjord/Ofotfjord area in northern Norway. A Gaussian distribution with a characteristic mean length for each species, and coefficient of variation $v_S = \sigma_S/\mu_S$ not larger than 0.1, would thus be adequate for the length S of fish in schools. If one only looks at one school, the variance in fish length might be smaller, since fish tend to join schools of fish with similar length, when two schools encounter (Krause et al., 1987).

Asuming that A_0 is at least nearly proportional to S^2, we conclude that A_0 can be described by the non-central chi-square distribution with $k = 1$ degree of freedom and non-centrality parameter $\lambda = \mu_S^2/\sigma_S^2$ not smaller than 100, using the results in (Ona, 2003).

Distribution of $\Omega = (\alpha^F, \beta^F)$.

In an ideal school fish should be highly syncronized, so that the variance in the orientation distribution is small. In large schools, (as the school discussed in this thesis which spans more than 100 meters), the orientation of a fish at one end is unlikely to directly affect the orientation of the fish at the other end very much. There is a range in which the fish are able to see each other, or feel the movement of neighbouring fish with the lateral line (motion sense organ along the side of the fish). If the school moves, there must clearly be more fish with orientation in the direction of the school, than in other directions, but polarization might not be very high. A natural assumption would be the normal distribution for the orientation angle α^F, with mean in the direction of the fish, and variance reflecting the polarization. The vertical orientation angle β^F will also be assumed gaussian, but with smaller variance than α.

6.2.3 Randomness in the sonar equation.

We now wish to translate the randomness in $\mathbf{X}$, A_0 and Ω into randomness in the acoustic intensity from one single fish, which is given by the sonar equation. Generalization of the results in this section to the signal from more than one fish, will be done in the following

sections. The effect of the stochastic variables r, Z_X, γ, A_0 and Ω, will be treated one by one, and we restate (6.15) for practical reasons as

$$\begin{aligned} I_E(r,\theta',\phi') &= I_0 \frac{10^{-2\alpha r}}{r^4} B_T\left(\theta^T,\phi^T\right) B_F\left(\theta',\phi'\right) \eta_\Omega \frac{A_0}{\psi}\, \eta_c\, \eta_r \\ &= \quad \text{(A)} \qquad \text{(B)} \qquad \text{(C)} \qquad \text{(D)(E)(F)}, \end{aligned} \tag{6.19}$$

where we have added the radial weighting given in (6.16).

To measure the variability in the 6 different parts of (6.19), we consider the squared coefficient of variation $v^2 = \sigma^2/\mu^2$, where σ^2 is the variance, and μ is the expected value of an arbitrary stochastic variable. We will explain the use of v^2 by computing $v^2 = v_{XY}^2$ for the product of two independent variables X and Y:

$$\begin{aligned} \mathrm{Var}(XY) &= \int_x \int_y x^2 y^2 f(x) f(y) dy dx - \int_x \int_y xy f(x) f(y) dy dx \\ &= \int_x x^2 f(x) dx \int_y y^2 f(y) dy - \int_x x f(x) dx \int_y y f(y) dy \\ &= \left(\sigma_X^2 + \mu_X^2\right)\left(\sigma_Y^2 + \mu_Y^2\right) - \mu_X^2 \mu_Y^2 = \sigma_X^2\sigma_Y^2 + \sigma_X^2\mu_Y^2 + \sigma_Y^2\mu_X^2. \end{aligned} \tag{6.20}$$

Expressed in terms of v^2, (6.20) becomes

$$v_{XY}^2 = \frac{\mathrm{Var}(XY)}{\mathrm{E}(XY)^2} = \frac{\sigma_X^2\sigma_Y^2}{\mu_X^2\mu_Y^2} + \frac{\sigma_X^2}{\mu_X^2} + \frac{\sigma_Y^2}{\mu_Y^2} = v_X^2 v_Y^2 + v_X^2 + v_Y^2. \tag{6.21}$$

In the case of 6 independent variables we would have one part containing all 6 ratios, 6 parts containing 5 ratios, and so on, where the number of parts are taken from the 7'th line in Pascal's Triangle of numbers, which is 1 6 15 20 15 6 1. We see this from the last line in (6.20), generalized to the 6 variables (A), (B), (C), (D), (E) and (F) inn (6.19):

$$\mathrm{Var}\left((A)\,(B)\,(C)\,(D)\,(E)\,(F)\right) = \left(\sigma_A^2+\mu_A^2\right)\left(\sigma_B^2+\mu_B^2\right)\left(\sigma_C^2+\mu_C^2\right)\left(\sigma_D^2+\mu_D^2\right)\left(\sigma_E^2+\mu_E^2\right)\left(\sigma_F^2+\mu_F^2\right) - \left(\mu_A\,\mu_B\,\mu_C\,\mu_D\,\mu_E\,\mu_F\right)^2 .$$

Dividing the variance of the product of the 6 variables expressed above, by the product of the mean of the 6 individual variables, we get the total squared coefficient of variation named $v_{A:F}^2$. We now wish that the individual squared coefficients of variation $v_A^2,\ldots,v_F^2$ are smaller than one, and small enough that most of the products of two or more squared coefficients of variation can be neglected in the total $v_{A:F}^2$

In the following we analyze the squared coefficient of variation for the 6 variables (A) through (F) separately. The final calculation of $v_{A:F}^2$ requires independency between the 6 parts of (6.19), which to a large extent is true. A discussion of independency is done at the end of this section.

(A).

Because of the short range $[r_k-\Delta r,r_k+\Delta r]$ compared to r_k, variation in the backscattering from one fish in S_{ijk} due to absorption and geometric attenuation is negligible. A computer simulation of 10000 fish with uniformly distributed distances to the transducer in the given range, resulted in $v_A^2 \approx 7.9\cdot 10^{-5}$.

(B).

In (6.18) we presented the probability distribution of the angle γ between the axis of acoustic maximum of a beam, and the position vector of a uniformly positioned fish. Since the acoustic intensity of the sound from a particular beam, is dependent on γ through the beam pattern $B_T(\gamma)$, we wish to transform from the distribution of the random variable γ to the distribution of $B_T(\gamma)$. To ease notation we write $B=B_T(\gamma)$ with the realization b. We use the parabola approximation for the beam pattern of the transducer given in (6.17), which defines the range of interest of γ to $\gamma\in[0,\epsilon^{1/2}]$:

$$f_\Gamma(\gamma) = \frac{2}{\gamma_{max}}\gamma = 2\epsilon\gamma \qquad \text{and} \qquad b = 1 - \epsilon\gamma^2$$

$$\Downarrow$$

$$\gamma(b) = \left(\frac{1-b}{\epsilon}\right)^{1/2}$$

$$\Downarrow$$

$$|J| = \frac{1}{2\epsilon}\left(\frac{1-b}{\epsilon}\right)^{-1/2}$$

which gives the transformation from γ to B:

$$f_B(b) = f_\Gamma\left(\gamma(b)\right) \cdot |J| = 2\epsilon\left(\frac{1-b}{\epsilon}\right)^{1/2} \cdot \frac{1}{2\epsilon}\left(\frac{1-b}{\epsilon}\right)^{-1/2} = 1$$

$$\Longrightarrow \qquad B_T(\gamma) \sim \text{Uniform}(0,1).$$

The variance and expectation of uniformly distributed variables then gives us $v_B^2 = \frac{1}{12} \cdot 0.5^2 = \frac{1}{3}$.

Since the parabola approximation is zero at the side lobes and at the weak parts of the main lobe, it neglects fish which experience weak intensity from the beam, thus overestimating the expectation μ_B. This may lead to a too low v_B^2. Still, we can defend the approximation by the fact that it neglects only weak signals, which when summing up all fish in S_{ijk}, will have little contribution to the total signal.

(C).

The beam pattern of the pressure field from a fish has a great influence on the acoustic intensity scattered towards the receiver. This beam pattern is the product of the directional factor of the fish, and the cross sectional area of the swim bladder/imaginary swim bladder, as seen from the transducer, called *aspect factor*. The directional factor of the fish is dependent on the product of wave number k and length l of the swim bladder/imaginary swim bladder (as seen (6.4) for the directional factor of the line source). Since frequencies vary between horizontal fans in the MS70 sonar, the directional factor for all fish changes accordingly. The length L is dependent on

size S of the fish so we need to add the dependency of S to the directional factor of the fish as done in (6.5) and (6.6).

The angles θ' and ϕ' were found in (6.2), and depends on the five angles θ_T, ϕ_T (angles in the coordinate system of the transducer as defined in section 6.1.5), α^F, β^F (orientation of the fish) and τ (tilt angle of the swim bladder), which all can be considered stochastic. Variance of θ_T and ϕ_T is small, since the width of the subvolume S_{ijk} as seen from the transducer is narrow. The subvolume chosen by the parabola approximation of $B_T(\theta, \phi)$ is defined by $\gamma_{max} = a^{-1/2} = 2.36°$, so the width of S_{ijk} is clearly narrow and we thus neglect the randomness of θ and ϕ. Variations in τ can be incorporated in the orientation angle β^F, giving this a larger variance. We thus end up with 3 stochastic variables affecting the beam pattern of the pressure field from the a fish: α^F, β^F and S.

There is an important difference in how orientation angles α^F and β^F affect the acoustic intensity at the receiver, and the effect of S. While size influence the beam pattern of the fish, α^F and β^F *decide* the direction. As we have established that the variance in S is not very large (coefficient of variation ≈ 0.05), we only consider the effect of α^F and β^F on the randomness of the beam pattern. To model the product $B_F\left(\theta', \phi'\right)\eta_\Omega$, we consider the theoretical directional factor of a line source, given in (6.4). We wish to smoothen the directional factor $B_F\left(\gamma'\right)$, by taking the mean of $B_F\left(\gamma'\right)$ from a number of fish of random Gaussian length, giving $\bar{B}_F\left(\gamma'\right)$. The purpose of this smoothing is that directional factors found in research papers involve smoothing of this kind. An important documentation on the directional factor of fish is (Love, 1977), where fish of 12 different species and lengths in the range (0.015,1) meters, with or without swim bladder, were insonified with sound frequencies in the range (0.015,1.5) MHz. Target strengths were measured for a set of transducer/receiver aspects, and the data were analyzed by the least squares method, performed on a logarithmic version of an empirically found relation in (Love, 1969):

$$\frac{\sigma_{sp}}{\lambda^2} = a\left(\frac{L}{\lambda}\right)^b, \tag{6.22}$$

where λ is the wavelength of the sound, and a and b are regression coefficients. These regression coefficients are not the same as the radius a of the line source and the ratio $b = L/a$ of swim bladder length and swim bladder radius, used in section 6.1.4.

We consider the case $\phi' = 90°$, which corresponds to seven of the aspects at which the fish are viewed in (Love, 1977), specified by $\phi' \in (75°, 105°)$, and $\theta \in \{(-105°, -75°), (-75°, -45°), \ldots, (75°, 105°)\}$. We do the smoothing for three different mean lengths of the line sources, 0.005 m, 0.015 m and 0.05 m, and coefficient of variation $\sigma/\mu = 1/5$. Figure 6.9 shows the smoothed directional factors $\bar{B}_F\left(\gamma'\right)$, aspect factors η_Ω, and the product of these (beam pattern), for swim bladder models produced by averaging 50 directional factors from line sources of lengths from the Gaussian distribution given above. Estimated regression parameters a from (6.22), for the seven aspects mentioned above and scaled so that $max(a) = 1$, are plotted in black dashed lines.

The figure displays the great effect of changes in length μ_L on the smoothed directional factor $\bar{B}_F\left(\gamma'\right)$. By visual inspection, it seems

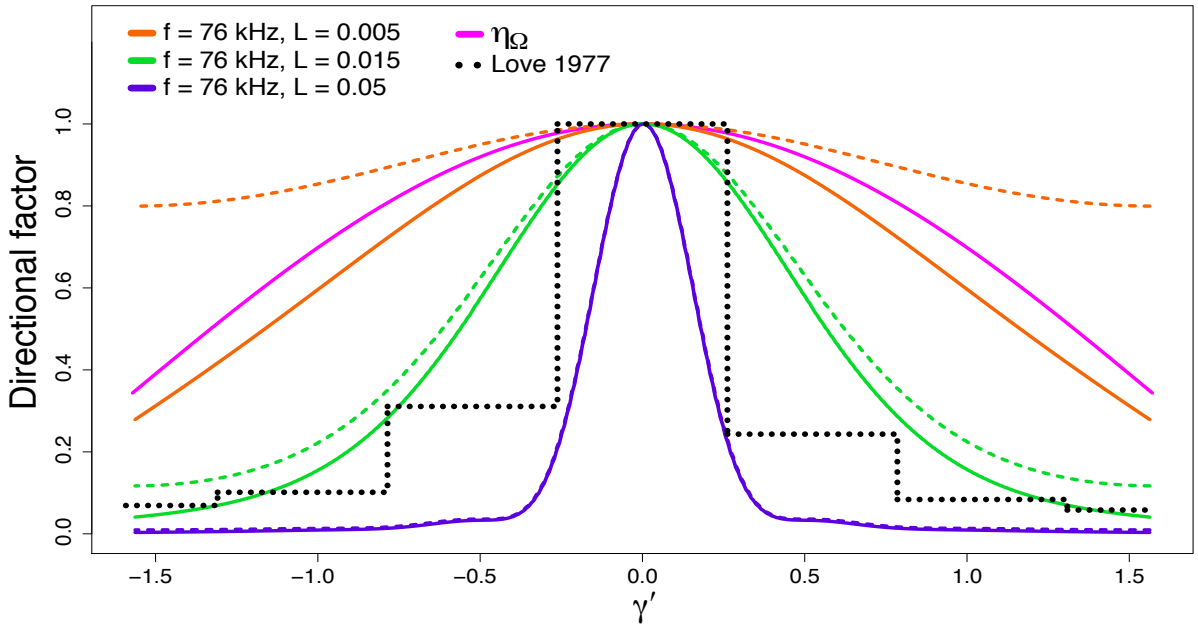

Figure 6.9: Theoretically estimated $B_F\left(\gamma'\right)$ (beam pattern), η_Ω (aspect factor) and the product of these two (directional factor), for fish with swim bladders, plotted against angle of incidence γ' to the line source representing the swim bladder. The beam patterns were produced by averaging the beam pattern from 50 line sources of Gaussian length with means $\mu = 0.005$ m, $\mu = 0.015$ m and $\mu = 0.05$ m, and with coefficient of variation $\sigma/\mu = 1/5$, representing three species of different lengths. Frequency of the sound is set to $f = 76$ kHz. The pink line is the aspect factor η_Ω for the cross sectional area of the cylinder representing the swim bladder. The dashed lines are $B_F\left(\gamma'\right)$, while solid lines are the product of η_Ω and $B_F\left(\gamma'\right)$. The fish model is seen from the side, so $\phi' = \pi/2$. Results from (Love, 1977) are plotted in black for comparision.

reasonable that mean length of the line sources producing the smoothed beam pattern $\bar{B}_F\left(\gamma'\right)$ should be between 0.015 m and 0.05 m. This is of course a very inaccurate estimate, but considering the high sensitivity of $\bar{B}_F\left(\gamma'\right)$ regarding the product kL, and the fact that the directional factor is found from theoretical line sources, a narrower specification might be unwise. In (Gorska and Ona, 2003b) a picture of a 32 cm herring is shown, and the swim bladder length is found to be 83 mm. However, the thickness of the swim bladder varies, and if we only consider the thick part, this makes up less than half of the swim bladder length. A line source approximation of length $L > 50$ mm thus seems unwise, while $L < 15$ mm is probably to short, so $\mu_L \in (0.015, 0.05)$ m appears to be a safe estimate. This is of course based on an assumption that the school in question is of herring. Other fish with shorter or longer swim bladders, will have directional factor changed accordingly.

We examined the effect on v_C^2 of the mean μ_L of the 50 objects drawn to produce the smoothed directional factor $\bar{B}_F\left(\gamma'\right)$, and of the ratio b used in η_Ω (6.13). All 6 combinations of $b = (5, 10)$ and $\mu_L = (0.005, 0.015, 0.05)$, were used to generate 6 numeric functions $\bar{B}_F\left(\gamma'\right)\eta_\Omega$, which were applied to 1000 "fish" with randomly chosen orientations (α^F, β^F). The angles α^F were drawn from the uniform distribution between 0 and 2π, while β^F was set to $\pi/2$. This process was repeated 10 times, with a new set of orientations each time. The results of the simulations are shown in Figure 6.10. The lines have colours orange, green and blue for $\mu_L = 0.005, 0.015$ and 0.05 respectively. We see that the greatest effect on v_C^2 is from differences in mean length μ_L, of the 50 "fish" drawn to produce the smoothed directional factor $\bar{B}_F\left(\gamma'\right)$. This represents the size of the fish, and affects kL in the same way as the frequency does. The larger fish, the more polarized directional factor. The ratio b seems to have a limited effect on the smoothed directional factor. Since the frequency is $f = 76$ kHz in the top fan and $f = 111$ kHz in the bottom fan, v_C^2 changes accordingly, giving larger coefficient of variance in the bottom fan.

From the specification that $\mu_L \in (0.015, 0.05)$, Figure 6.10 gives us a squared coefficient of variation approximately $v_C^2 \in (0.5, 7)$.

(D).

The optimal receiving cross sectional area A_0, was found in section 6.2.2 to be nearly non-central chi-square distributed with $k = 1$ degree of freedom and non-centrality parameter $\lambda = \mu_S^2/\sigma_S^2 > 100$. The mean and variance of a non-central chi-square distributed variable are $k + \lambda$ and $2(k + 2\lambda)$, so for a large λ, v_D^2 will we approximately $4/\lambda < 0.04$.

(E).

The variance contribution from depth compression of the swim bladder, is highly dependent on the distance r from the transducer. We consider the subvolume $S_{13,20,1319}$, which has the widest range of Z_X-values. (This subvolume may be partially above the surface of the sea, depending on how deep the sonar is lowered.) Computer simulations of 10000 fish with swim bladders having $\gamma_A = 2/3$, with Z_X drawn from the uniform distribution between 0 and $1319\Delta r \sin(2\gamma_{max}) \approx 41$ meters, resulted in $v_E^2 \approx 0.1$. Compared to the estimated γ_A in (Ona, 2003), the assumption that $\gamma_A = 2/3$ involves no risk of underestimating v_E^2.

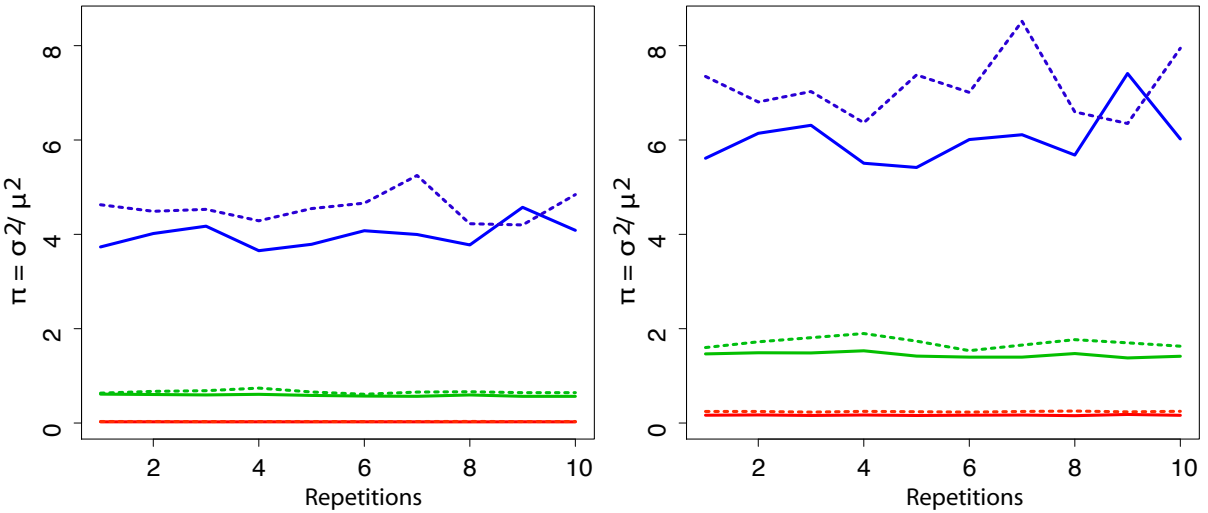

Figure 6.10: Estimated squared coefficient of variation v_C^2 for the product of smoothed directional factor and cross sectional area, $\bar{B}_F\left(\gamma'\right)\eta_\Omega$, of (imaginary) swim bladders. 1000 fish were drawn for each of the 10 repetitions, with orientation angles $\alpha^F \sim \text{Uniform}(0, 2\pi)$, and $\beta^F = \pi/2$. The orange, green and blue lines represent fish with swim bladder lengths 0.005, 0.015 and 0.05 meters respectively, as in Figure 6.9. Dashed and solid lines are for $b = 5$ and $b = 10$ respectively. The plot to the left is of fish insonified by a beam in the bottom horizontal fan (S_{ijk} $j = 1$, and $f = 111$ kHz), while the left plot is of fish in the top horizontal fan (S_{ijk} $j = 20$, and $f = 76$ kHz).

(F).

As stated before, r can be considered uniformly distributed in the range of the subvolume S_{ijk}. Transformation from r to η_r leads immediately to $\eta_r \sim \text{Uniform}(0,1)$, so as for $B_T(\gamma)$ we get $v_F^2 = \frac{1}{3}$.

Overall variance.

We sum up the previous discussions by a table of squared coefficients of variation:

$I_0 \frac{10^{-2\alpha r}}{r^4}$	$B_T\left(\theta^T, \phi^T\right)$	$B_F\left(\theta', \phi'\right)\eta_\Omega$	$\frac{1}{4\pi}A_0$	η_c	η_r
$v_A^2 \approx 7.9 \cdot 10^{-5}$	$v_B^2 = \frac{1}{3}$	$v_C^2 \in (0.5, 7)$	$v_D^2 < 0.04$	$v_E^2 \approx 0.1$	$v_F^2 = \frac{1}{3}$

The largest source of variation in the signal from a single fish is clearly the beam pattern of the fish. TFrom the discussion around (6.21) we get that the largest contributions to $v_{A:F}^2$ are

$$v_{A:F}^2 \approx v_B^2 + v_C^2 + v_E^2 + v_F^2 + v_C^2(v_B^2 + v_E^2 + v_F^2) \in (1.65, 13.1). \tag{6.23}$$

This way to calculate the variability in the sonar equation assumes independency between the 6 elements, which is nearly true. Part (A) and (F) are dependent, but (A) contributes so little to the total variation, that we neglect this dependency. (C) depends on both size affecting (D) and depth affecting (E), but given the large uncertainty in the randomness in (C) we du not bother to investigate this dependency. Hence we stick with the independency assumption.

The nature of the variability in the sonar equation is mainly resulting from the nature of the variability in the directional factor of the fish. The distribution will thus be high for low values of the acoustic intensity, and lower for larger values, since the beam pattern $\bar{B}_F\left(\gamma'\right)\eta_\Omega$ is low for most directions and high for angles near optimal incidence.

Remark about the expected backscattering from one fish.

A fundamental difference between echo sounders radiating vertically, and the MS70 sonar radiating at angles with horizontal in the range $(0°, 45°)$, is that a fish of uniformly distributed orientation angle α^F will have larger mean directional factor in the direction of

the transducer for echo sounders than for the MS70 sonar. This is because the angle of incidence of the transducer/receiver of an echo sounder, respective to the fish, will have mean 0. If we consider two fish of the same species, but with different lengths S, the beam pattern of the large fish will be more polarized than the beam pattern of the small fish. This will result in a smaller surface integrated beam factor $\psi(k, S)$ for the large fish than for the small fish. Referring to (6.10) this results in a larger optimal backscattering σ_0 from the large fish, than would be expected only from the enhanced size of the fish. However, averaging the beam factor over uniformly distributed orientation angles α^F, will be close to integrating the beam factor over all directions, which is what we do to obtain $\psi(k, S)$. Thus the larger fish will have mean spherical backscattering cross section $\bar{\sigma}_{sp}$ nearly proportional to fish length, for fish with uniformly distributed α^F. We will use this when analyzing the total backscattering from the school in section 7.2.1. For echo sounders this approximation might not be valid.

6.3 Backscattering from more than one fish.

We will now use the results from the previous section, where we estimated the squared coefficient of variation for one single fish in the subvolume S_{ijk}, as a basis when discussing the randomness in the total signal from an arbitrary number n of fish in the subvolume. This will be a discussion of the randomness in the actual values from a school observed by the MS70 sonar. Through simulations we will estimate the squared coefficient of variation of the values from the sonar, for different numbers of fish in the subvolumes, for different fish lengths, and for different orientation distributions of the fish. Later we will also estimate the autocorrelation between voxels along beams, caused by the radial overlap described in section 4.1.1.

The generalization from one fish to more than one fish involves interference effects between the acoustic signals, resulting in either a weakening or a strengthening of the signal received in time interval k, for beam number (i, j). We will discuss these effects based on the findings in (Stanton, 1984). The interference effects between the fish in the subvolume S_{ijk}, will be shown to dominate the randomness in the total signal from S_{ijk}.

6.3.1 Model for superimposed backscattering from n fish.

The basic assumption when examining interference between fish in a subvolume S_{ijk}, is that the phases of acoustic pressure (the sound) from the fish, are uniformly distributed between 0 and 2π. This is satisfied by the short wavelength of the insonified sound, ranging from 1.3 cm to 2.1 cm, for frequencies from 112000 Hz to 70000 Hz, and speed of sound $c = 1481$ m/s. Even with an extremely rigid structure of the school, individual fluctuations in position would result in uniform phase. When many sine waves having uniform phase and random amplitude are superimposed, the total wave has Rayleigh distributed pressure amplitude (Stanton, 1984):

$$f_X(x) = \frac{x}{\sigma^2} e^{-x^2/2\sigma^2}, \qquad \sigma^2 = \sum_{l=1}^{n} A_l^2/2. \tag{6.24}$$

Here X is the amplitude of the total signal, A_l is the amplitude of the l'th fish, and n is the number of fish in the subvolume S_{ijk}. As the sonar equation (6.15) considers acoustic intensity, we need to look at the squared amplitude. A known result is that if $X \sim \text{Rayleigh}(\sigma^2)$, then the variable $Y = X^2/2\sigma^2\lambda_Y$ has the exponential distribution with parameter λ_Y:

$$\begin{aligned} f_Y(y) &= f_X(h(y))\,|J| \\ &= \frac{\sqrt{2\sigma^2\lambda_Y y}}{\sigma^2}\exp\left[\frac{-2\sigma^2\lambda_Y y}{2\sigma^2}\right]\cdot\frac{\sigma^2\lambda_Y}{\sqrt{2\sigma^2\lambda_Y y}} = \lambda_Y e^{-\lambda_Y y} \end{aligned} \qquad \begin{aligned} h(y) &= \sqrt{2\sigma^2\lambda_Y y} \\ &\Downarrow \\ |J| &= \left|\frac{\sigma^2\lambda_Y}{\sqrt{2\sigma^2\lambda_Y y}}\right|. \end{aligned}$$

We have here that X represents the acoustic pressure amplitude, and Y represents the acoustic intensity. If we now compare $Y = X^2/2\sigma^2\lambda_Y$ with the expression $I = A^2/2\rho_0 c$ for acoustic intensity, presented in (2.6) and with (6.24), we need to have

$$\sigma^2\lambda_Y = \rho_0 c$$

$$\lambda_Y = \frac{2\rho_0 c}{\sum_{l=1}^{n} A_l^2},$$

which leads us to

$$\text{E}Y = \frac{1}{\lambda_Y} = \sum_{l=1}^{n}\frac{A_l^2}{2\rho_0 c} = \sum_{l=1}^{n} I_l.$$

The total acoustic intensity is thus exponentially distributed, with expected value λ_Y equal to the sum of the individual acoustic intensities. The squared coefficient of variation of an exponentially distributed variable is $\sigma^2/\mu^2 = 1$, which will be used when discussing simulations in the nest section. Figure 6.11 shows the sum of 10 sine waves with amplitude 1, giving the expected total intensity 10.

The sum of the individual acoustic intensities $\lambda_Y = \sum_{l=1}^{n} I_l$ is itself stochastic, with squared coefficient of variation $v_{A:F}^2/n$, since the

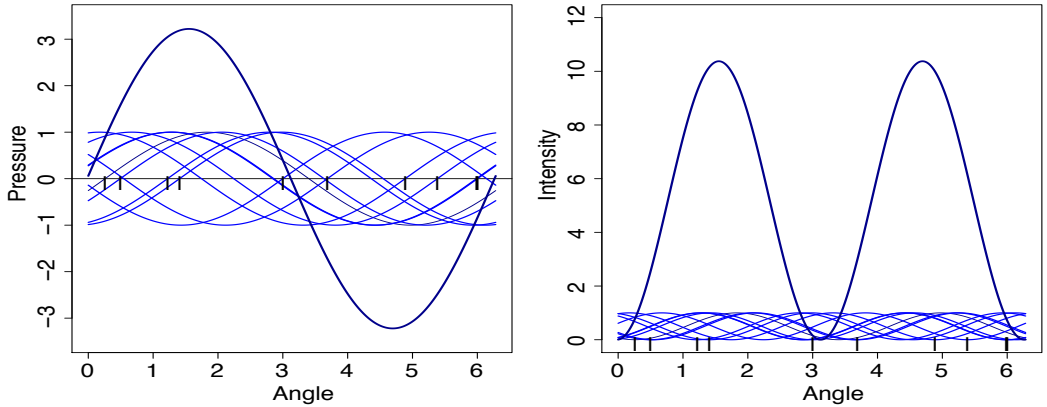

Figure 6.11: The sum of ten sine waves having uniform phase but common amplitude equal to 1. The plot to the right shows the squared sine waves, and the squared total sine wave.

individual acoustic intensities are stochastic. As mentioned at the end of section 6.2.3, the probability distribution of the acoustic intensity from individual fish, will be large for small values of I_l and small for large values of I_l. Using the central limit theorem, the sum of individual acoustic intensities approaches the Gaussian distribution as the number n of fish contributing to a B-value rises. We thus have the hierarchical model of the total intensity Y:

$$Y|\lambda_Y \sim \exp(\lambda_Y) \qquad \frac{1}{\lambda_Y} = \sum_{l=1}^{n} I_l \xrightarrow{n} \text{Gaussian.}$$

6.3.2 Simulations of the backscattering from n fish.

Based on the discussion of randomness in the signal from one fish and the effect of interference between fish, done in the previous section, we wish to performe simulations of the total intensity from n fish in the specific subvolume $S_{13,12,500}$. The aim is to specify the randomness in the B-values, given the number of fish in the subvolumes. We base the simulations on the following variables:

$r \sim \text{unif}(r_k - \Delta r, r_k + \Delta r)$	Distance from the transducer.
γ from (6.18)	Angle with acoustic maximum of the beam.
$\theta^T \sim \text{unif}(0, 2\pi)$	Angle in the plane parallel to acoustic maximum of the beam.
Z_X from $\mathbf{X}= (r, \gamma, \theta^T)$	Depth.
$L = \mu_L$	Length of the swim bladder.
$\sigma_0 \propto L^2$	Optimal scattering cross section.
$\alpha^F \sim N(\mu_{\alpha^F}, \sigma^2_{\alpha^F})$	Orientation angle.
$\beta^F \sim N(\pi/2, (\pi/12)^2)$	Orientation angle.
$\tau = 0$	Tilt angle.
γ' from α^F, β^F and τ, according to (6.3)	Angle of incidence to swim bladder.

We draw values from the specified distributions of these variables, and apply the values to the sonar equation (6.15), in order to produce the amplitude of the "fish". Phases are drawn from the uniform distribution between 0 and 2π, so that interference between fish would be expected. The theoretical directional factor of the transducer given in (2.9) will be used. As the beam pattern of the fish, we use the line source model described in the previous section and displayed in Figure 6.9, where 50 line sources of length $L \sim \text{N}(\mu_L, \sigma_L)$ were averaged to produce the desired directional factor $\bar{B}(\gamma')$. For every simulated fish, we generate a new $\bar{B}(\gamma')$. The maximum beam width γ_{max} is chosen to be 3.5°, in order to to cover the first side lobe of the theoretical beam pattern of the transducer.

Simulations of 1000 intensities from subvolume number $(13, 12, 500)$ will be done, using the three different numbers of fish 1, 30 and 120. We repeat the simulations 6 times, for the different fish lengths and orientation angles:

	μ_L	σ_L	μ_{α^F}	σ_{α^F}
(a)	0.015	0.003	$\pi/2$	$\pi/12$
(b)	0.015	0.003	$\pi/3$	$\pi/12$
(c)	0.015	0.003	$\pi/2$	π
(d)	0.05	0.01	$\pi/2$	$\pi/12$
(e)	0.05	0.01	$\pi/3$	$\pi/12$
(f)	0.05	0.01	$\pi/2$	π

The two mean swim bladder lengths $\mu_L = 0.015$ and $\mu_L = 0.05$ in the line source model of the swim bladder, are the same lengths we used for estimating the total squared coefficient of variation in (6.23). Comparison with the swim bladder of herring studied in (Gorska and Ona, 2003b) also indicated that a line source of length between these two values might be suitable. In the cases (c) and (f), we use Gaussian orientation angles α^F with standard deviation $\sigma_{\alpha^F} = \pi$ to represent no polarization of the simulated school. This will almost correspond to the uniform distribution for α^F used in the derivation of expression (6.23). The reason for the use of Gaussian α^F instead of uniformly distributed α^F, in the cases (c) and (f), is to make these cases consistent with (a), (b), (d) and (e).

The resulting histograms of simulated acoustic intensities are plotted in Figure 6.12 and Figure 6.13, along with the exponential density function with mean equal to the average of the acoustic intensities. We see clearly that the histograms for the number of fish $n = 1$, are too extreme to be explained by the exponential distribution. At $n = 30$ the fit is much nicer, but we can still see some exaggeration of the lower values compared to the moderate values, in the cases (e) and (f). This is also reflected by the high squared coefficient of variation for one fish in the cases (e) and (f), affecting the total signal when there are only 30 fish in the subvolume, so that the squared coefficients of variation is equal to 1.621 and 1.895 respectively when $n = 30$. When fish number is 120 however, there is no apparent deviation from the exponential distribution in any of the cases (a) through (f).

Since the volumes of the subvolumes increase with increasing k (radial number), the density of fish when the number of fish in the subvolume is for instance 30, is dependent on k. These volumes will be approximately $\pi(k\Delta r \sin(3.5^\circ))^2 \cdot 2\Delta r$. For the school treated in this thesis, the minimum value of k is 527, which gives the volume ≈ 350 m^3. If the number of fish in this volume is 30, the fish have more than 10 cubic meters each, which conflicts with the rules of attraction given in IBMs (confront Chapter 1). We thus conclude that the randomness in the signal from individual fish does not affect the B-values in the real data from this school, but that the interference between the individual signals causes the B-values to be exponentially distributed.

However, for a school located 50 meters from the sonar, the size of a subvolume will be approximately 20 m^3, giving a fish density of 1.5 fish per m^3 when $n = 30$, which is more realistic. In future multibeam sonars the beamwidth might be narrower, so that the randomness in the B-values is significantly affected by the randomness in the acoustic intensity from one fish.

Remark about the calibration of the beams.

Because of the angular overlap between beams from the sonar, the neighouring beams of beam number (i, j) contribute to the amount of acoustic energy experienced by a fish in this beam. The beam width was given to be in the range $(6.111902^\circ, 6.962585^\circ)$ horizontally and in the range $(2.602462^\circ, 4.395848^\circ)$ vertically, depending on the position of the beam in the sonar. The corresponding angles for the beams of voxels are $\Delta\alpha = 2.5^\circ$ and $\Delta\beta = 2.37^\circ$ respectively. At the edges of the sonar volume, a fish would thus experience lower acoustic intensity than in the middle of the sonar volume. This needs to be taken into account when calibrating the MS70 sonar.

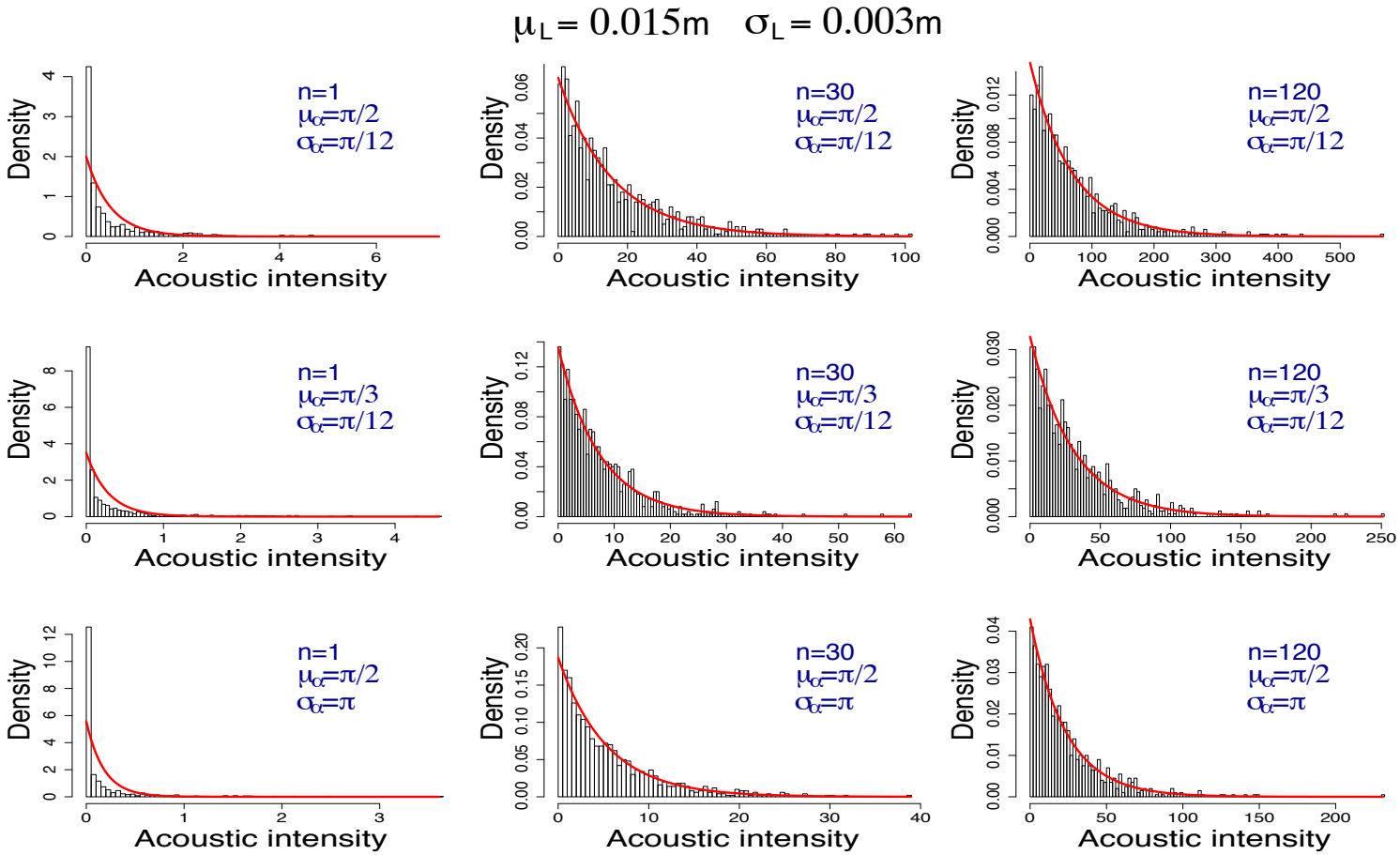

Figure 6.12: Histograms of the simulated acoustic intensity from $n = 1, 30, 120$ fish. Length of swim bladder is set to 0.015 meters.

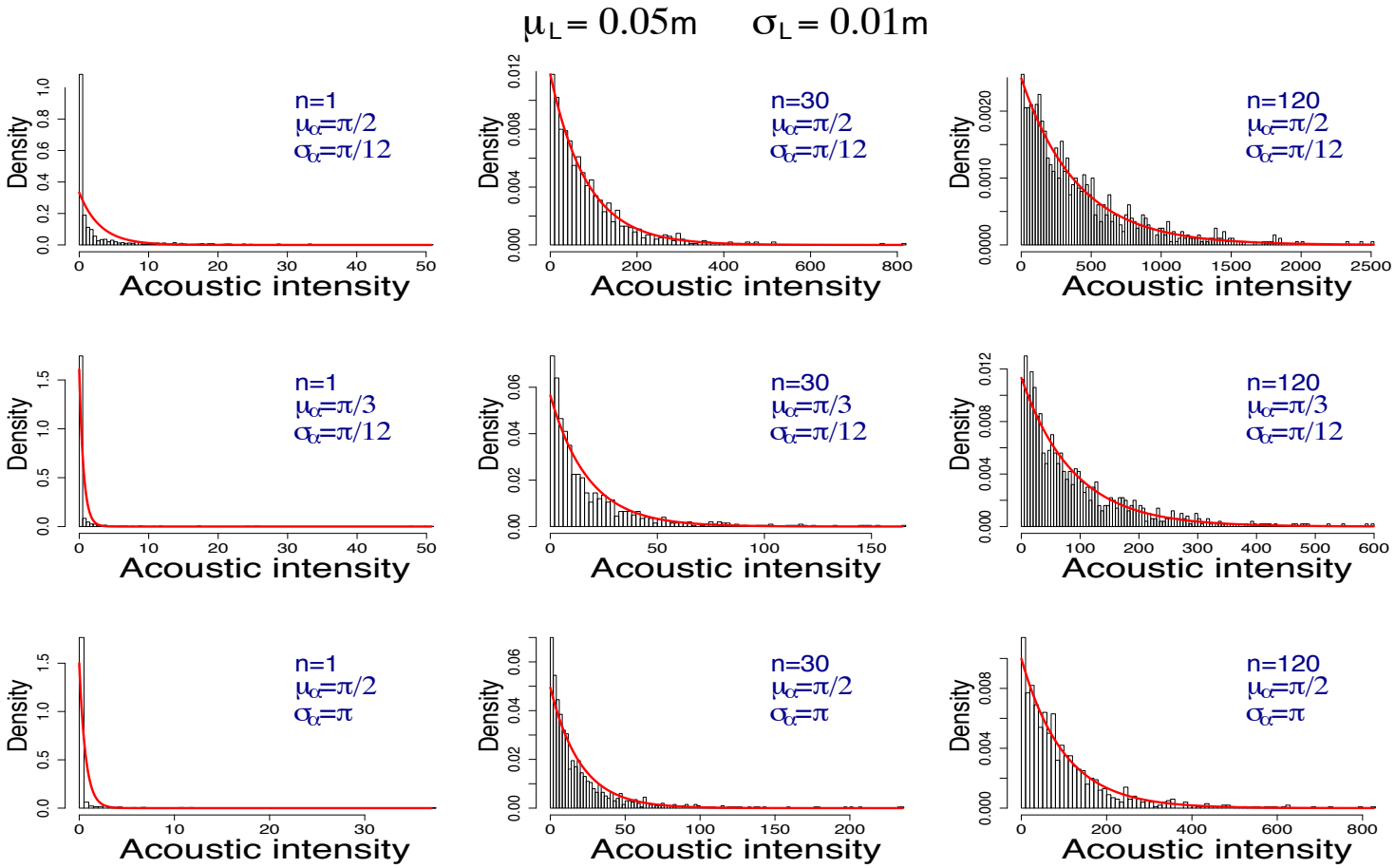

Figure 6.13: Histograms of the simulated acoustic intensity from $n = 1, 30, 120$ fish. Length of swim bladder is set to 0.05 meters.

	Number of fish		
	1	30	120
(a)	2.868	0.996	1.010
(b)	3.726	1.009	0.969
(c)	5.295	1.089	1.035
(d)	4.817	1.112	0.954
(e)	28.860	1.621	1.083
(f)	19.209	1.895	1.212

Table 6.1: Squared coefficient of variation of simulated acoustic intensities.

6.3.3 Simulations of the correlation between voxels along beams.

As presented in section 4.1.1, there is an overlap between voxels along bemas in the MS70 sonar, due to the radial partitioning. To quantify the effect of this overlap on the autocorrelation between voxels along beams, we performed simulations of 1000 beams of 100 voxels, taking radial overlap into account:

As opposed to the previous simulations, we now only drew the radial positions of fish, and assigned the same acoustic intensity to all fish, except for the radial weighting η_r given in (6.16). We thus considered fish positioned on the axis of acoustic maximum of a beam, and gave the fish equal sizes, depths and orientations. Fish positions were drawn from the uniform distribution in 102 voxels, with 100 fish in each voxel. The reason for drawing fish positions in 102 voxels, is that the intensity assigned to a voxel comes from fish in the respective voxel, and from fish in the two neighbouring voxels, as seen in Figure 4.1. The B-values for the center 100 voxels were thus calculated. Phases of the fish were drawn from the uniform distribution between 0 and 2π.

For each of the 100 voxels in a beam, we summed up all sine waves from the fish contributing to the respective B-values, using (6.16). The resulting amplitudes were then squared to give values of the intensity. The autocorrelations of lags up to 20, were calculated for all the 1000 simulated beams. Figure 6.14 shows the mean of the correlations at each lag, giving us that a mean autocorrelation between two neighbouring voxels at 0.13 due to the overlap between voxels presented in section 4.1.1. The mean of the autocorrelations for all other lags are negative and small (< 0.016 in absolute value). In the next chapter we will compare this to the autocorrelations in the real data.

Because a voxel is correlated to the neighbouring voxels at the same distance from the transducer from the overlap between beams, there will be an additional indirect correlation between voxels along beams. We did not model this additional autocorrelation, as it needs to go through 3 steps to reach the next voxel along the beam, which probably makes the effect of it small.

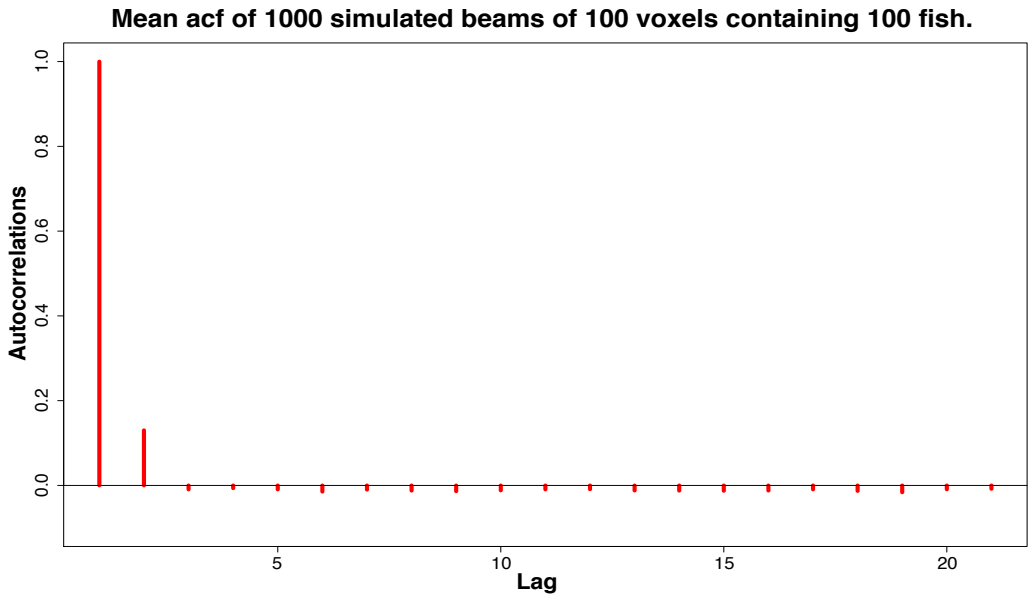

Figure 6.14: Mean empirical autocorrelation for all 1000 simulated beam of 100 voxels, taking overlap between voxels into account.

Chapter 7

Statistical analysis.

While the discussion in Chapter 6 considered the stochastic nature of backscattering from a school on the individual level, we will now focus on revealing patterns in the Sv-values from the entire school, trying to describe the school by some set of stochastic parameters. Most of the methods we present in this chapter are implemented in Chapter 8 ("Results"). We will make use of the results from Chapter 6 in this analysis. In the previous chapter we defined the coordinate system of the fish, respective to the coordinate system of the vessel, but in this discussion, we need three coordinate systems, one global (G), one for the vessel (V) and one for the school (S), and we start by defining these.

7.1 Coordinate systems.

7.1.1 Global coordinate system (G)

For a given sequence of pings $p = 1, \ldots, P$ subject to analysis, we define (G) to be centered at the first position of the vessel in this sequence, with the x-y-plane on the surface of the sea. We give the vessel a set of time, position and rotation values $D_p^v = (t_p, x_p^v, y_p^v, z_p^v, a_p^v, b_p^v, c_p^v)$, $p = 1, \ldots, P$, where the superscript v denotes position and orientation of the *vessel* with respect to the global coordinate system. Orientations are defined as a_p^v = counter clockwise rotation around the z-axis, b_p^v = counter clockwise rotation around the x-axis and c_p^v = counter clockwise rotation around the y-axis (z-x-y-rotation). For time $t_1 = 0$ we will have $D_1^v = (0, 0, 0, z_1^v, a_1^v, b_1^v, c_1^v)$.

The position and orientation of the vessel at the point t_p in time, are given in the data set as in this example:

[Volume 1]

TimeCode: 53169.3
Heading: 4.126482
Roll: -0.016929694
Pitch: 0.055676006
Heave: -0.58
Latitude: 67.8408103
Longitude: 11.740668683333332

Here, "TimeCode" is seconds elapsed the given day of the survey; "Heading" is angle *clockwise* with north in radians, South being π; "Roll" is rotation in radians *counter clockwise* around the direction of the vessel; "Pitch" is upwards angle with horizontal of the direction of the vessel (*counter clockwise* around the x-axis), given in radians; "Heave" is elevation of the vessel in meters; and "Latitude" and "Longitude" is the position in the global coordinate system of Earth.

The transformation from these dynamics to D_p^v needs a bit of attention. We consider Earth to be a circular ball, although it really has approximately 20 meters longer radius at the Equator than at the poles. The coordinates x and y in (G) will thus have the following connection to "Latitude" and "Longitude":

$$y_p = (\text{Latitude}_p - \text{Latitude}_1)\frac{\pi}{180} \cdot r$$

and

$$x_p = (\text{Longitude}_p - \text{Longitude}_1)\frac{\pi}{180} \cdot r\cos(\text{Latitude}_p).$$

To complete the transformation from the dynamics given in the data set to D_p^v, we observe that "Heading" is defined clockwise in the data set, while it is defined counter clockwise in D_p^v. We thus complete the connection between dynamics data and D_p^v:

$$\begin{aligned} t_p &= \text{TimeCode}_p \\ z_p^v &= \text{Heave}_p \\ a_p^v &= -\text{Heading}_p \\ b_p^v &= \text{Pitch}_p \\ c_p^v &= \text{Roll}_p \end{aligned}$$

7.1.2 Coordinate system of the vessel (V)

B-values in the data set (defined in (2.14)) represent the density of objects scattering sound in voxels positioned in the coordinate system of the vessel. We define this coordinate system as centered at the position (x_p^v, y_p^v, z_p^v), and rotated (a_p^v, b_p^v, c_p^v) relative to the global coordinate system. We need positions in (V) to be translated and rotated into (G), and will use the transformation matrices presented in Appendix A, to do this.

It is given in product specification of the MS70 sonar (AS, 2006), that the sonar compensates for roll motion in the range $(-10°, 10°)$. However, this roll motion is not defined in the product specification, and is easily confused with the roll angle of the vessel defined in D_p^v. By visual analysis of the bottom noise, displayed in Figure 7.6, we were able to identify the roll compensation as being linked to a coordinate system of the sonar, having roll motion defined as roll around the axis of maximum acoustic intensity of beam number $(13, 20)$, corresponding to the negative x-axis in (V). Figure 7.6 is a plot of regenerated fish/bottom positions presented in section 7.2.3, and in the figure the regenerated positions are rotated into (G) by taking heading a_p^v and pitch b_p^v into account. We can see from the figure, that the bottom noise has a fluctuating slope (plotted as blue lines), corresponding to the pitch of the vessel (shown in the lower right corners of the frames). Thus the roll compensation of the sonar involves a pitch compensation of the vessel, corresponding to $b_p^v = 0$ for all pings. In the beginning of chapter 8 we investigate the motion compensation of the system further, based on the centers of mass of the school.

If we name a position vector in (G) $\mathbf{v}_G$, and give the vessel the position vector $\mathbf{s} = (x_p^v, y_p^v, z_p^v)$, a point $\mathbf{v}_V$ in the coordinate system of the vessel will then have the following connection to $\mathbf{v}_G$:

$$\mathbf{v}_V = \mathbb{A}_{\mathrm{G}\to\mathrm{V}} \cdot (\mathbf{v}_G - \mathbf{s}),$$

where $\mathbb{A}_{\mathrm{G}\to\mathrm{V}} = \mathbb{A}_{zy}(a_p^v, c_p^v)$ is presented in Appendix A. The reversed operation will be

$$\mathbf{v}_G = \mathbb{A}_{\mathrm{G}\to\mathrm{V}}^{-1}\mathbf{v}_V + \mathbf{s} = \mathbb{A}_{\mathrm{V}\to\mathrm{G}}\mathbf{v}_V + \mathbf{s}, \tag{7.1}$$

so that we need to rotate first, and then add the vessel position. The rotation matrix from (V) to (G) is found from (A) to be $\mathbb{A}_{\mathrm{V}\to\mathrm{G}} = \mathbb{A}_{yz}(-c_p^v, -a_p^v)$.

7.1.3 Coordinate system of the school (S) - analysis of the center of mass.

The center of mass ξ_p of the school will serve as the origin in the coordinate system (S) of the school at each ping $p = 1, \ldots, P$. If we are able to estimate the center of mass at several following time steps, we can calculate an estimated velocity of the school, and use this as the direction of the y-axis of (S). We define the x-axis of (S) to be horizontal prior to the analysis.

Calculation of ξ_p will be done by two methods; one crude and one accurate. The crude method considers only the centers of the voxels belonging to the school, assuming that differences in volume and acoustic backscattering from voxels are negligible. The accurate one, takes these differences into account, weighing the voxels by the product of volume and acoustic intensity, represented by $V_{ijk} \cdot B_{ijk}$ for voxel number (i, j, k).

In either method we need to identify the voxels that belong to the school. This is in itself a great statistical challenge, and will not be analyzed in this master thesis. Maybe such a statistical identification routine should consider the average of the result from several methods, as noise and variability might lead to different conclusions depending on the method. In the following however, we will use identification values from the Sonar Explorer (Balabanian et al., 2007), found using a flood-fill algorithm on a median-smoothed version of the data set:

A seed point in the middle of the school is chosen by visual inspection, from which the Sonar Explorer calculates identification values by the function

$$f = 1 - \left(\frac{d}{t}\right)^2.$$

Here d is the difference between the value in a voxel and the seed point value, and t is the tolerance, at which the difference d results in $f = 0$. Voxels having $d > t$ is set to $f = 0$. The set of voxels with f greater than or equal to some desired limit in the range $(0, 1)$, at ping p is called M_p. One can object to this flood-fill algorithm, that it contains no automatic detection process. The user must manually set the seed point where there appears to be a school. There is also no statistical justification for the algorithm, as would be natural for such a problem. We will later see that the segmentation of the school treated in this master thesis, found by the algorithm flood-fill algorithm, seems to have limited accuracy.

Once this identification procedure has been performed, we calculate the center of mass ξ_p of the school by the more accurate method through these three steps:

1. Find the centers of the voxels identified as belonging to the school, which represents the centers of mass of the voxels.
2. Calculate the volume of the voxels and multiply it by the corresponding B-values.

3. Sum up the x- y- and z-coordinates, weighted by the products $V_{ijk} \cdot B_{ijk}$ for all voxels $(i, j, k),\ i = 1, \ldots, I,\ j = 1, \ldots, J,\ k = 1, \ldots, K$, and divide by the total mass of the school, $\sum_{\text{school}}(V_{ijk} \cdot B_{ijk})$.

In the crude method step 2 and 3 is replaced by the simple average of the midpoints from step 1.

The use of centers of voxels as the centers of mass of the voxels, is motivated from the assumption that fish are distributed uniformly throughout a voxel (as claimed in section 6.2.2). Although this probably is not quite true generally, any other assumption would displace the center of mass of a uniformly distributed school in some systematic way. If B-values from the sonar were to exactly give the density of fish in the voxels, we could develop an interpolation method to find a probable density distribution in each voxel (other than uniform). However, since a single B-value is exactly or nearly exponentially distributed, with squared coefficient of variation larger than or equal to 1, as displayed in Table 6.3.2, B_{ijk} will be a very inaccurate measure of the fish density in voxel number (i, j, k).

Since the voxels, as defined in Chapter 4, are not exactly rectangular, the center of a voxel is not an entirely meaningful concept. The definition we will use here is the midpoint of a voxel in the system of voxels $(r_{\text{mid}}, \alpha_{\text{mid}}, \beta_{\text{mid}})$, rotated into (V). This gives a midpoint positioned slightly further out from the sonar, than the center of mass of the voxel. The volumes of the voxels were calculated in Chapter 4, so the rest of the weighted calculation of ξ is straight foreward.

For a sequence of P subsequent estimated centers of mass of the school, $\xi = (\xi_1, \ldots, \xi_P)$ given in the global coordinate system (G), we will now estimate the direction of the school. The simplest representation of the direction of the school would be the straight line giving the minimum sum of squared distances between $\xi_1, \ldots, \xi_P$ and the line. This will of course only hold for a school in motion, and where there are no clear evidences that the school turns or splits into fractions. Such difficulties are left to future analysis.

The distance vector from a point to a line in 3D is simple to calculate. If we name a point $\mathbf{p}$ in (G), and a unit vector $\mathbf{u}$ along the line L running through $\mathbf{p}$ (Figure 7.1), the shortest vector $\mathbf{d}$, from L to a point $\mathbf{q}$ is

$$\mathbf{d} = (\mathbf{q} - \mathbf{p}) \times \mathbf{u}.$$

For the sequence ξ of centers of mass, the sum of squared distances from ξ to a line L_j is

$$\mathrm{S}_j = \sum_{p=1}^{P} \left[\left(\xi_p - \mathbf{p}_j \right) \times \mathbf{u}_j \right] \cdot \left[\left(\xi_p - \mathbf{p}_j \right) \times \mathbf{u}_j \right],$$

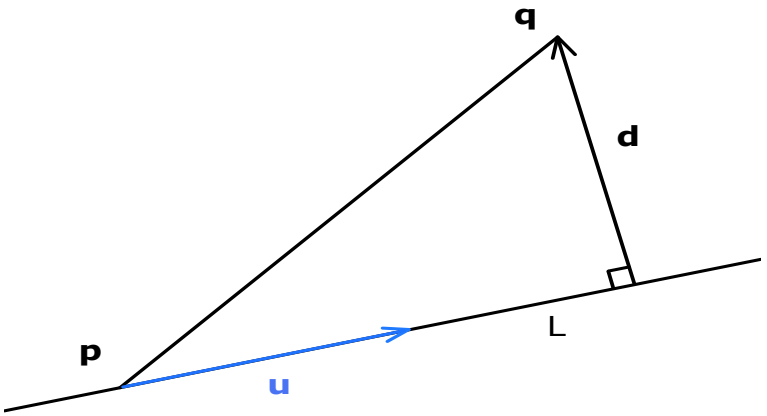

Figure 7.1: The distance from a point **q** to a line L, where the line is defined by the point **p** and the unit vector **u**.

where $\mathbf{p}_j$ and $\mathbf{u}_j$ are the point and the unit vector defining the j-th line to be checked. To find the line of minimum sum of squared distances (at least to a desired accuracy), we start by checking among $j = 1, \ldots, n^4$ lines defined by a grid of n x-values and n y-values on the x-y-plane of (G), and n θ-values and n ϕ-values for each x-y-combination. The line of best fit among these n^4 lines will then serve as the midpoint of a new, but narrower four dimensional grid. We continue this iteration until the previous line is as good as the next one.

There is of course a risk that the iteration procedure "misses" the best line, so to have a good starting point we pick the line through the first and the last center of mass, or preferably the first and the last of a moving average smoothed version of $(\xi_1, \ldots, \xi_P)$.

From the line of minimum sum of squared distances, we now get the direction (θ_ξ, ϕ_ξ) of the school. Since the coordinate system of the school is defined in the same way as the coordinate system of the fish in Chapter 6, the direction (θ_ξ,ϕ_ξ) implies a z-x-rotation $(\theta_\xi - \pi/2, \pi/2 - \phi_\xi)$ of (S) relative to (G).

There can however be a movement in ξ, even if the school is at rest compared to its surroundings. If there is a current in the sea affecting the school, we need to know the direction and strength of this current to find the movement of the school relative to the surrounding. For the data treated in this master thesis we have not compensated for the current, as we did not have information about it. This might have led to an error in the direction of the fish.

We now have the necessary tools to transform a point in the coordinate system (V) of the vessel, to the coordinate system (S) of the school, where (S) is defined with horizontal x-axis. For a position vector $\mathbf{v}_V$ in (V), we get the representation $\mathbf{v}_S$ in (S) from

$$\mathbf{v}_S = \mathbb{A}_{\mathrm{V}\to\mathrm{S}}\left(\mathbf{v}_V - \xi_p\right),$$

where ξ_p is the center of mass for a given ping. The rotation matrix $\mathbb{A}_{\mathrm{V}\to\mathrm{S}}$ consists of two separate rotations $\mathbb{A}_{\mathrm{V}\to\mathrm{G}}$ and $\mathbb{A}_{\mathrm{G}\to\mathrm{S}}$, so that

$$\mathbb{A}_{\mathrm{V}\to\mathrm{S}} = \mathbb{A}_{\mathrm{G}\to\mathrm{S}}\mathbb{A}_{\mathrm{V}\to\mathrm{G}},$$

where $\mathbb{A}_{\mathrm{G}\to\mathrm{S}} = \mathbb{A}_{zx}(\theta_\xi - \pi/2, \pi/2 - \phi_\xi)$, and $\mathbb{A}_{\mathrm{V}\to\mathrm{G}} = \mathbb{A}_{yz}(-c_p^v, -a_p^v)$ was defined in (7.1).

7.2 Variables reflecting the properties of the school.

We here present a set of 6 classes of variables aiming to describe the properties of the school. These variables will, as far as possible, be analyzed in three settings: (1) the entire school, (2) segments of the school, which will be the school divided by planes parallel to the x-y-plane, the x-z-plane and the y-z-plane of (S) and (3) the school regenerated as individual fish positions, from the B-values of the voxels identified as belonging to the school. The 6 variables to be examined are:

7.2.1 Analysis of the total school.

(a) ξ_p

The centers of mass ξ_p, for pings $p = 1, \ldots, P$, of the school, has already been discussed as a means for finding the coordinate system (S) of the school. However, there is more information in ξ_p than the direction of the school. The trace of ξ_p can be considered as a three dimensional time series, which can be decomposed into the three orthogonal directions that best explain the variance in ξ_p. This is done by principal component analysis (PCA). We briefly describe the theory behind PCA:

Principal components of the random vector $\mathbf{X} = X_1, \ldots, X_g$, are the uncorrelated linear combinations $a_{i1}X_1 + \ldots + a_{ig}X_g$, $i = 1, \ldots, g$, whose variances are successively taken as large as possible. It is a common result that the eingenvectors $\mathbf{e}_1, \ldots, \mathbf{e}_g$ of the empirical covariance matrix Σ of m observations of the random vector $\mathbf{X}$, give the principal components $Y_i = e_{i1}X_1 + \ldots + e_{ig}X_g$, $i = 1, \ldots, g$. The corresponding eigenvalues provide the amounts of the total variance of the random vector $\mathbf{X}$, that are explained by the principal

(a)	ξ_p	Center of mass of the school at ping p.
(b)	$V_p^{(T)}$	Total volume of the school at ping p.
(c)	$\sigma_p^{(T)} = \sum_{M_p} V_{ijk} B_{pijk}$ and $B_p^{(T)} = \sigma_p^{(T)} / V_p^{(T)}$	Total backscattering ability of the set M_p of voxels in the school, and ratio to total volume of the school at ping p.
(d)	PCA_p	Principal component analysis at ping p.
(e)	$\bar{B}_p$, $\text{Var}(B)_p$ and $\text{Var}(B)_p / \bar{B}_p^2$	Empirical mean, empirical variance, and empirical squared coefficient of variation of B-values at ping p.
(f)	$\hat{\rho}_{ijp}(h)$	Empirical autocorrelation for lags h along beam number (i, j) at ping p, if the beam has length $>$ some predefined value.

where $p = 1, \ldots, P$, $i = 1, \ldots, I$ and $j = 1, \ldots, J$. Note that $B_p^{(T)}$ and $\bar{B}_p$ are two different variables, one being the ratio of total backscattering to total volume of the school, while the second is simply the mean of B-values of the school.

components found from eigenvectors of Σ. Summed up we get:

Eigenvectors:	$\mathbf{e}_1, \ldots, \mathbf{e}_g$
Eigenvalues:	$\lambda_1, \ldots, \lambda_g$
Principal components:	$Y_i = e_{i1} X_1 + \ldots + e_{ig} X_g$, $i = 1, \ldots, g$
Amount of total variance explained by Y_i:	$\lambda_i / \sum_{i=1}^{g} \lambda_i \quad i = 1, \ldots, g$

We can now perform PCA on the centers of mass ξ_p, $p = 1, \ldots, P$. In the general set-up, this corresponds to $g = 3$ and $m = P$. If the school moves in some direction, the variance in the positions of centers of mass, as projected onto this direction, will be large. We can thus use the eigenvector associated to the largest eigenvalue, as a measure of the direction of the school. If the school does not move significantly, no direction can be found from the centers of mass, so there should thus be a minimum acceptance ratio $\lambda_1^{\xi} / \lambda_2^{\xi}$ (with superscript denoting the centers of mass) of the largest eigenvalue compared to the second largest eigenvalue, that separates moving schools from non-moving schools. In this discussion we will only consider moving schools, so such an acceptance ratio is left to future work.

If we project the centers of mass onto the direction found from the eigenvector corresponding to the largest eigenvalue, we will have a time series $\xi_p^{(d)}$ of one dimensional positions along this direction (with superscript denoting the *direction* of the school). The projected time series will be the y-component of the rotated centers of mass $\mathbb{A}_{\mathrm{G}\to\mathrm{S}}\xi = \mathbb{A}_{zx}(\theta_\xi - \pi/2, \pi/2 - \phi_\xi)\xi$, and will consist of a trend component, and a stationary noise process:

$$\xi_p^{(d)} = m_p + \zeta_p, \tag{7.2}$$

where m_p is a trend component and ζ_p are the random fluctuations in $\xi_p^{(d)}$. Assuming linear trend $m_p = v_\xi t_p$ for time points t_p of the pings, ordinary linear regression reveals the speed v_ξ of the school in the given direction. The stationary noise can then be estimated by subtracting m_p from $\xi_p^{(d)}$, giving $\hat{\zeta}_p$. If the assumption of linear trend is correct, $\hat{\zeta}_p$ will have expected value 0, and some variance describing the degree of fluctuations in the center of mass of the school. We thus propose that both the estimated linear trend, and the variance in $\hat{\zeta}_p$, may describe the properties of the school.

There is a weakness in the analysis of the centers of mass linked to the method for identifying the voxels that belong to the school. If this segmentation does not cover the entire school, or if it identifies voxels outside of the school as belonging to the school, ξ_p may involve errors which will be hard to identify unless a more accurate segmentation procedure is used. As we will see in Chapter 8 ("Results"), such errors in the segmentation might be the case for the school treated in this thesis. Along the discussion of variables describing the properties of the school in this chapter, we will thus aim to identify the variables that describe the school without being affected by the segmentation procedure.

As fish of some species are likely to prefer certain depths more than other depths, we can consider the mean depth of ξ_p, which we call Z_p, as a variable describing the school. Given the time of day, and the depth of the sea, Z_p might suggest, or rule out certain species.

(b) $V_p^{(T)}$

The total volume $V_p^{(T)}$ of the school might very well be a variable for species identification, and it is anyhow important in biomass estimation. Using the expression for the volume of voxels found in (4.3) in Chapter 4, we get $V_p^{(T)}$ simply by summing up the voxels identified as belonging to the school. Doing this for consecutive pings, we can detect any trend and random fluctuations of the total volume, using the method described for the analysis of $\xi_p^{(d)}$. An increase or decrease in the total volume, can only happen if the school spreads of contracts, or if groups of fish join of leave the school. Random fluctuations between pings, say of time difference 5 seconds, can hardly be described by fish leaving and joining the school, but must be caused by expansion and contraction. For a perfectly segmented school, the estimated trend in $V_p^{(T)}$, the variance in the random fluctuations of $V_p^{(T)}$, and the average of $V_p^{(T)}$ itself, can all be used as

variables describing properties of the school. As the centers of mass, the total volume $V_p^{(T)}$ is sensitive to errors in the segmentation of the school.

(c) $\sigma_p^{(T)} = \sum_{M_p} V_{ijk} B_{pijk}$ and $B_p^{(T)} = \sigma_p^{(T)} / V_p^{(T)}$

A measure of the total ability of the school to scatter sound will be the variable $\sigma_p^{(T)} = \sum_{M_p} V_{ijk} B_{pijk}$, where M_p is the set of voxels identified as belonging to a school at ping p. Defining B_{pijk} to be the number of bubbles of air of cross sectional area $b = 1\text{mm}^2 = 10^{-6}\text{m}^2$ in voxel number (i, j, k) at ping p, as in (2.14), $\sigma_p^{(T)}$ will be the total number of such bubbles in the school, as seen from the transducer. This will be a better measure of biomass than $V_p^{(T)}$, but it requires knowledge of the size and type of fish, and the distribution of orientation of the fish. If for instance the observed school is mackerel, which lacks swim bladder, the backscattering would be much less than that of an equally sized school of herring.

As the total backscattering $\sigma_p^{(T)}$ is dependent on the size of the school, we consider the ratio $B_p^{(T)} = \sigma_p^{(T)} / V_p^{(T)}$ to be a variable that might describe the properties of the school. If a good segmentation exists, the size S of the fish may be detected using this ratio. We then assume that the space expected to be occupied by one fish, $V^{(F)}$, is known as a function of fish length. This can for instance be $V^{(F)} = (\kappa S)^3$, where κ is a value specific for each species. (Pitcher and Partridge, 1979) showed through experiments for saithe, herring and cod, that κ is dependent on the fish type and speed of the school, but can generally be set to 1. Because all schools of a species are not the same, we may consider κ to be a random variable of some kind, with mean and variance specific for each species. In addition we assume that the mean backscattering cross section $\bar{\sigma}_{sp}$ of the fish, is proportional to the square of mean fish length $\bar{S}^2$, referring to the remark at the end of section 6.2.3. We write this as $\bar{\sigma}_{sp} = \varepsilon \bar{S}^2$, where ε too is a random coefficient, with mean and variance specific for each species. The coefficient ε will be dependent on the frequency f, and the depth z if the species have a swim bladder.

If we for ping number p consider a school of N_p fish, at a certain depth z, we will have total volume $V_p^{(T)} = N_p \bar{V}^{(F)}$, and total backscattering $\sigma_p^{(T)} = N_p \bar{\sigma}_{sp} \bar{I}$, where $\bar{I}$ is the mean of $B_T\left(\theta^T, \phi^T\right) B_F\left(\theta', \phi'\right) \eta_\Omega \eta_c$ of all the fish in the school (referring to the sonar equation (6.15)). For two different species both having swim bladders, and with mean fish lengths $\bar{S}'$ and $\bar{S}$ satisfying $\bar{S}' = \nu \bar{S}$ for some constant ν, we get:

$$B_p^{(T)} = \frac{\sigma_p^{(T)}}{V_p^{(T)}} = \frac{\varepsilon \bar{I}}{\kappa^3 \bar{S}} \qquad \text{and} \qquad B_p'^{(T)} = \frac{\sigma_p'^{(T)}}{V_p'^{(T)}} = \frac{\varepsilon' \bar{I}'}{(\kappa')^3 \bar{S}'}$$

$$\Longrightarrow \frac{B_p'^{(T)}}{B_p^{(T)}} = \frac{\varepsilon'}{\varepsilon} \left(\frac{\kappa}{\kappa'}\right)^3 \frac{\bar{I}'}{\bar{I}} \frac{1}{\nu}.$$

If we consider two schools of fish having the same orientation distribution, the ratio $\bar{I}'/\bar{I}$ will be 1. For two fish types having somewhat similar ε and κ, and $\nu = 2$, the smaller fish would scatter twice as much sound as the larger. In the case where the fish in one of the schools lack swim bladders, $\sigma_p^{(T)}$ for the fish without swim bladder will be much smaller, and $B_p'^{(T)}/B_p^{(T)}$ might contain enough information to identify the school with fish lacking swim bladders.

The ratio $B_p^{(T)} = \sigma_p^{(T)}/V_p^{(T)}$, as an indication of fish length, can of course be unreliable if there are errors in the segmentation of the school. In addition, the knowledge of ε and κ as random variables, might be limited, so that the information in $B_p^{(T)}$ about size, is inaccessible. Instead one could get knowledge of which $B_p^{(T)}$-values that are expected from a school of a given species at depth z, registered by the MS70 sonar, with a corresponding standard deviation. By this we will know which species are hard to distinguish and which are easier to distinguish, based on the variable $B_p^{(T)}$.

If the ratio $B_p^{(T)}$ varies in time, the reason is most likely to be at least one of the these three reasons: Changes in the density of fish in the school, changes in the mean orientation of the fish in the school, and errors in the segmentation of the school. Since the fish are spatially restricted by the behaviour zones presented in the IBMs in chapter 1, and are more free to change the orientation, we would expect rapid changes to be due to changes in the mean orientation, rather than density changes. The effect of segmentation errors is unknown, so unless an error free segmentation exists, the fluctuations in $B_p^{(T)}$ should not be trusted as a describing variable.

(d) PCA$_p$

The theory behind principal components have already been explained. An immediate approach would be to use PCA on the three-dimensional midpoints of the voxels identified as belonging to the school. However, this would be useless, since these midpoints are highly correlated, as they are dense points on rays pointing outwards from the transducer. As mentioned in Chapter 4, the voxels are typically 10 meters in height and width, but only 0.379 meters thick, so we can consider pearls on strings attached to the transducer, when picturing the midpoints of voxels. This gives high correlation between midpoints, forcing us to project onto planes, and analyze the resulting two-dimensional covariance matrix. The natural planes to project onto are the x-y-plane, the x-z-plane and the y-z-plane of (S).

Using the eigenvectors associated to the largest eigenvalues of the covariance matrix of midpoints projected onto the x-y-plane, and onto the y-z-plane, we define the direction $(\theta_o'^p, \phi_o'^p)$ of the *oblongness* of the school in (S), for each ping p. The prime refers to the school and is consistent with the use of primes in chapter 2 and 6, for angles with respect to a fish. To find $(\theta_o'^p, \phi_o'^p)$ we simply transform from cartesian to spherical coordinates of the two eigenvectors in the x-y-plane, and in the y-z-plane of (S). The angles $(\theta_o'^p, \phi_o'^p)$ imply a rotation of the y-axis of (S), which has the direction $(\pi/2, \pi/2)$. The rotation will thus be $(\theta_o'^p, \phi_o'^p) - (\pi/2, \pi/2)$. In section 7.1.3 we defined the direction (θ_ξ, ϕ_ξ) of the school in the global coordinate system (G), found from the centers of mass. The direction (θ_o^p, ϕ_o^p) of the oblongness for each ping p, represented in (G) will thus be:

$$(\theta_o^p, \phi_o^p) = (\theta_\xi, \phi_\xi) + (\theta_o'^p, \phi_o'^p) - (\pi/2, \pi/2). \tag{7.3}$$

If the direction (θ_ξ, ϕ_ξ) found from ξ is valid, it would be natural but not necessary, to expect that (θ_o^p, ϕ_o^p) and (θ_ξ, ϕ_ξ) do not differ very much. This would mean that the direction of the school coincide with the largest axis in a three dimensional ellipsoid representing the school. We assume here that the school has oblong shape in the direction of the school (Pitcher, 1980). The rotation $(\theta_o'^p, \phi_o'^p) - (\pi/2, \pi/2)$ may thus serve as a describing variable reflecting how determined the school is to move in a defined direction (the *determination* of the school). The oblongness itself may also be used to describe the school. Defining the largest eigenvalue in the x-y-plane, the x-z-plane and the y-z-plane of (S), to be λ_1^{xy}, λ_1^{xz} and λ_1^{yz}, the oblongness may be described by the mean of the ratios $\lambda_1^{xy}/\lambda_1^{xz}$ and $\lambda_1^{yz}/\lambda_1^{xz}$, or simply just one of them, since the two will be fairly similar.

Necessary conditions for using the rotation $(\theta_o'^p, \phi_o'^p) - (\pi/2, \pi/2)$ as a describing variable of the school, are that the current in the sea has been accounted for, and that the segmentation of the school is free of errors. As we will see in Chapter 8, none of these conditions are fulfilled in the case of the school treated in this thesis. We thus define a second coordinate system (S') of the school, which is a counter clockwise zx-rotation of (S), by the angles $(\bar{\theta}_o' \bar{\phi}_o') - (\pi/2, \pi/2)$ defined by the sum of the P eigenvectors corresponding to the largest eigenvalues in the xy-plane and in the yz-plane respectively. We here assume that the direction of the oblongness of the school, does not change during the observation. The rotation is done through multiplying by the rotation matrix $\mathbb{A}_{\mathrm{S}\to\mathrm{S'}} = \mathbb{A}_{zx}(\bar{\theta}_o' - \pi/2, \bar{\phi}_o' - \pi/2)$. The mean direction of the school in (G), as defined by the eigenvectors, will according to (7.3) be $(\bar{\theta}_o, \bar{\phi}_o) = (\theta_\xi, \phi_\xi) + (\bar{\theta}_o', \bar{\phi}_o') - (\pi/2, \pi/2)$. For the data treated in this master thesis, (S') will be used as the the coordinate system of the school, because the conditions mentioned above are violated.

In the beginning of section 7.1.3 we defined the x-axis of (S) to be horizontal. The idea behind this is that there is no collective consciousness of the school, that knows wether the school as a whole tilts on one side or another. Any such deviation from a horizontal x-axis, must be random, or due to the school shifting direction or shape. A roll angle c^s of this kind can be found from the the eigenvector associated to the largest eigenvalue of the covariance matrix of midpoints projected onto the x-z-plane of (S). If c^s differs much from zero, this might be an indication on some unusual state of the school, as a turn or that two schools of different depth joins.

From the midpoints represented in (S') we find the smallest rectangular box that contains all midpoints for each ping p, defining the length L_S^p, width W_S^p and height H_S^p of the school (with subscripts denoting the school). Interesting variables will in then be the degree of centrality of the school in the x-direction, y-direction and z-direction at each ping, denoted by C_x^p, C_y^p and C_z^p. The degree of centrality in the x-direction will be the distance from x-coordinate the center of mass to the front end of the rectangular box, divided by the distance from x-coordinate the center of mass to the tail end of the rectangular box, for each ping. In the y-direction and in the z-direction the degree of centrality is defined similarly. This variable is presented in (Hemelrijk and Kunz, 2004).

(e) $\bar{B}_p$, $\mathrm{Var}(B)_p$ and $\mathrm{Var}(B)_p/\bar{B}_p^2$

The mean $\bar{B}_p$ of all B-values from voxels identified as belonging to the school, is nearly the same variable as $B_p^{(T)} = \sigma_p^{(T)}/V_p^{(T)}$ treated in part (c) of this section. The difference lies in the fact that the volume of a voxel is dependent on its number (i, j, k). If voxels were identical, $\bar{B}_p$ and $B_p^{(T)}$ would be equal. The mean and variance of B-values, and shape of the histogram of B-values, are still important, and may reflect properties of the school.

At the end of section 6.3.1, we showed that B-values are exponentially distributed with expected value equal to the sum $\sum_{l=1}^{n} I_l$ of the n individual acoustic intensities contributing to the respective B-value. This sum is in turn stochastic, as it is a function of the sizes, positions and orientations of the n fish, which all are random variables. The expected B-values are most sensitive to randomness in the orientation, as shown in Table 6.2.3. We thus get a specter of expected B-values even if the fish in a school are regularly spaced, and have similar sizes. Such a specter of expected values may cause the squared coefficient of variation $\mathrm{Var}(B)_p/\bar{B}_p^2$ of the B-values to increase, and as seen in Table 6.3.2, this happens for number of fish $n = 30$ and size of the swim bladder model $\mu_L = 0.05$. For nearly uniformly distributed orientation angles α^F of the fish, the simulations resulted in $v_B^2 \approx 1.9$. An increasing number of fish contributing to a B-value, reduces the variance in $\sum_{l=1}^{n} I_l$, and the squared coefficient of variation approaches 1.

An increase in $\mathrm{Var}(B)_p/\bar{B}_p^2$ may also be caused by changes in the number of fish contributing to the B-values, or changes in the mean orientation of the fish throughout the school. We thus have two reasons for an increased $\mathrm{Var}(B)_p/\bar{B}_p^2$: (1) randomness in the individual acoustic intensities, and (2) changes in the number of fish or the mean orientation of the fish. Reason (1) is only likely if the numbers of fish contributing to the B-values are small, and the sizes of the fish are large. If we consider the cylindrical subvolume defined in section 6.2.1, where $\gamma_{max} = 2.36°$ as used in the simulations resulting in (6.23), and where $k = 697$ which is the mean radial number of the B-values identified as belonging to the school, a number of fish $n = 30$ in this subvolume implies more than 9 square meters per fish. This conflicts with the desire of the fish to stay together in schools, so we will focus on relating any large values of $\mathrm{Var}(B)_p/\bar{B}_p^2$ to changes in fish density and orientation throughout the school.

Calculating the squared coefficient of variation of the B-values, for all pings where the whole school is inside the sonar volume, we get a series of values whose mean and variance both are interesting variables, possibly describing the school. However, the use of $\mathrm{Var}(B)_p/\bar{B}_p^2$ requires an error free segmentation of the school. If many B-values from voxels outside the school are considered when calculating the squared coefficient of variation, both the mean and the variance of B-values are affected.

(f) $\hat{\rho}_{ijp}(h)$

Since a voxel in the middle of the sonar volume will have width and height typically 10 meters, and radial thickness 0.379 meters, the resolution is much higher along beams than across beams. We will thus examine the empirical autocorrelations of sequences along beams, identified as belonging to the school, and we only look at sequences of length greater than a minimum length, to ensure some accuracy in the empirical autocorrelations. This minimum length will be set to 40, which gives us a total of 684 sequences of interest. For each

of the lags $h = 0, \ldots, 20$ we average empirical autocorrelations for all 684 sequences, giving $\hat{\rho}^{(T)}(h),\ h = 0, \ldots, 20$. This will also be an average over the 12 pings at which the school is observed, so no development in time is examined. Analysis of the time development of autocorrelations is left to future work.

In Chapter 6, section 6.3.3, we calculated the autocorrelations of 1000 simulated beams of lengths 100 voxels, taking the radial overlap between voxels described in section 4.1.1 into account. A number of 100 radial fish positions were drawn, and the "fish" were given equal backscattering ability, except for the radial weighting η_r given in (6.16). The resulting mean autocorrelations are plotted in Figure 7.2, along with the empirical autocorrelations described above. We see that the simulated autocorrelations do not explain the mean of the empirical autocorrelations very well. The simulated autocorrelations were based on an equal number of fish with equal backscattering ability in each voxel, which is unlikely to happen in a real school. In section 7.1.3 we showed that a beam radiating through the school treated in this thesis, gradually enter and leave the school, so that gradual changes in B-values for a sequence of a beam identified as belonging to the school must be expected. In addition there may be changes in fish density and orientation throughout the school.

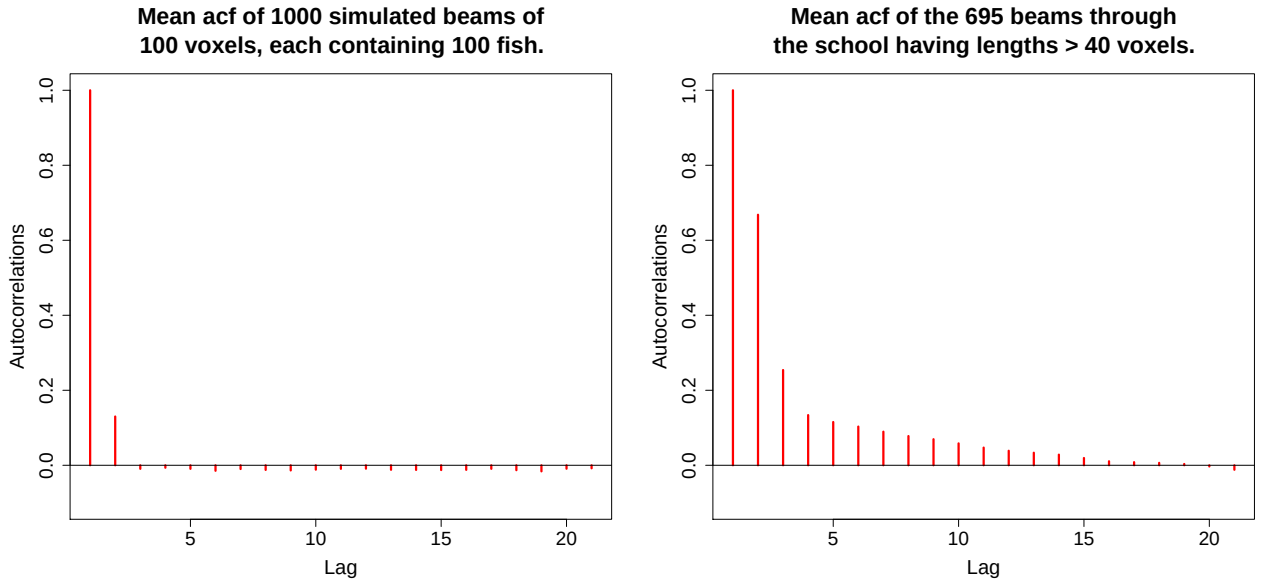

Figure 7.2: **Left**: Mean autocorrelation of the beams simulated in section 6.3.3. **Right**: Mean autocorrelation of all sequences along beams, identified as belonging to the school, of lengths > 40.

Figure 7.3 displays $\hat{\rho}_{12,i,10}(h), i = 1, \ldots, 12$, (the horizontal fan having $j = 10$ for ping $p = 12$). We observe that there are large deviations between the plots, with generally larger autocorrelations for the beams that radiate through the main parts of the school. The mean empirical autocorrelation $\hat{\rho}^{(T)}(h)$ indicate that neighbouring voxels are on average highly correlated ($\hat{\rho}^{(T)}(1) = 0.67$), and that there is also some correlation to the next to nearest neighbour ($\hat{\rho}^{(T)}(2) = 0.25$), but that for lags $h > 2$ the correlation is not very large on average ($\hat{\rho}^{(T)}(h) < 0.14,\ h = 2, \ldots, 20$). Since the thickness of the voxels are only 0.379 meters, lag h corresponds to $h \cdot 0.379$ meters, so voxels that are more than one meter away, seems to be not very much correlated. However, as Figure 7.3 shows, there are large differences between the beams, and beams that radiate through the outskirts of the school might contribute to a lower $\hat{\rho}^{(T)}(h)$.

As for many other variables presented in this chapter, $\hat{\rho}^{(T)}(h)$ may react to errors in the segmentation of the school.

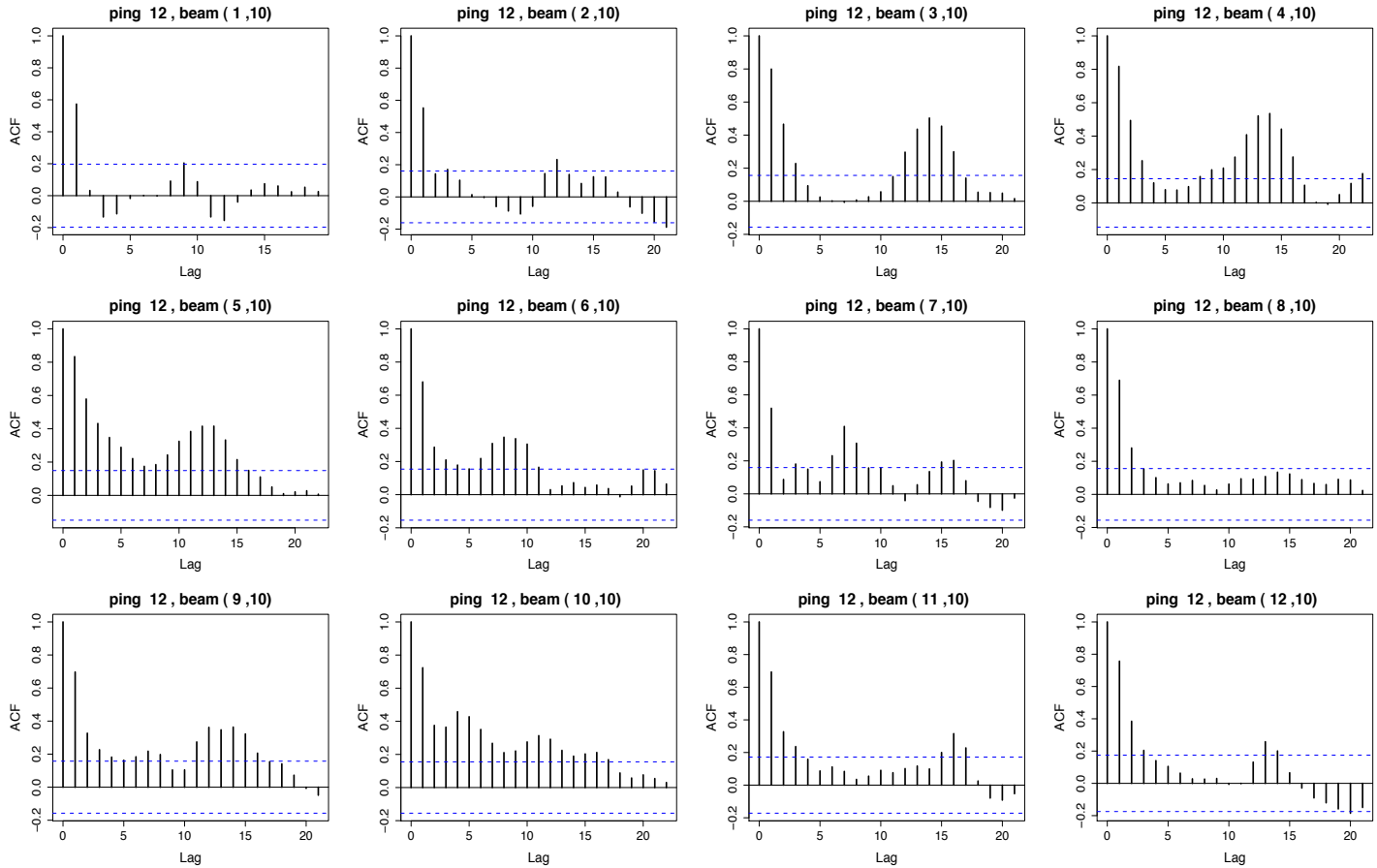

Figure 7.3: Autocorrelations of 12 beams in horizontal fan number $j = 10$ for ping number $p = 12$. 95 % confidence bounds $\pm 1.96/\sqrt{\text{length of sequence}}$ are plotted in blue dashed lines.

7.2.2 Analysis of parts of the school.

We wish to analyze parts of the school, to describe the symmetry or "shape" of the school. Of the classes of variables listed in the beginning of section 7.2 we only consider (b), (c) and (d). This is because the center of mass (a) of a part of the school is dependent on the part, and because considering parts only, makes beams shorter, largely ruling out the autocorrelations (f). In addition we do not believe that the squared coefficients of variation of the B-values of parts of the school will give any additional information on the properties of the school, unless the part considered is small so that the number of B-values is small. We thus do not consider the variable presented in part (e) of section 7.2

To define the partitioning of the school we consider the ranges of x-, y- and z-values in (S) or (S'), but to make the partitioning less sensitive to errors in the segmentation of the school, and less sensitive to the overlap between voxels, we define these ranges using quantiles of the products of volume and B-value for the voxels in the school. These quantiles will be specified by the value c_q, so that in the x-direction, the range $(x_p^{(1)}, x_p^{(2)})$ is defined by:

$$x_p^{(1)} : \sup_{x_p^{(1)}} \left(\frac{1}{\sigma_p^{(T)}} \sum_{x_{pijk} < x_p^{(1)}} B_{pijk} V_{ijk} \leq c_q \right) \quad \text{and} \quad x_p^{(2)} : \inf_{x_p^{(2)}} \left(\frac{1}{\sigma_p^{(T)}} \sum_{x_{pijk} > x_p^{(2)}} B_{pijk} V_{ijk} \geq 1 - c_q \right), \tag{7.4}$$

where x_{pijk} is the midpoint of voxel number (i, j, k) for ping number p, and the numbers (p, i, j, k) are restricted to the set M_p of voxels identified as belonging to the school for ping p. Similar expressions define the ranges in the y-direction and in the z-direction. By this method we ignore parts at the ends of the school that do not seem to be fully integrated in the school. We propose that an appropriate value for c_q is 0.01, so that the middle 98% of the school is considered in all three directions x, y and z.

We now consider all voxels having x-values of midpoints in the lower half and in the upper half of the range of x-values, labeling them left side voxels (LS) and right side voxels (RS) respectively. Similarly we use this scheme for partitioning with regard to y-values and z-values of midpoints of voxels. We define these 7 parts: (LS), (RS), tail part (T), middle part (M), front part (F), lower part (L) and upper part (U). The parts (T), (M) and (F) are defined by the planes 0, 0.25, 0.75 and 1, where the range of y-values is modified to (0,1).

Modified to the 7 parts q =(LS),(RS),(T),(M),(F),(L),(U) of the school, we get the classes of variables to be analyzed:

(b_q)	$V_{p,q}^{(T)}$	Volume of part q of the school at ping p.
(c_q)	$\sigma_{p,q}^{(T)} = \sum_{M_{p,q}} V_{ijk} B_{pijk}$ and $B_{p,q}^{(T)} = \sigma_{p,q}^{(T)} / V_{p,q}^{(T)}$	Total backscattering ability of the set $M_{p,q}$ of voxels in part q the school, and ratio to total volume of the school at ping p.
(d_q)	$\text{PCA}_{p,q}$	Principal component analysis of part q of the school at ping p.

$\mathbf{(b)}_q$ $V_{p,q}^{(T)}$

From the 7 values of $V_{p,q}^{(T)}$ for each ping p, we propose that the interesting variables to examine are the ratios $V_{p,U}^{(T)}/V_{p,L}^{(T)}$, $V_{p,F}^{(T)}/V_{p,T}^{(T)}$ and $V_{p,M}^{(T)}/(V_{p,T}^{(T)} + V_{p,F}^{(T)})$. The reason why the ratio of volume of the left side, to volume of the right side, is not considered as being interesting, is that this ratio is subject to high randomness, because a free fish has no restrictions in the orientation angle α^F. The tilt angle of a free fish, β^F, is however restricted by the desire of the fish to swim horizontally, and not to much up and down.

The use of the ratio $V_{p,F}^{(T)}/V_{p,T}^{(T)}$ between front and tail part of the school, and the ratio $V_{p,M}^{(T)}/(V_{p,T}^{(T)} + V_{p,F}^{(T)})$ of the middle part and the sum of the front and tail parts, is inspired by (Hemelrijk and Kunz, 2004). The paper refers to the findings of (Bumann et al., 1997), where the density of moving fish groups are shown to be higher in the front of the group. This is explained by a positive predation risk gradient along the direction of the school. In (Hemelrijk and Kunz, 2004), an individual based model (IBM), as described in Chapter 1, was used to simulate schools, showing a higher fish density in the front. The reason for this was that fish in the front are attracted to its neighbours to the side, since there are no fish in front of them. School sizes were approximately 9 in (Bumann et al., 1997), and 100 in (Hemelrijk and Kunz, 2004).

The 3 ratios of total volume in the 7 parts of the school, will not directly reflect the density of fish, but rather the shape of the school. In the following we consider the total backscattering $\sigma_{p,q}^{(T)}$ in each part, which reflect the number of fish, and the ratio $B_{p,q}^{(T)} = \sigma_{p,q}^{(T)}/V_{p,q}^{(T)}$ reflecting the fish density.

$\mathbf{(c)}_q$ $\sigma_{p,q}^{(T)} = \int_{V_{p,q}^{(T)}} B$ and $B_{p,q}^{(T)} = \sigma_{p,q}^{(T)}/V_{p,q}^{(T)}$

By the variables $\sigma_{p,q}^{(T)}$ and $B_{p,q}^{(T)}$ we wish to see if the same pattern appears in the data for our school observed by the MS70 sonar, as was described in (Hemelrijk and Kunz, 2004) and (Bumann et al., 1997). Here the density of real (Bumann et al., 1997) or simulated (Hemelrijk and Kunz, 2004) fish schools we observed to have greater density in the front part than in the tail part. However, the size of our school is probably several hundred thousand fish, so that similar results for the big and the small school might not have the same reasons. If we observe a higher density in the upper part than the lower part of the school, the reason might be pure chance. Analyzing the three ratios $B_{p,U}^{(T)}/B_{p,L}^{(T)}$, $B_{p,F}^{(T)}/B_{p,T}^{(T)}$ and $B_{p,M}^{(T)}/(B_{p,T}^{(T)} + B_{p,F}^{(T)})$ and the ratios $\sigma_{p,U}^{(T)}/\sigma_{p,L}^{(T)}$, $\sigma_{p,F}^{(T)}/\sigma_{p,T}^{(T)}$ and $\sigma_{p,M}^{(T)}/(\sigma_{p,T}^{(T)} + \sigma_{p,F}^{(T)})$, for many

schools is needed to find out if these variables are suited for describing school properties, and to work out a test for deciding wether the ratios results from pure chance or not.

$\mathbf{(d)}_q$ $\text{PCA}_{p,q}$

The natural planes to project the 7 parts of the school onto, are the y-z-plane, for the parts (RS) and (LS), the x-z-plane, for the parts (T), (M) and (F), and the x-y-plane, for the parts (L) and (U). If the eigenvectors of the covariance matrixes of connected parts differ, (i.e parts that are projected onto the same plane), this must either be caused by randomness in the shape of the school, or by some property linked to the species. In this thesis we only graphically analyze the principal components of the projected midpoints in the 7 parts of the school.

7.2.3 Regeneration of the school.

In this section we present a method for regenerating the school, which involves recreating artificial fish positions from the data. For a voxel (i, j, k), we use the corresponding moving average value $\hat{B}_{ijk}$, of 15 B-values along beam number (i, j), to estimate the number of fish in the voxel. This is done to reduce the random fluctuations between voxels, caused by the interference between acoustic signals from fish, and involves an assumption that the actual fish density does not change too much throughout the 15 voxels ($15 \cdot 0.38$ meters $= 5.7$ meters). The regeneration has these 6 steps:

1. Define an expected spherical backscattering cross section σ_{fish} of the fish. A large value reduces the amount of data regenerated.
2. Calculate the products $b\hat{B}_{ijk}V_{ijk}$, $i = 1, \ldots, I,\ j = 1, \ldots, J,\ k = 1, \ldots, K$, of all voxels belonging to the school, and divide the products by σ_{fish}. Here $b = 10^{-6}\ m^2$ and the calculation is according to (2.15). Rounding of the results provide the numbers n_{ijk}, $i = 1, \ldots, I,\ j = 1, \ldots, J,\ k = 1, \ldots, K$, of fish in the voxels.
3. For the number of fish n_{ijk} in a voxel, draw α-, β- and r-values, in the range of voxel number (i, j, k), defined in (4.1) and in (4.2). These angles are not the same as the orientation angles $\Omega = (\alpha^F, \beta^F)$ of a single fish, introduced in section 6.1.1.
4. Rotate all drawn fish positions from the specifications of the beams, to the cartesian coordinate system of the vessel (V), and further into the global coordinate (G) system if required.
5. Using the mean of the eigenvectors associated to the largest eigenvalue for all pings, of the three dimensional covariance matrix of regenerated fish positions, redefine the direction of the school. Use this as the y-axis in a new coordinate system of the school (S"), having horizontal x-axis.
6. Transform all regenerated fish positions into (S").

The resulting data set will still consist of blocks of fish positions, so that the school shape is edgy instead of smooth. One option might be to draw fish positions in the subvolumes S_{ijk} presented in section 6.2.1, so that the fish positions related to neighbouring voxels overlap. This would smoothen the regenerated school, and may be more in accordance with the acoustic theory. In this section however, we stick to the regeneration algorithm presented above.

The acoustic refraction discussed in chapter 4, is not taken into account in the regeneration algorithm. This might be something that needs to be done in future work. However, compensating for the refraction can be a time consuming process, if one which to do this for all the regenerated fish positions, so a way of defining voxels based on the midpoints calculated from the procedure presented in section 2.6.2, and based on the direction of the beam at that midpoint, might be a solution. One would then draw fish positions uniformly in the *refracted* voxels.

Because we after the fourth step in the regeneration algorithm, will have fish positions filling the volume of the school, as opposed to the midpoints positioned densely on rays pointing outwards from the transducer, we can perform the three dimensional principal component analysis of the fish positions. This will give the most precise definition of the oblongness and direction of the *shape* of the school, defining (S"). We use the mean of the eigenvectors associated to the largest eigenvalue for all pings as the direction, because we assume that in the brief time interval that the school is observed, (1 minute for the school in this thesis), it is natural to think that the direction does not change, unless the school is under immediate attack by a predator. As discussed previously in the chapter, the centers of mass provide the *translational* direction of the school, which define (S). Comparing these two directions will reflect the determination of the school (defined in part (d) of section 7.2.1), and will be more accurate than comparing (S) to (S'), as discussed in part (*d*) of section 7.2.1.

The regenerated school requires a different set of describing variables than the ordinary data. The direction for each ping, found from the three dimensional principal component analysis, is itself an interesting variable. Deviation from the translational direction, found from the centers of mass, have already been mentioned, and variations in the direction of the shape between pings might also be interesting, possibly reflecting orientation changes locally and globally in the school. A robust estimate of the length, width and height of the school for each ping, is provided by the ranges of y-, x- and z-values in (S"), because the B-values are taken into account. We may use a similar modification of the ranges as in (7.4).

Using the regenerated school we may also analyze arbitrary segments of the school more accurately than if we consider midpoints and corresponding B-values. We can choose the segment to be analyzed so that it is completely inside the school, thus being unaffected by errors in the segmentation of the school. An example of such a segment is a sphere of radius 5 meters centered at the centers of mass of the school. Since we are using moving average values $\hat{B}$, of 15 consecutive B-values along beams when regenerating the school, and because an arbitrary segment will contain several voxels or parts of voxels, the squared coefficient of variation of the number N_p^S of artificial fish in the segment at ping p will reduced accordingly. We will try to find a very rough estimate on this squared coefficient of variation, in order to be able to evaluate observed values:

Considering the school treated in this thesis, we have that the voxels are approximately 11 meters in width and height, and 0.379 meters deep. If the sphere of radius 5 meters is centered along the eigenvector of a beam, it will thus intercept $10/0.379 \approx 26$ voxels. The total number of artificial fish in the sphere will thus be a weighted sum of the 26 voxels, where the voxels closest to the sonar, or farthest from the sonar, will have smaller volume of intersection, thus being weighted less. Because of this weighting, we may say that the sum will correspond to the sum of $26/(\pi/2) \approx 16$ equally weighted voxels (dividing by the area of the unit half sphere). The smoothing done by considering the moving average values $\hat{B}$ when calculating the number of fish in regeneration algorithm, will only affect the contribution from the voxels closest to the sonar and farthest from the sonar, since we anyway sum up the $\hat{B}$-values from consecutive voxels. We thus propose that the effect of the moving average filter is negligible, as it is only important in for the least weighted voxels.

Another situation occur when the sphere is centered at the borderline between 4 beams, thus intercepting approximately 100 voxels. We then say that the weighted sum corresponds to approximately $100/(\pi/2) \approx 64$ equally weighted voxels. A very rough estimate of the number of equally weighted voxels in a sum corresponding to the intersection of the sphere, may thus be $(16 + 64)/2 = 40$ voxels. If the real fish are not too large and not too densely distributed, the B-values will be exponentially distributed with squared coefficient of variation equal to 1 (confront Table 6.3.2). For the voxels intercepted by the sphere of radius 5 meters, we may also assume that the number of real fish, and the mean orientation of the fish deciding the expected value of the exponential distribution in the voxels, is largely unchanged. A wide specter of expected values may increase the squared coefficient of variation, but we assume here that this is not the case for the voxels intercepted by the sphere.

When summing up 40 equally weighted voxels for the sphere of radius 5 meters, we thus get the squared coefficient of variation of the number of artificial fish in the sphere roughly estimated by $1/40 \approx 0.16^2$. Invoking the central limit theorem we thus claim that there is a 95 % probability that the number of artificial fish in the sphere at an arbitrary ping, will roughly be within $1 - 1.96 \cdot 16\% \approx 70$ % and $1 + 1.96 \cdot 16\% \approx 130$ % of the previous number of artificial fish in the sphere. If we wish to consider a sphere of radius 10 meters, we may assume that the number of intercepted voxels is 8 times as high as for the sphere of radius 5 meters, thus narrowing the above confidence interval to between $1 - 1.96 \cdot 16\%/\sqrt{8} \approx 79$ % and $1 + 1.96 \cdot 16\sqrt{8}\% \approx 111$ %. We will make use of these intervals in section 8.3 of the next chapter.

If the centers of mass of the school contains errors inherited from errors in the segmentation of the school, we might have a situation where the spherical segment "moves around" in the school. It might thus be wise to smoothen ξ_p, or simply assign to ξ_p equally spaced positions on the straight line describing the translational direction of the school, found in section 7.1.3. A robust method for identifying the movement of the school should be a key subject in future work with data from the MS70 sonar. We propose an alternative method in section 8.1.

In Figure 7.4 and Figure 7.5, the school treated in this thesis has been regenerated using $\sigma_{\text{fish}} = 350$ mm^2, and projected onto the xz-plane of (V) and (G) respectively. We have here regenerated B-values for voxels number (i, j, k), $i = 1, \ldots, 25$, $j = 3, \ldots, 13$ and $k = 527, \ldots, 888$, which is the smallest three dimensional box in the system of voxels, containing the school at all pings. Positions in voxels that are identified as belonging to the school, are plotted in red, and all other positions are plotted in black. The bottom is visible, as the

major cluster of black points. In the plots, some instrument noise is apparent for pings 6, 9 and 11. The edgy regeneration mentioned earlier, is clearly seen in Figure 7.4, where the beams are seen from the side.

Figure 7.6 refers to the discussion in section 7.1.1, concerning the motion compensation of the system of the sonar and the vessel. The difference in slope of the bottom is clearly seen as variations in the blue lines of the plot, and corresponds to the given pitch values shown in the lower right corners. The rotation of the regenerated positions in Figure 7.6 were done using a rotation matrix $\mathbb{A}_{\mathrm{V}\to\mathrm{G}} = \mathbb{A}_{xz}(-b_p^v, -a_p^v)$, assuming that roll motion c_p^v of the vessel has been compensated for in the sonar. The rotation used in Figure 7.4 and Figure 7.5 were done using the rotation matrix $\mathbb{A}_{\mathrm{V}\to\mathrm{G}} = \mathbb{A}_{yz}(-c_p^v, -a_p^v)$, , assuming that the pitch b_p^v of the vessel has been compensated for in the sonar.

Remark about the choice of $\sigma_{\mathbf{fish}}$.

For the school treated in this thesis, we have already claimed that there are hundreds of thousands of fish. If fish positions are given in 8 digits, we can approximate the memory usage of one fish position in text formate by $3 \cdot 8 = 24$ bytes (B). For a school of 500 000 fish, observed for 10 pings, we thus get a total memory usage of the regenerated school of more than 100 MB. It is therefore natural to define σ_{fish} to be large, so that the data set is reduced. Mark that this procedure is only a way of representing the data as points in space, rather than voxels assigned to B-values that represent the ability to scatter sound, of the objects in the respective voxels. There is thus no strict need for using values of σ_{fish} that are realistic. However, σ_{fish} should not be chosen too high, as this could result in too many voxels with zero regenerated fish positions.

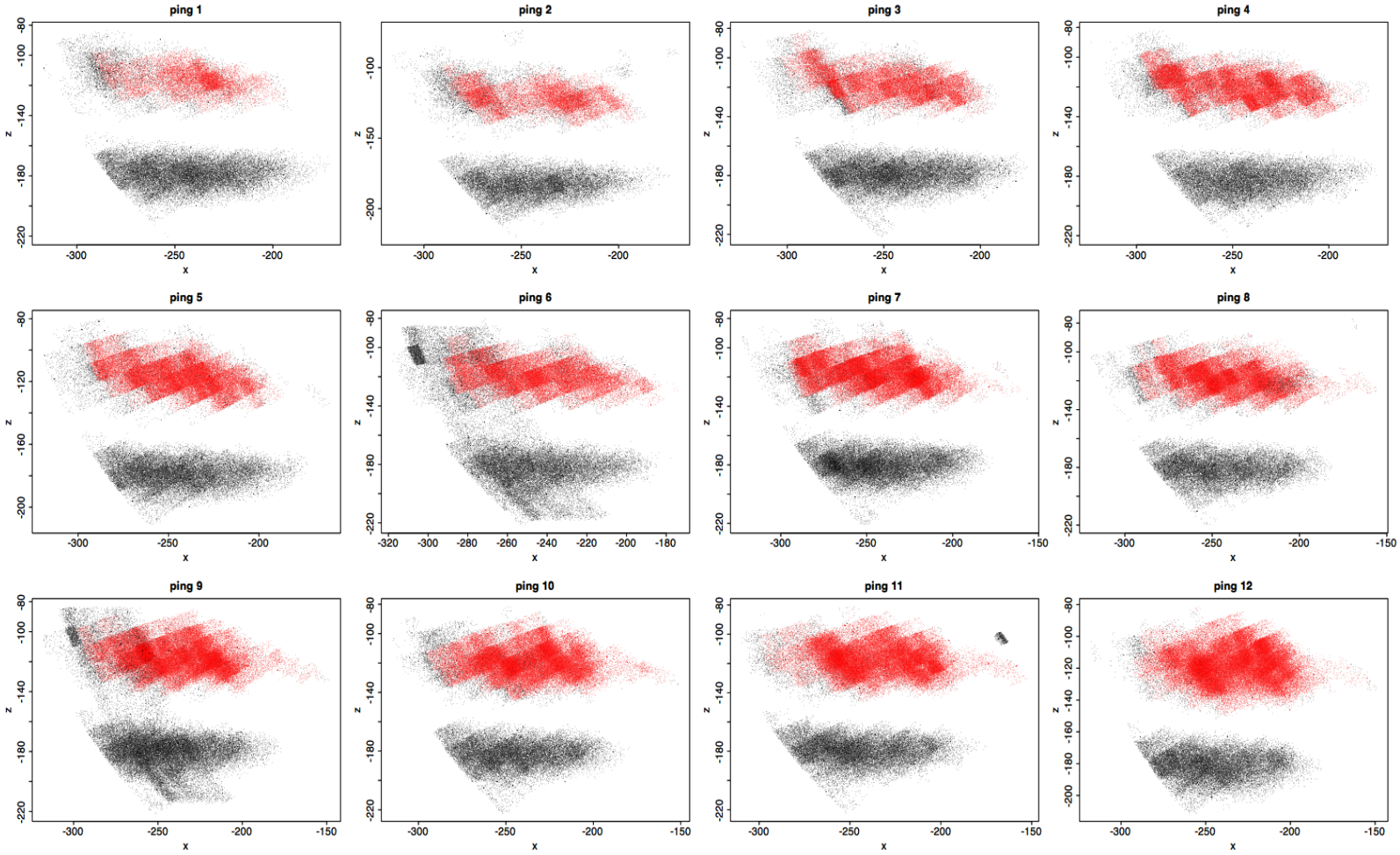

Figure 7.4: Plots of the regenerated school projected onto the xz-plane in (V). "Fish" positions from voxels identified as belonging to the school, are plotted in red, and all other regenerated positions are plotted in black. The big cluster of black positions is the sea bed.

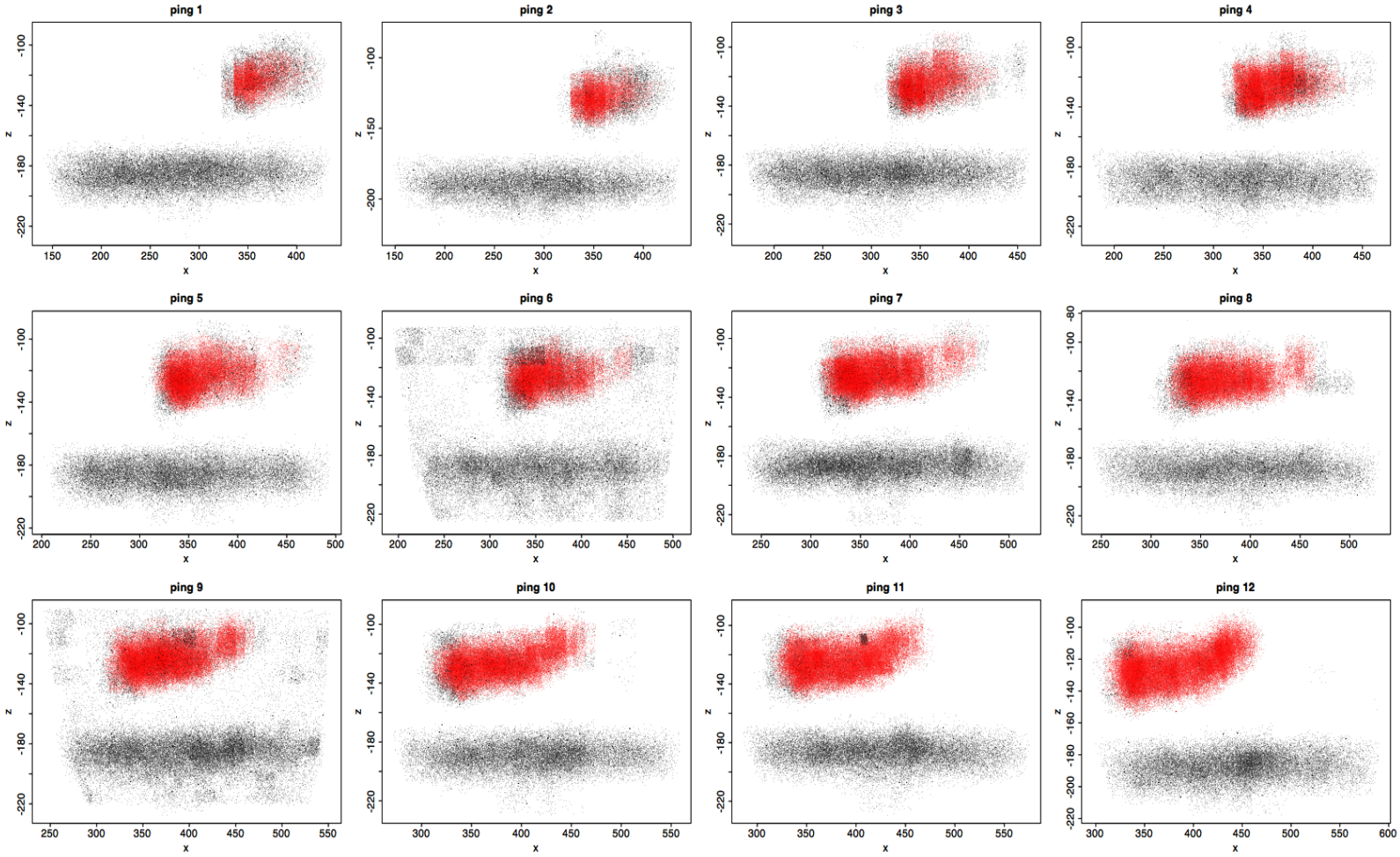

Figure 7.5: Plots of the regenerated school projected onto the xz-plane in (G). "Fish" positions from voxels identified as belonging to the school, are plotted in red, and all other regenerated positions are plotted in black. The big cluster of black positions is the sea bed.

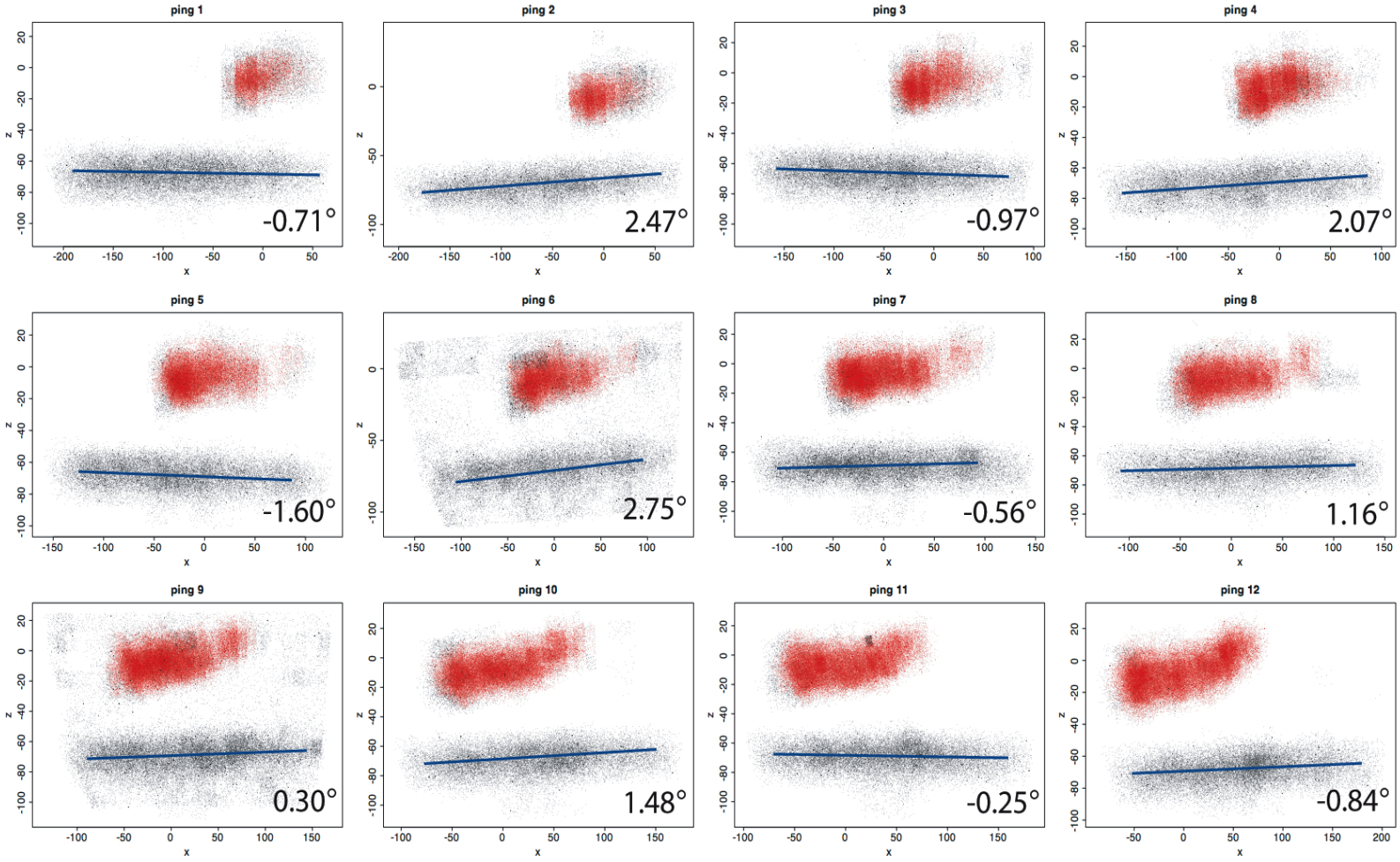

Figure 7.6: Plots of the regenerated school projected onto the xz-plane in (G). "Fish" positions from voxels identified as belonging to the school, are plotted in red, and all other regenerated positions are plotted in black. The big cluster of black positions is the sea bed, and the blue lines represent the slope of the sea bed. Pitch angles of the vessel are shown in the bottom left corners of the 12 frames.

Chapter 8

Results.

In this chapter we present the results of the methods for statistical analysis discussed in Chapter 7. These methods involve the 6 classes of variables (a) through (f) for the entire school, defined in the beginning of section 7.2; the 3 classes of variables (b_q) through (d_q) for the 7 parts of the school, defined in section 7.2.2, and the methods suggested for the regenerated school described in section 7.2.3. We go through the classes of variables in the same order as in Chapter 7.

8.1 Results for the total school.

(a) ξ_p

We calculated the centers of mass $\xi = \xi_p,\ p = 1, \ldots, 12$, in the crude way and in the more accurate way, as described in section 7.1.3. The two versions of ξ were rotated from (V) into (G) and further into (S), thus being represented in all three coordinate systems. As presented in section 7.1.2, the sonar compensates for the pitch of the vessel (defined in section 7.1.1). However, based on the possible confusion regarding which rotations have been compensated for in the system of the MS70 sonar and the research vessel, we rotated the centers of mass into (G) in three ways, using the rotation matrices $\mathbb{A}_{\mathrm{V}\to\mathrm{G}} = \mathbb{A}_{yxz}(-c_p^v, -b_p^v, -a_p^v)$, corresponding to no motion compensation in the system, $\mathbb{A}_{\mathrm{V}\to\mathrm{G}} = \mathbb{A}_{xz}(-b_p^v, -a_p^v)$, corresponding to compensation for the roll motion of the vessel, and $\mathbb{A}_{\mathrm{V}\to\mathrm{G}} = \mathbb{A}_{z}(-a_p^v)$, corresponding to compensation for the roll motion and the pitch of the vessel. The x-, z- and z-coordinates of ξ in (G) are plotted in Figure 8.1.

From the plot to the right, of z-coordinates of the centers of mass, we see that the black line corresponding to no motion compensation of the system of sonar and vessel, is unlikely to be the correct one. Since the school is observed on the port side of the vessel, the roll motion

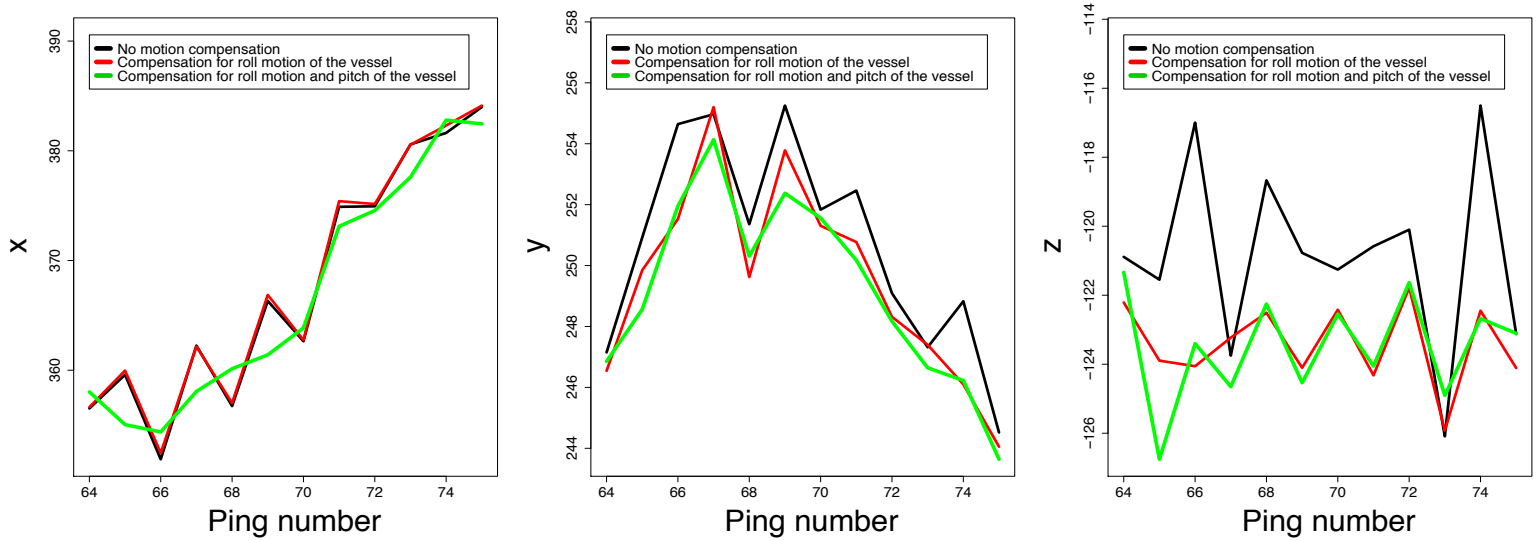

Figure 8.1: Rotation of the centers of mass ξ into (G) using three different rotation matrices. The three plots are of x-, z- and z-coordinates of ξ in (G), where the origin is defined at the first position of the vessel.

of the vessel has potentially great effect on the depth of the school, and a random roll motion would add noise to the z-coordinates of ξ. The probability that this added noise causes the variance in the depth coordinates to be smaller, as in the plot to the right in Figure 8.1, is intuitively small, so we conclude that the roll motion is compensated for in the system of sonar and research vessel. We could perform a test on wether this change in variance is likely to occur, by analyzing the random roll motion of the vessel, and adding the variance of the roll motion to the variance of the z-coordinates based on no motion compensation. However, here we confine ourselves to the visual inspection.

In section 7.1.2 we claimed that the compensation of roll motion in the MS70 sonar, specified by the manufacturer in (AS, 2006), corresponded to compensation of the pitch of the vessel. This was discovered by visual inspection of the bottom noise in Figure 7.6. The same conclusion can be drawn from the left frame in Figure 8.1, where the x-coordinates of ξ are plotted for the three different motion compensation situations:

Because the school is observed at angles with horizontal in the range $(16.57895, 40.26316)$, the pitch will have an influence on the

y-coordinates of the school in (V). The heading of the vessel is approximately 76°, as defined in section 7.1.1, so y-coordinates in (V) will largely correspond to x-coordinates in (G). If the case was that the pitch had not been compensated for in the system, we would expect the random pitch motion of the vessel to add noise to the x-coordinates in (G) of the school. However, the contrary seems to be the case if we consider the left frame in Figure 8.1. The green line, corresponding to compensation of both roll and pitch of the vessel, seems to be a smoothed version of the red and the black lines, justifying the assumption that the pitch of the vessel has been corrected for in the system of sonar and vessel. In the following, we thus consider the centers of mass rotated into (G) and further into (S), under the assumption that both roll and pitch of the vessel has been accounted for in the system.

The depth of the school may be represented by the z-component of ξ, called Z_p. As seen in Figure 8.1, the fluctuations in the depth of the school are not very large, with mean $\bar{Z} = -123.5$ and standard deviation equal 1.6 meters. As we will see several times throughout this chapter, there are reasons to believe that there are errors in the segmentation of the school, but the small value of the standard deviation of Z_p suggests that this variable is insensitive to such errors.

The traces of the centers of mass, calculated in the accurate and in the crude way, using $\mathbb{A}_{\mathrm{V}\to\mathrm{G}} = \mathbb{A}_z(-a_p^v)$ for the rotation from (V) to (G), are plotted in the global coordinate system (G) in Figure 8.2. We see that there a mismatch between the two traces (up to 20 meters in x and up to 10 meters in y but little in z). If we are sure that all significant noise has been removed, the more accurately found ξ is the one we should use, as we account for the B-values and the volumes of voxels in that method. However, the movement of the centers of mass from the two methods seem correspond, and at least for the last 6 pings, there seems to be a movement in somewhat the same direction for both traces of ξ.

The y-axis in the coordinate system (S) of the school, was proposed in section 7.1.3 to be found from ξ, by the line having the smallest sum of quadratic distances to the centers of mass. We performed these iterations on ξ, giving

$$\text{Direction found from fitted line to } \xi: \quad (\theta_\xi, \phi_\xi)_{\mathrm{acc}} = (-9.2°, 88.9°) \quad \text{and} \quad (\theta_\xi, \phi_\xi)_{\mathrm{cru}} = (-14.6°, 88.2°),$$

where the subscripts "acc" and "cru" denotes directions extracted from ξ found by the accurate and the crude method respectively. We assume that the direction found in the accurate way is the most precise, and thus define (S) as the orthogonal coordinate system centered at ξ_p for each ping, with y-axis along this direction, and with horizontal x-axis. Midpoints in the voxels can then be rotated and translated into (S).

Another way of finding the direction of the school from the centers of mass is to extract the angles θ_ξ and ϕ_ξ from the largest eigenvector of the covariance matrix of ξ, as explained in part (a) of section 7.2.1. The resulting directions found in this way from the accurate and crude centers of mass of the school treated in this thesis are:

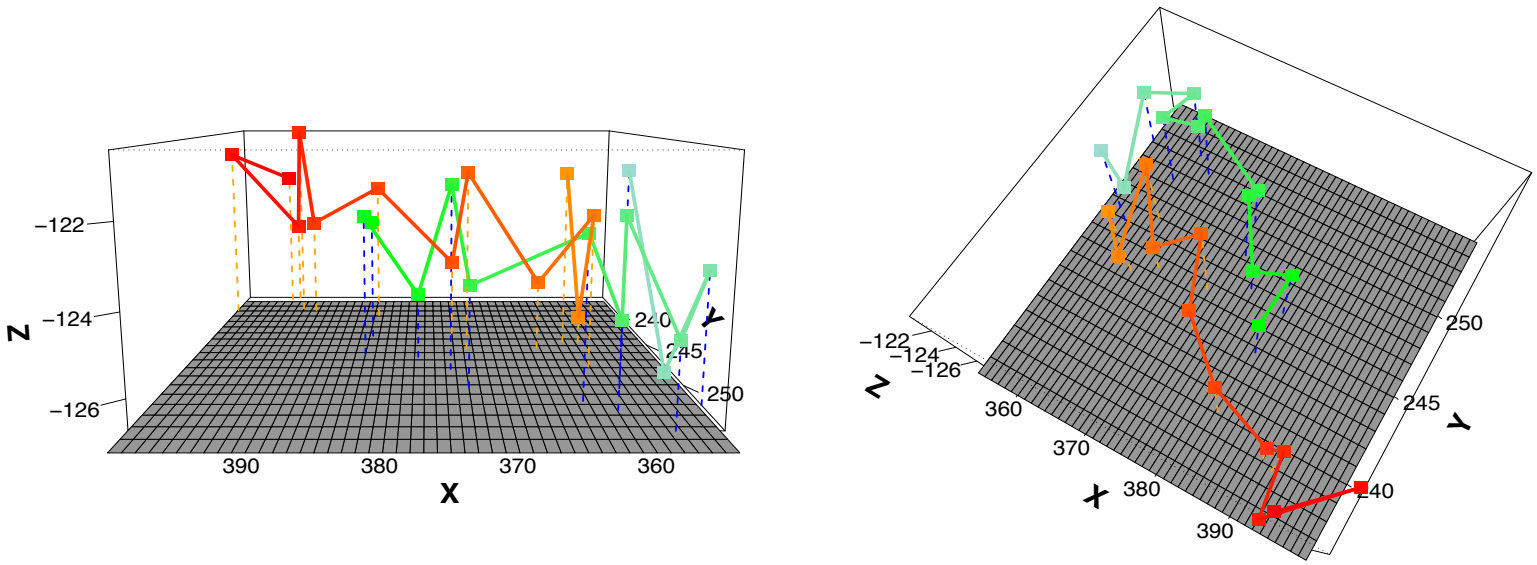

Figure 8.2: Centers of mass ξ of the school calculated in the crude way (red) and in the more accurate way (green). Coordinates are in the global system (G), and dashed lines are normal lines onto the plane $z = \min(\xi)$. Colours move from orange to red, and from light blue to green as p increases.

$$\text{Direction from PCA of } \xi: \quad (\theta_\xi, \phi_\xi)_{\text{acc}} = (-11.6^\circ, 88.2^\circ) \quad \text{and} \quad (\theta_\xi, \phi_\xi)_{\text{cru}} = (-14.0^\circ, 87.5^\circ).$$

Comparing the different directions of the school, we see that θ_ξ is the angle that is most sensitive to the method used to obtain the direction.

As suggested in part (a) of section 7.2.1 there should be a minimum acceptance ratio of the largest eigenvalue to the next to largest, separating moving schools from nonmoving schools. This ratio must be a functions of the number of pings P at which we have observed the school. We do not suggest any such ratio here, but only present the square root of the eigenvalues of the covariance matrix of ξ

found in the accurate way and in the crude way:

$$\text{Square root of the eigenvalues of } \xi: \quad (10.86, 2.20, 1.51)_{\text{acc}} \quad \text{and} \quad (14.66, 1.80, 1.09)_{\text{cru}}.$$

These will be the axes in an ellipse representing the centers of mass, so the oblongness is quite satisfying.

We now continue with the centers of mass found in the accurate way, and wish to rotate ξ into a coordinate system having y-axis along the direction $(\theta_\xi, \phi_\xi)_{\text{acc}}$ found from the eigenvector corresponding to the largest eigenvalue of the covariance matrix of ξ, and with horizontal x-axis. This will be the global coordinate system (G) rotated by in a zx-fashion by the angles $(\theta_\xi - \pi/2, \pi/2 - \phi_\xi)_{\text{acc}}$, as in section 7.1.3. We can then project the centers of mass onto the y-axis, to get the time series $\xi_p^{(d)}$ presented in (7.2):

$$\xi_p^{(d)} = v_\xi t_p + \zeta_p, \tag{8.1}$$

where v_ξ is the speed of the school, t_p are the time points for the pings, and ζ_p is a noise term with expected value 0. To estimate v_ξ, we perform a simple linear regression on the time series, with t_p as explanatory variable, giving $\hat{v}_\xi$. The variance of the residuals $\hat{\zeta}_p = \xi_p^{(d)} - \hat{v}_\xi t_p$ will represent the degree of fluctuations of the centers of mass of the school:

$$\hat{v}_\xi = 0.58 \text{ m/s} \quad \text{and} \quad \text{Var}(\hat{\zeta}_p) = 13.2.$$

Figure 8.3 displays $\xi_p^{(d)}$ plotted against the time points for the pings, together with the fitted line $\hat{v}_\xi t_p$. We see that the center of mass of the school does not seem to move along the direction found, for the first 7 pings. It looks as if there are two different states of $\xi_p^{(d)}$. The centers of mass of the school, either found by the accurate way or by the crude way, are sensitive to errors in the segmentation done to identify the voxels that belong to the school, and as we will see in the nest section, there are evidence that there actually are errors in the segmentation of the school in our case. In addition we have not accounted for the sea current in our calculations, so that the transformation from (V) to (G) might contain errors. This is something that needs to be done in future work, but since we did not have the data for the sea current at the particular survey site, we accept the transformation from (V) to (G) in this thesis.

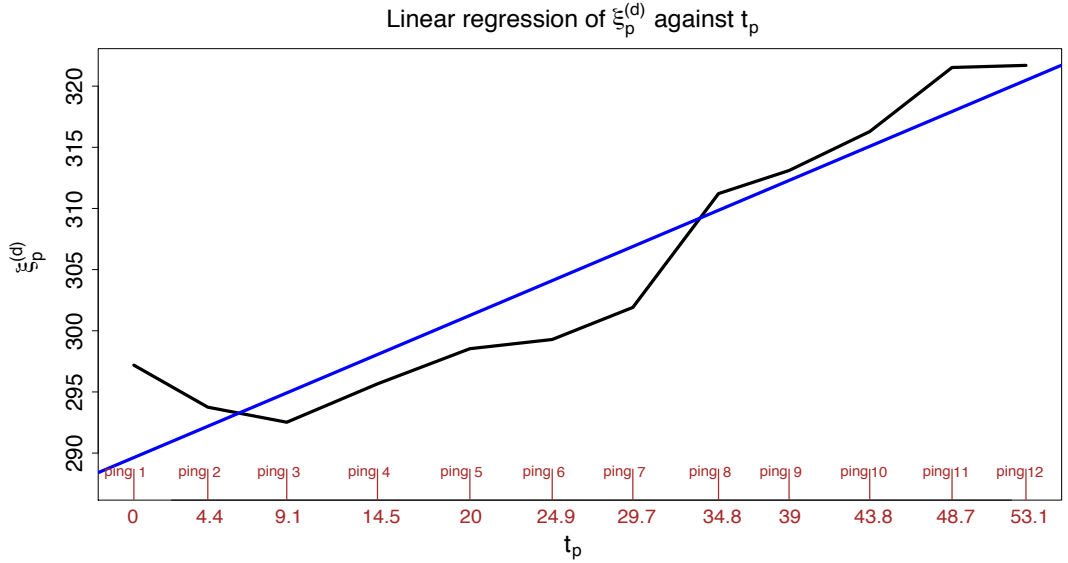

Figure 8.3: Projected centers of mass $\xi_p^{(d)}$ (found by the accurate method), onto the direction extracted from the eigenvector corresponding to the largest eigenvalue of the covariance matrix of ξ. The blue line is the fitted line of (8.1). The values of $\xi_p^{(d)}$ are values on the y-axis of the global coordinate system, rotated by $(\theta_\xi, \phi_\xi)_{\text{acc}}$.

(b) $V_p^{(T)}$ and (c) $\sigma_p^{(T)} = \sum_{M_p} V_{ijk} B_{ijkp}$ and $B_p^{(T)} = \sigma_p^{(T)} / V_p^{(T)}$

An important indication on errors in the segmentation of the school is the total volume $V_p^{(T)}$ of the school at ping p. As seen in Figure 8.4 there is a change in the volume of the school, increasing to more than four times the value at ping $p = 1$. As the 12 pings at which the school is observed span a time interval of length 53.1 seconds, the change in total volume is drastic. There can only be 3 reasons for such a development: (i) Expansion of the school, (ii) other schools of fish joining the school and (iii) of errors in the segmentation. We wish to find out which of these three cases might cause the change in $V_p^{(T)}$.

To decide wether or not (i) might be the case, we need to look at the variables $\sigma_p^{(T)}$ and $B_p^{(T)}$, representing the total amount of bubbles of cross sectional area 1 mm^2, defined in (2.14), and the total density of such bubbles per m^3. These are plotted in Figure 8.5. If expansion

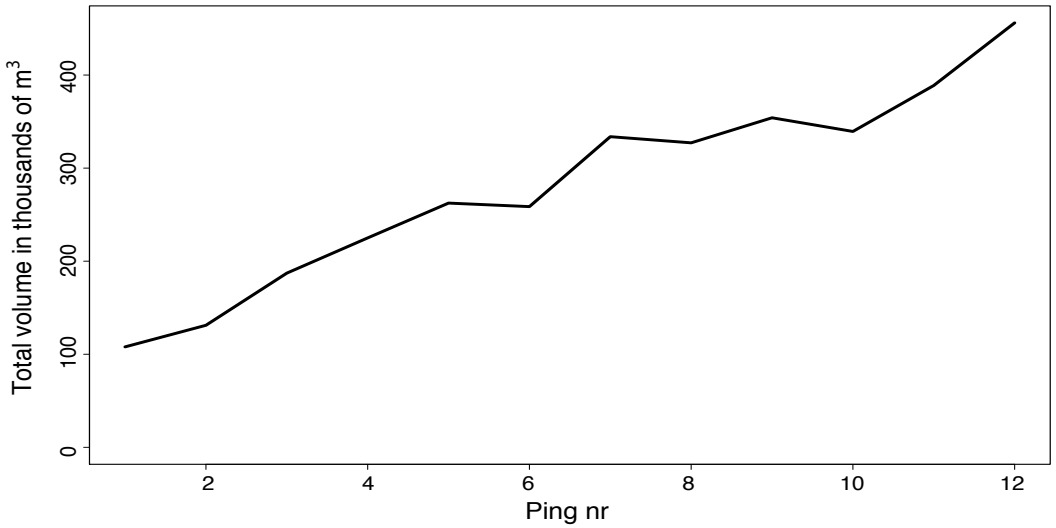

Figure 8.4: Total volume of the school plotted against time, according to the segmentation method presented in (Balabanian et al., 2007).

was the reason for the increasing total volume, we would expect no significant changes in $\sigma_p^{(T)}$, and a reduction in $B_p^{(T)}$ according to the expansion. As seen in Figure 8.5 the total density $B_p^{(T)}$ appears to be unchanged, while the total number of bubbles $\sigma_p^{(T)}$ changes according to the increase in total volume $V_p^{(T)}$. We thus conclude that expansion can not be the reason for the increased total volume of the school.

There is however the possibility that the increase in $\sigma_p^{(T)}$ is caused by the a gradual change in mean orientation angle $\bar{\alpha}^F$ of the fish in the school, causing the mean beam factor to increase, but the probability of such an event must be very small.

We are thus left with the three possibilities (ii), (iii), and a combination of the two. To decide which situation is the most plausible, we perform a visual inspection of the plot in Figure 7.5, which displays the regenerated school presented in section 7.2.3. The figure shows the regenerated school plotted in red, while all other regenerated values are plotted in black. For the first few frames a number of black dots close to or integrated in the red school is seen, indicating that the segmentation procedure have not performed satisfyingly for these

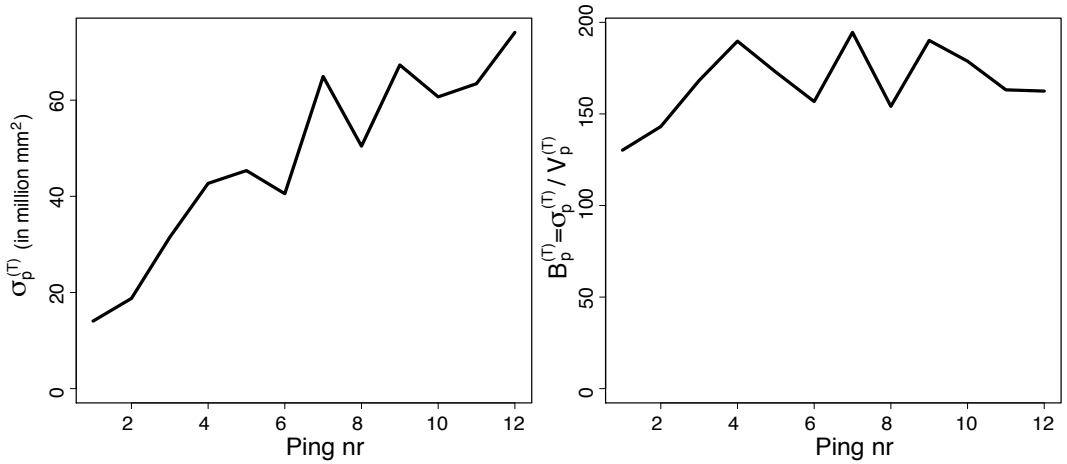

Figure 8.5: **Left:** Total total amount of bubbles of cross sectional area 1 mm^2 of the school plotted against time, according to the segmentation method presented in (Balabanian et al., 2007). **Right:** Total B-value of the school, i.e. number of bubbles of cross sectional area 1 mm^2 per m^3.

pings. For pings number 5 through 10, there seems to be a group of fish joining the school, so that we might believe that both (ii) and (iii) are contribute to the increase in $V_p^{(T)}$.

The mean and variance of $B_p^{(T)}$ for all pings $p = 1, \ldots, P$ can both be used as describing variables. However, since we have detected errors in the segmentation of the school, we do not interpret the variance in $B_p^{(T)}$ (referring to the end of part (c) of section 7.2.1), but only consider the mean. As we do not have information about the calibration of the MS70 sonar, we do not wish to interpret the observed mean, but only present the result as mean$(B^{(T)}) = 167.0$ given as the number of bubbles of cross sectional area 1 mm^2 per m^3.

(d) PCA$_p$

As presented in part (d) of section 7.2.1, we need to project the midpoints onto planes in order to analyze the covariance structure of the school by PCA. We projected the midpoints onto the x-y-plane, the x-z-plane and the y-z-plane, in (S), and calculated the eigenvectors and eigenvalues of the covariance matrices of the projected midpoints in the three planes. The resulting eigenvectors, weighted by the

square root of the corresponding eigenvalues, are plotted in Figure 8.6. An apparent feature in the plot of the eigenvectors from the x-y-plane (left) is that the eigenvalues of the first 6 pings are unstable compared to the eigenvalues of the last 6 pings. In addition the eigenvectors of ping 1 and ping 3 clearly deviates from the rest of the eigenvectors. We propose that this is connected to the change in total backscattering $\sigma_p^{(T)}$ displayed in Figure 8.5. We have before linked this change to a combination of errors in the segmentation of the school and groups of fish joining the school. When calculating the mean of the eigenvectors, to obtain the rotation angles $\bar{\theta}'_o$ and $\bar{\phi}'_o$ of the mean oblongness of the school, presented in (d) of section 7.2.1, we thus only consider the last 6 pings, hoping to minimize the effect of the assumed errors in the segmentation of the school. The mean direction of the oblongness of the school represented in (S) and (G) was found to be:

$$(\bar{\theta}'_o, \bar{\phi}'_o) = (89.0^\circ, 86.0^\circ)$$

and

$$(\bar{\theta}_o, \bar{\phi}_o) = (\theta_\xi, \phi_\xi) + (\bar{\theta}'_o, \bar{\phi}'_o) - (\pi/2, \pi/2) = (-10.2^\circ, 84.9^\circ),$$

where (θ_ξ, ϕ_ξ) was chosen to be the direction found from fitting the closest line to the centers of mass derived in the accurate way.

Using the rotation $(\bar{\theta}'_o, \bar{\phi}'_o) - (\pi/2, \pi/2)$ of the direction of the oblongness of the school with respect to the y-axis of (S), we now define the second coordinate system (S') of the school by the rotation matrix $\mathbb{A}_{\mathrm{S}\to\mathrm{S'}} = \mathbb{A}_{zx}(\bar{\theta}'_o - 90^\circ, \bar{\phi}'_o - 90^\circ) = \mathbb{A}_{zx}(-1.0^\circ, -4.0^\circ)$, according to the notation defined in Appendix A.

In part (d) of section 7.2.1 the roll angle c^s, found from the eigenvectors of the covariance of the midpoints projected onto the x-z-plane, was suggested as a variable possibly describing the state of the school. We calculated the mean $\bar{c}^s$ of this angle for the 6 last pings, as we did for the two other rotation angles $\bar{\theta}_o$ and $\bar{\phi}_o$:

$$\bar{c}^s = 15.2^\circ,$$

where $\bar{c}^s$ is defined as the counter clockwise rotation around the y-axis of (S). Wether or not this angle has significance in the statistical analysis, is left to future work.

The variables length L_S^p, width W_S^p and height H_S^p of the school and the variables C_x^p, C_y^p and C_z^p reflecting the degree of centrality of the school, was defined in part (d) of section 7.2.1 from the ranges of x-, y- and z-values in (S'). We modified ranges of x-, y- and

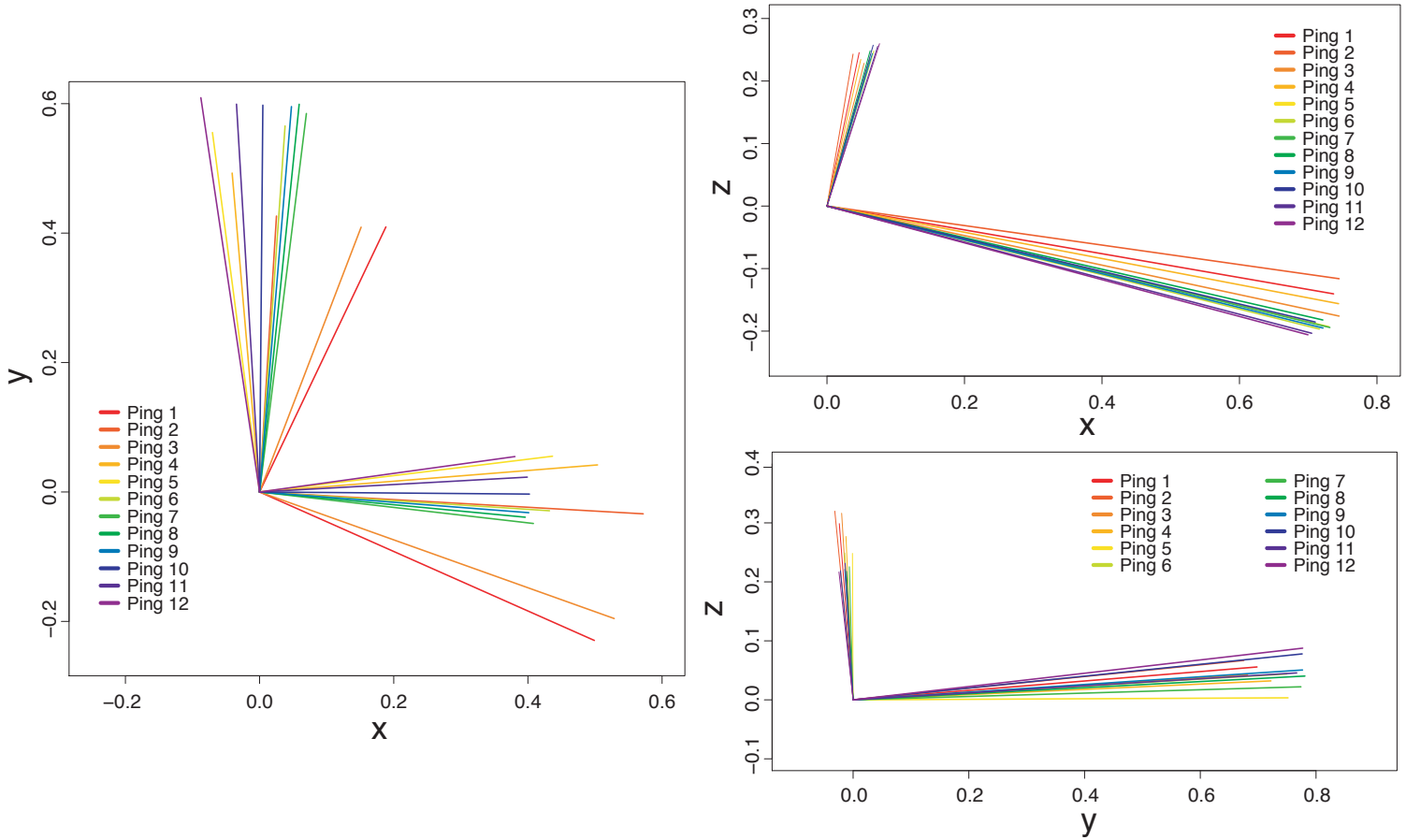

Figure 8.6: Eigenvectors of the midpoints projected onto the x-y-plane, the x-z-plane and the y-z-plane, in (S), with lengths weighted by the square root of the corresponding eigenvalues.

z-values using (7.4) in section 7.2.2 for $c_q = 0$ and $c_q = 0.01$. The results are presented in Figure 8.7. From the left frame we clearly see the difference between the ranges defined from the different values of c_q. The dashed lines are ranges defined by the center 98 % of the total backscattering from the school in the x-, y- and z-direction. If the school had clearly defined outskirts, and if the segmentation of the school was free of errors, we would expect that the two ranges differed by much less than what is seen in Figure 8.7. When analyzing the shape and degrees of centrality of the school, we thus suggest that the modified range specified by $c_q = 0.01$ should be used.

The most striking feature of the plots of the degree of centrality in the x-, y- and z-direction is the large values of C_y^p, implying larger weight in the tail parts of the school than in the front parts. This conflicts with the result that small schools usually have larger weight in the front, documented in (Hemelrijk and Kunz, 2004) and (Bumann et al., 1997). We discuss this further in part $(b)_q$ and $(c)_q$ of section 8.1.

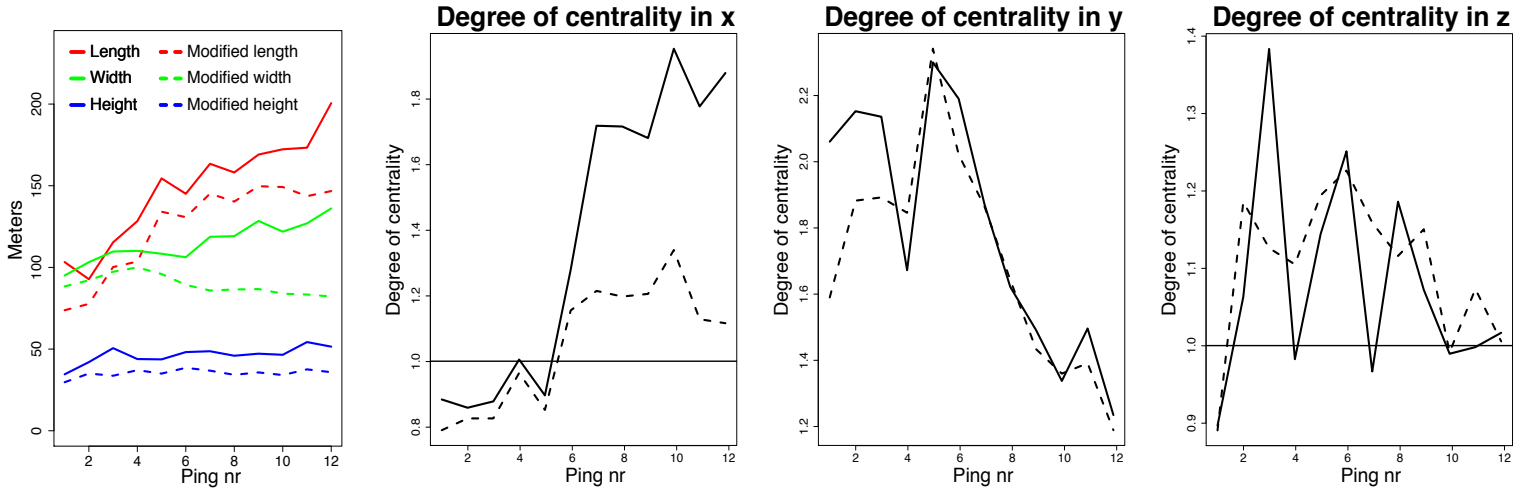

Figure 8.7: Length L_S^p, width W_S^p and height H_S^p of the school and degrees of centrality C_x^p, C_y^p and C_z^p of the school, defined for the full range and the modified range corresponding to $c_q = 0$ and $c_q = 0.01$ in (7.4).

(e) $\bar{B}_p$, $\mathrm{Var}(B)_p$ and $\mathrm{Var}(B)_p/\bar{B}_p^2$

We calculated the squared coefficient of variation of the B-values for each ping $p = 1, \ldots, 12$, and the results are displayed in Figure 8.8. We have that the mean and variance of the squared coefficients of variation for all pings are 4.03 and 0.86. Wether or not these variables

can be used for describing the school is left to future work, but we mark that the mean of the squared coefficients of variation is 4 times higher than what is provided by the exponential distribution of B-values. As explained in section 6.1, the number of fish contributing to the B-values is expected to change as a beam enters and leaves the school. It is thus possible that the value of the mean of the squared coefficients of variation of B-values found for the school in this thesis, can be explained by these effects.

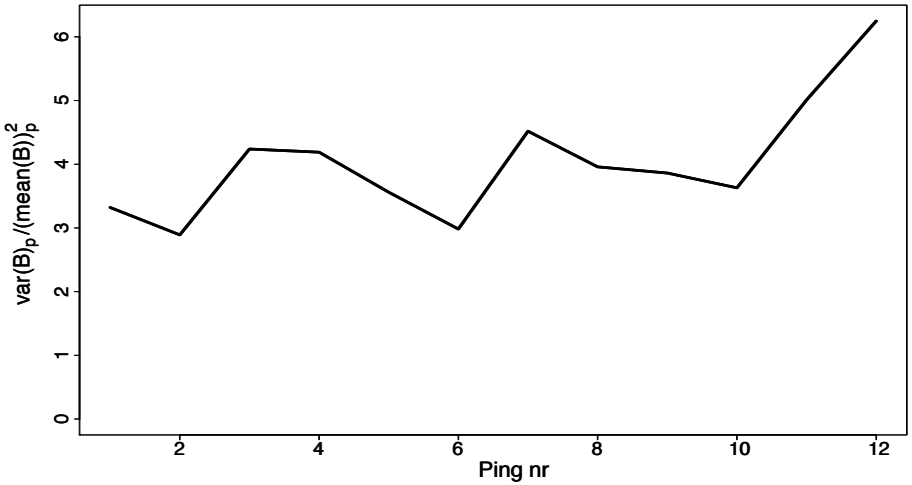

Figure 8.8: Squared coefficient of variation $\mathrm{Var}(B)_p/\bar{B}_p^2$ of B-values identified as belonging to the school, for each ping $p = 1, \ldots, 12$.

(f) $\hat{\rho}^{(T)}(h)$

The mean autocorrelation $\hat{\rho}^{(T)}(h)$ for lags $h = 0, \ldots, 20$ of sequences of lengths larger than 40 along beams identified as belonging to the school treated in this thesis, have already been presented in part (f) of section 7.2.1. The result is displayed in Figure 7.2. Comparing $\hat{\rho}^{(T)}(h)$ from several observed fish schools of different species is needed to evaluate the significance in this variable.

8.2 Results for parts of the school.

Using the modified ranges of x-, y- and z-values defined according to (7.4) for $c_q = 0.01$, we define the 7 parts to be considered in this section, q =(LS),(RS),(T),(M),(F),(L),(U), as explained in section 7.2.2. Figure 8.9 shows the modified ranges of $c_q = 0.01$ compared to the original ranges corresponding to $c_q = 0$. We see that there is a rather significant difference between the two types of ranges, and for the last ping the range in x when $c_q = 0.01$ is only 60 % as wide as the full range. This justifies the use of the modified range, rather than the full range.

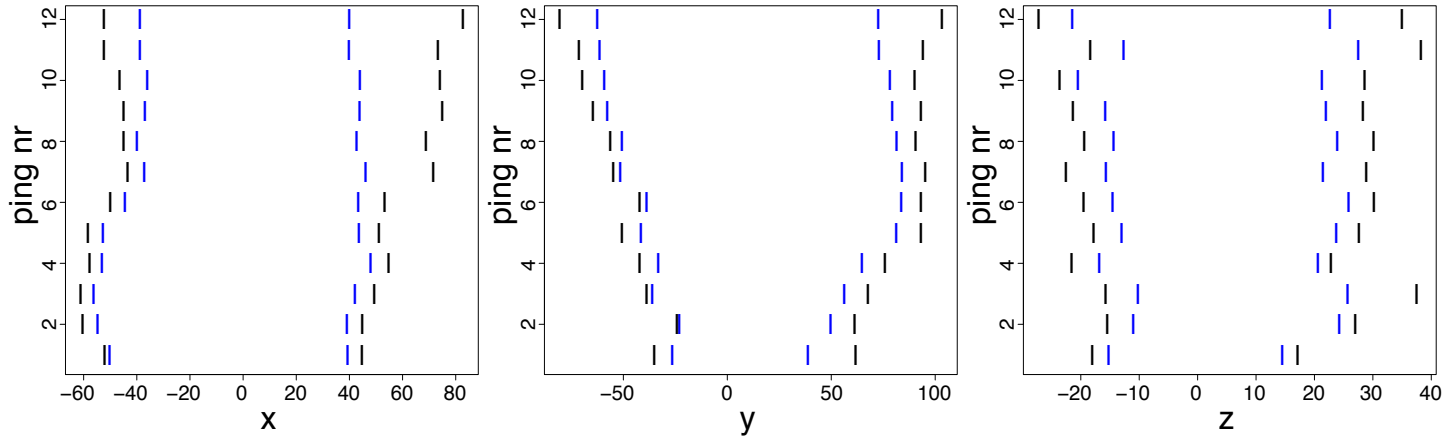

Figure 8.9: Modified ranges of x-, y- and z-values (blue) compared to the original ranges of x-, y- and z-values (black) in the coordinate system (S') of the school.

$\mathbf{(b)}_q$ $V_{p,q}^{(T)}$ and $\mathbf{(c)}_q$ $\sigma_{p,q}^{(T)} = \sum_{M_{p,q}} V_{ijk} B_{ijkp}$ and $B_{p,q}^{(T)} = \sigma_p^{(T)} / V_{p,q}^{(T)}$

We present the results for the 3 ratios between the parts (U) and (L), (F) and (T), and (M) and the sum (T)+(F), for the three variables $V_{p,q}^{(T)}$, $\sigma_{p,q}^{(T)}$ and $B_{p,q}^{(T)}$, as suggested in part $(b)_q$ and part $(c)_q$ in section 7.2.2. All 9 ratios for the 12 pings at which the school is observed, are displayed in Figure 8.10. As shown in section 8.1, there is reason to believe that the segmentation of the school used in this thesis contains errors, and that the last 6 pings are the most reliable. We thus focus on the pings 7 through 12 when analyzing Figure 8.10.

The 3 ratios concerning total volume $V_{p,q}^{(T)}$ of the different parts, primarily reflect the shape of the school, and not necessary the number of fish in those parts. The 3 ratios concerning total backscattering $\sigma_{p,q}^{(T)}$ might reflect the number of fish in the parts, but differences in mean orientation of the fish in the different parts may affect the total backscattering to a large degree. Similarly the 3 ratios of $B_{p,q}^{(T)}$ intuitively reflect the fish density, but differences in mean orientation of the fish may affect these ratios too. As the orientation structure of the school is unknown at this point, we will in the following interpret results as reflecting the number of fish in different parts, bearing in mind that this may be a wrong assumption.

We consider the ratios of upper half (U) to lower half (L) for the three variables first. From Figure 8.10 we see that based on the modified ranges defined in the beginning of section 7.2.2, the upper half of the school seems to be larger and containing more fish than the lower half. The fish density also seems to be slightly lower in the upper half than in the lower. Wether these observations are properties of the particular school, or results of errors in the segmentation of the school, or simply results of random changes in the school, is undecided until more schools have been analyzed.

The ratios of front and tail of the school, defined by the first and the last quarters of the modified ranges of y-values, are interesting in comparison to the findings of (Hemelrijk and Kunz, 2004) and (Bumann et al., 1997), where groups of fish are documented through simulations and observations to have higher density in the front part than in the tail part. This result however, was registered for schools of 100 (Hemelrijk and Kunz, 2004) and 9 (Bumann et al., 1997) fish, which are very small schools compared to the school treated in this thesis. We propose that if the same pattern is to be found in our results, it would translate to larger total backscattering in the front part compared to the tail part. The variable $\sigma_{p,q}^{(T)}$ will be less sensitive to errors in the segmentation, because if voxels are wrongly identified as belonging to the school, these will normally have low B-values, thus contributing little the total backscattering.

Considering Figure 8.10 we obsesrve that the contrary of the findings of (Hemelrijk and Kunz, 2004) and (Bumann et al., 1997) seems to be the case. Both $B_{p,q}^{(T)}$ and $\sigma_{p,q}^{(T)}$ is lower than 1 for all 12 pings. We can however not be certain that the number of fish is larger in the tail part of the school than in the front part. As mentioned in section 7.1.3 there might be a current in the sea, which has not been accounted for in our calculations. Combined with the possible errors in the segmentation of the school, this opens for the possibility that the school actually moves *opposite* the direction of the centers of mass, found in part (a) of section 8.1. In that case the results in Figure 8.10 for the ratio (F) to (T) would be in consistency with (Hemelrijk and Kunz, 2004) and (Bumann et al., 1997).

We wish to examine the front end and the tail end of the school, assuming that the movement of the school may be detected by the position of these points. In the same way that the rotation from (S) to (S') was done in part (d) of section 8.1, we rotate the midpoints from (G) to a coordinate system having horizontal x-axis, and y-axis in the direction of the school, found from PCA of the midpoints projected onto the x-y-plane and the y-z-plane of (G). We then modify the ranges in x-, y- and z-direction by the procedure presented in section 7.2.2. The middle frame of Figure 8.11 shows that the blue points to the left of the plot, which represent the rare end of the school as identified by the movement of ξ, actually moves slightly backwards when considering all 12 pings, but shows no apparent movement for the last 6 pings. The front end moves up to 60 meters forwards during the first 7 pings, but shows no apparent movement

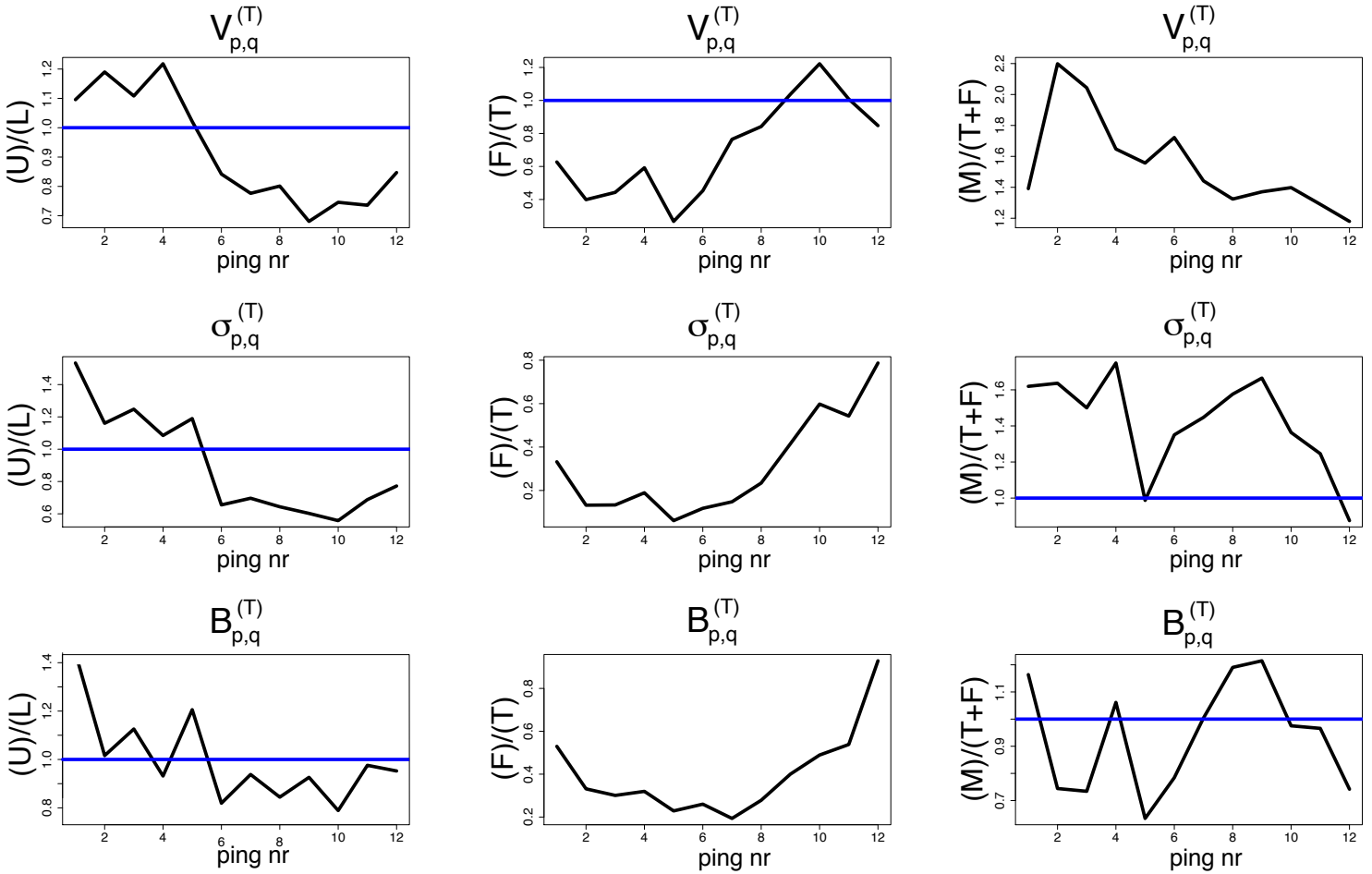

Figure 8.10: Ratios between the upper half (U) and the lower half (L), the front (F) and the tail (T), and the middle part (M) and the sum of the tail and the front (T)+(F) of the school, for the three variables $V_{p,q}^{(T)}$, $\sigma_{p,q}^{(T)}$ and $B_{p,q}^{(T)}$.

during the last 5 pings. In section 8.1 we observed by studying Figure 7.5, that there appears to be a group of fish joining the school at the front end (as defined by the movement of ξ). We thus rely mainly on the lower ranges of y-values, as seen in the middle frame of Figure 8.11. Since we concentrate on the last 6 pings, we actually have no evidence that the school moves at all based on the tail end and the front end. If any such assumption of the movement of the school should be made, it must be that it moves opposite the direction found by the centers of mass, thus corresponding to the findings of (Hemelrijk and Kunz, 2004) and (Bumann et al., 1997).

The above argument shows the danger of analyzing the centers of mass and other variables that are sensitive to errors in the segmentation of the school. If the assumption of oblongness in the direction of the school (Pitcher, 1980) can be made generally without high risk of errors, PCA of the projected midpoints onto the x-y-plane and the y-z-plane of (G), combined with an analysis of the two ends of the school in this direction, might give us the safest estimate of the direction of the school. In the rest of the thesis, we will however use the directions found from ξ, and adjusted for the oblongness of the projected midpoints, defining (S) and (S').

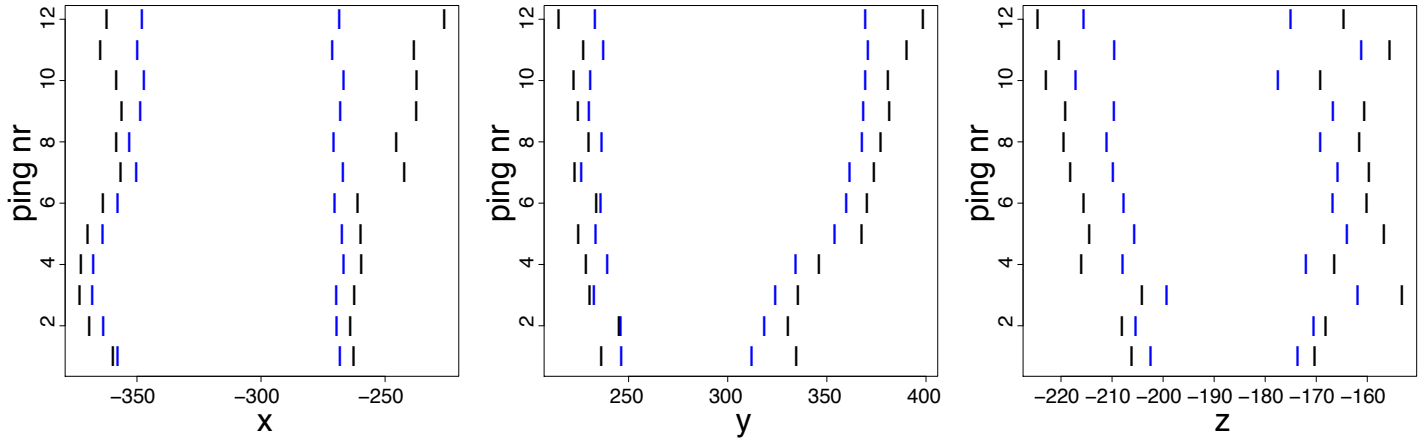

Figure 8.11: Modified ranges of x-, y- and z-values (blue) compared to the original ranges of x-, y- and z-values (black) in the global coordinate system rotated by the direction of the school found from PCA of the midpoints projected onto the x-y-plane and the y-z-plane of (G).

$(\mathbf{d})_q$ $\mathrm{PCA}_{p,q}$

We only visually analyze the eigenvectors of the covariance matrix of the projected midpoints in the 7 parts presented in section 7.2.2. The projections are made onto the y-z-plane, for the parts (RS) and (LS), the x-z-plane, for the parts (T), (M) and (F), and the x-y-plane, for the parts (L) and (U). The resulting eigenvectors with lengths according to the square root of the corresponding eigenvalues, are plotted in Figure 8.12. There are two apparent features of the plots. Firstly, in the left frame we observe that the upper and the lower part, represented by the green and the red lines, have generally different directions. Secondly we observe that the front part seems to have larger tilt angle than the tail part and the middle part. We do not propose any explanation on the first feature, but the second might be linked to the errors in the segmentation and the group of fish joining the school at the front. Wether PCA of parts of the school is useful for describing the properties of the school, is left to future analysis.

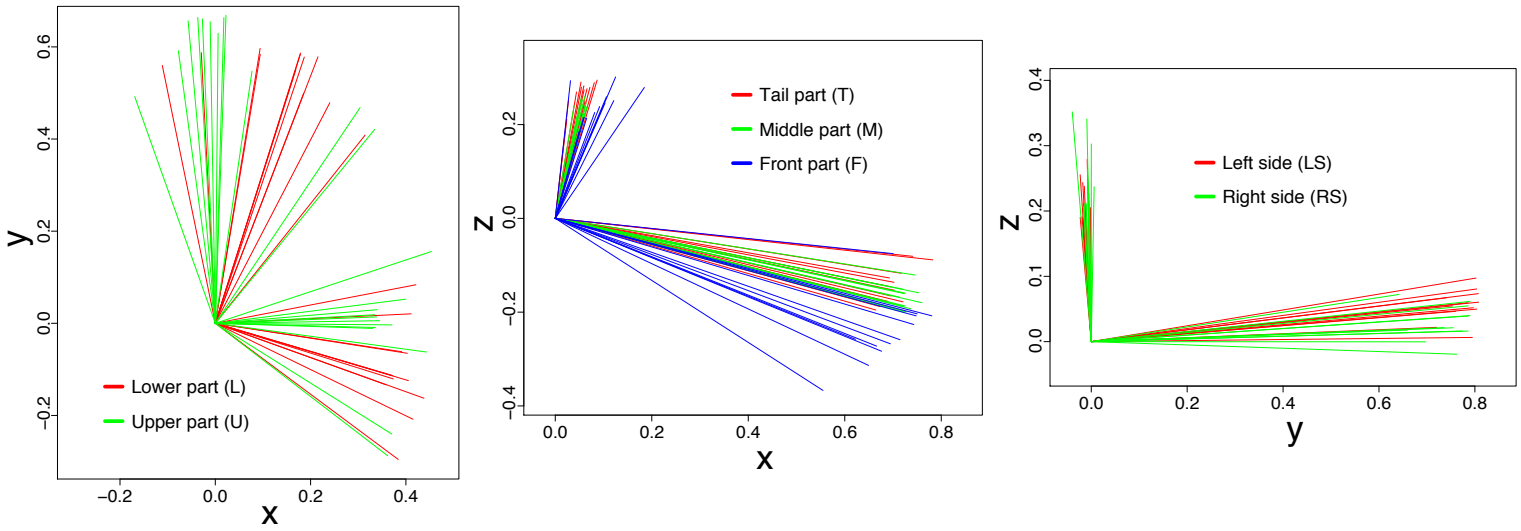

Figure 8.12: Eigenvectors of the midpoints in the 7 parts (RS), (LS), (T), (M), (F), (L) and (U) of the school, projected onto the x-y-plane, the x-z-plane and the y-z-plane, in (S). Lengths of the eigenvectors are weighted by the square root of the corresponding eigenvalues.

8.3 Regeneration of the school.

Plots of regenerated fish positions for the school treated in this thesis was presented in section 7.2.3. From the regenerated school we calculate the eigenvectors and the eigenvalues of the covariance matrix of regenerated positions identified as belonging to the school. As we have established so far, the last 6 pings are the most reliable because of the probable errors in the segmentation of the school. We thus average the eigenvectors corresponding to the largest eigenvalues for the last 6 pings when estimating the direction of the oblongness of the school, defining (S"). We name the directions for each ping (θ_o^p, ϕ_o^p), while the direction found from averaging the last 6 pings will be named $(\bar{\theta}_o, \bar{\phi}_o)$, both referring to the oblongness. The individual directions and the total direction are listed next:

Ping nr	1	2	3	4	5	6	7	8	9	10	11	12
$\theta_o^{(p)}$	-13.2°	1.2°	-19.3°	-18.4°	9.3°	-21.3°	-17.1°	-12.9°	-10.1°	-10.0°	-12.3°	-6.8°
ϕ_o^p	84.7°	80.6°	86.4°	85.6°	84.4°	85.6°	86.8°	86.0°	83.9°	81.7°	85.1°	80.9°

Direction found from three dimensional PCA of the last 6 pings: $(\bar{\theta}_o, \bar{\phi}_o) = (-12.8°, 84.8°)$

Comparing to the direction found from fitting the closest line to the centers of mass ξ, $(\theta_\xi, \phi_\xi)_{\text{acc}} = (-9.2°, 88.9°)$, we see that the difference is no more than 4°. The variation in θ_o^p is quite large compared to the difference between θ_o^p and θ_ξ, while ϕ_ξ seems to be significantly different from ϕ_o^p. The comparison between the directions found from the movement of the centers of mass, and PCA of the projected midpoints or the regenerated fish positions, might be useful for the description of the school. The determination of the school, defined in part (d) of section 7.2.1 to be the desire of the school to move in a defined direction, might be reflected by the difference between $(\bar{\theta}_o, \bar{\phi}_o)$ and (θ_ξ, ϕ_ξ). In our case the determination appears to be high, but the possible errors in the centers of mass prohibit us to relying on this conclusion.

In section 7.2.3 we presented the concept of counting the number N_p^S of regenerated fish positions at ping p, in a sphere completely contained in the school. We considered three such spheres of radius 5 meters, centered at the positions $\xi_{12} + (-10, 0, 0)$, ξ_{12} and $\xi_{12} + (10, 0, 0)$, and three spheres of radius 10 meters, centered at the positions $\xi_{12} + (-20, 0, 0)$, ξ_{12} and $\xi_{12} + (20, 0, 0)$. We have here assumed that the school does not move significantly during the 12 pings at which it is observed, inspired by the discussion in part $(b)_q$ and $(c)_q$ of section 8.1. The use of ξ_{12} is because the errors in the segmentation appears to decrease with the number of the pings. The resulting number of regenerated fish positions are plotted in Figure 8.13.

Comparing with the expected variation in N_p^S found in section 7.2.3, we observe that the fluctuations displayed in Figure 8.13 are to

large to be explained by random fluctuations. Changes are specially large between the last 6 pings, and for the spheres of radius 5 meters, the changes between pings sometimes exceed 100%, which compared to the 95% confidence interval of (70%,130%) is quite significant. We thus conclude that there are changes between consecutive pings, in the total acoustic backscattering from the spheres of radius 5 meters. Since the time difference between pings are on average 5 seconds, the changes in acoustic backscattering are rapid and can only be explained by changes in mean orientation of the fish in the spheres. This is an important result, as it reflects the *local* behaviour of the fish in the school. As opposed to many other variables discussed in this chapter, the number of regenerated fish positions in segments of the school that are completely enclosed in the school, will be largely unaffected by errors in the segmentation of the school.

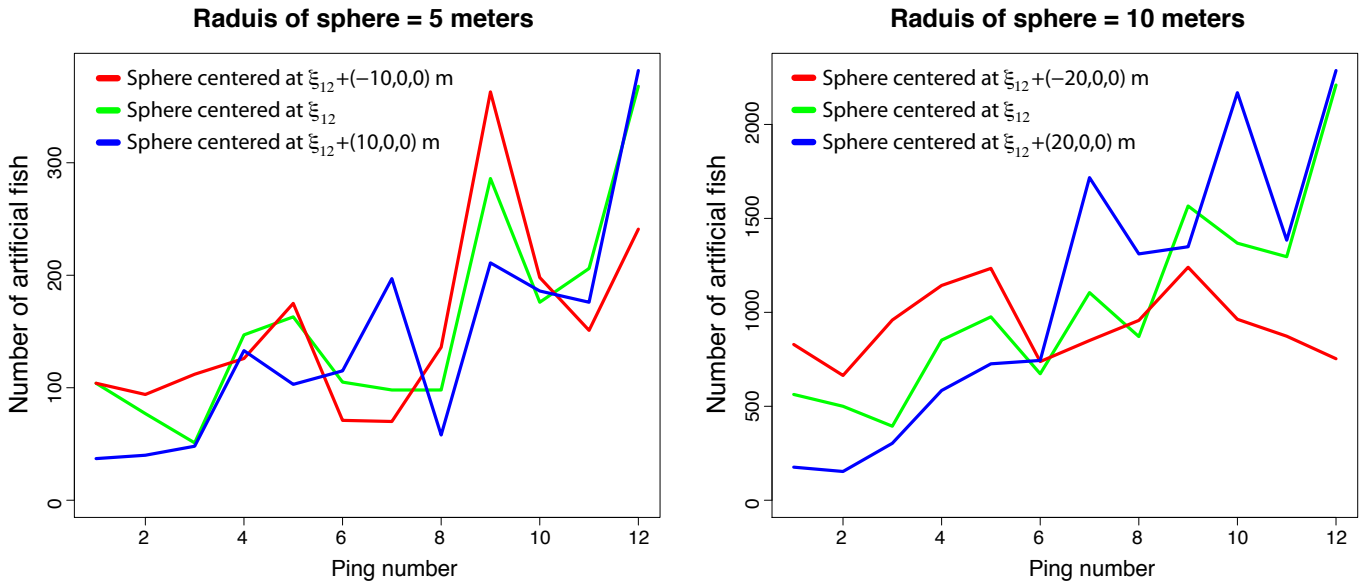

Figure 8.13: Number of artificial fish positions in spheres of radius 5 and 10 meters for the left and the right plot respectively. The three lines represent three neighbouring spheres around the center of mass of the school.

Chapter 9

Discussion and future work.

In chapters 7 and 8 we found variables that may describe the properties of the school. We will in this chapter list the most important of these variables, and identify those that are sensitive to errors in the segmentation of the school. We also present problems that might occur in the statistical analysis, based on the our own experiences, and suggest subjects for future analysis. In the statistical analysis, 5 coordinate systems have been introduced, where 3 of them are versions of the coordinate system of the school. We firstly present an overview of the definitions of these 5 coordinate systems.

(G) The global coordinate system, defined as having the x-y-plane on the surface of the sea, with y-axis in the direction North, and with origin at the first position of the vessel in the geographic coordinate system of the Earth.

(V) Coordinate system of the vessel, defined by horizontal x-axis, with y-axis in the direction of the vessel, and with origin at the position of the vessel in the x-y-plane of (G) for each ping p.

(S) Coordinate system of the school, defined by horizontal x-axis, with y-axis in the direction of the school defined by the movement of the centers of mass, and with origin at the center of mass of the school at each ping p.

(S') Coordinate system of the school, defined by horizontal x-axis, with y-axis in the direction of the school defined by PCA of the midpoints of voxels identified as belonging to the school, projected onto the x-y-plane and the y-z-plane, and with origin at the center of mass of the school at each ping p.

(S") Coordinate system of the school, defined by horizontal x-axis, with y-axis in the direction of the school defined by PCA of the regenerated school presented in section 7.2.3, and with origin at the center of mass of the school at each ping p.

While (S) is based on the motion of the centers of mass, which for a synchronized school represents the motion of the school, the two other coordinate systems (S') and (S") are based on the direction of the oblongness of the school, as detected by PCA. Because of the errors in the segmentation of the school, we primarily used (S') in the statistical analysis, but for the particular school treated in this thesis there vas only a minor deviation between (S) and (S'). The most accurate direction of the oblongness of the school is however provided by PCA of the regenerated fish positions, defining (S"). The regenerated school is an inviting way of representing the data set, but demands some time consuming computer processing.

Variables for describing schools.

We now present the variables that we consider to the be most important, labeling them by the degrees 0, 1 and 2 of the sensibility to errors in the segmentation of the school, representing "no sensitivity", "some sensitivity" and "crucial sensitivity":

Symbol	**Description**	**Sensitivity**
ξ_p	Centers of mass of the school at ping p.	2
Z_p	Depth of the school represented by the z-component of ξ_p	0
(θ_ξ, ϕ_ξ)	Direction of the school based on the motion of ξ_p	2
$\lambda_1^\xi/\lambda_2^\xi$	Ratio of the first two eigenvalues of ξ_p	2
$\hat{v}_\xi$	Speed of the school estimated from the centers of mass ξ_p projected onto the direction (θ_ξ, ϕ_ξ)	2
$\mathrm{Var}(\hat{Z}_p)$	Variance in the centers of mass ξ_p projected onto (θ_ξ, ϕ_ξ)	2
$V_p^{(T)}$	Total volume of the school at ping p. Mean and variance are both interesting.	2
$\sigma_p^{(T)}$	Total acoustic backscattering of the school at ping p. Mean and variance are both interesting.	1
$B_p^{(T)}$	Total B-value of the school at ping p. Mean and variance are both interesting.	2
$(\bar{\theta}_o, \bar{\phi}_o)$	Direction of oblongness of the school based on PCA .	1
$(\bar{\theta}_o, \bar{\phi}_o) - (\theta_\xi, \phi_\xi)$	Difference between directions based on ξ and on PCA, reflecting the determination of the school.	2
$\bar{c}^s$	Mean roll angle of the school.	1
L_S^p, W_S^p and H_S^p	Length, width and height of the school at ping p, found for the range specified by the range parameter c_q defined in section 7.2.2.	1

Symbol	Description	Sensitivity
C_x^p, C_y^p and C_z^p	Degrees of centrality of the school in x-, y- and z-direction.	1
$\mathrm{Var}(B)_p/\bar{B}_p^2$	Squared coefficients of variation of B-values at each ping p.	1
$\hat{\rho}^{(T)}(h)$	Mean empirical autocorrelations of sequences of length>40 along beams, for lags $h = 1, \ldots, 20$.	1
$V_{p,q}^{(T)}$	Total volume of part q of the school at ping p. Ratios of upper part (U) to lower part (L), front part (F) to tail part (T) and middle part (M) to the sum (T)+(F) are especially interesting.	2
$\sigma_{p,q}^{(T)}$	Total acoustical backscattering of part q of the school at ping p. Ratios of upper part (U) to lower part (L), front part (F) to tail part (T) and middle part (M) to the sum (T)+(F) are especially interesting.	1
$B_{p,q}^{(T)}$	Total B-value of part q of the school at ping p. Ratios of upper part (U) to lower part (L), front part (F) to tail part (T) and middle part (M) to the sum (T)+(F) are especially interesting.	2
N_p^S	Number of artificial fish positions in a segment enclosed in the school at ping p. Variance is especially interesting.	0

The variables that are classified with "crucial sensitivity" (sensitivity= 2), are the variables linked to the x- and y-value of the centers of mass ξ_p, and the variables linked to the total volume of the whole school or parts of the school. In part $(b)_q$ and $(c)_q$ of section 8.1, we provided indications on the possibility that the school actually moves in the opposite direction of the centers of mass, which qualifies for labeling all variables linked to ξ_p as sensitivity 2-variables. In section 8.1 we also showed that the ranges when considering only the center 98 % of the backscattering of the school in the x-, y- and z-direction, are reduced drastically. We thus believe that the effect on the variables related to the volume of the school or parts of the school, from errors in the segmentation, qualifies for a sensitivity 2-labelling. However, the depth of the school, represented by the z-component of ξ_p, was shown in part (a) of section 8.1 to have small variance, so that we may consider this variable unaffected by errors in the segmentation of the school.

Variables classified as having "some sensitivity" (sensitivity= 1) are the ones that may or may not have been affected by errors in the segmentation of the school. If the errors are that too many voxels have been identified as belonging to the school, this will not affect the total backscattering represented by $\sigma_p^{(T)}$ and $\sigma_{p,q}^{(T)}$ to a large degree, as voxels outside of the school are characterized by low B-values. The direction $(\bar{\theta}_o, \bar{\phi}_o)$ of the oblongness of the school can be found by three dimensional PCA of the regenerated school, which accounts for the low B-values of voxels that are wrongly identified as belonging to the school, thus being less sensitive to errors in the segmentation. The same holds for the mean roll angle $\bar{c}^s$. By defining the ranges of x-, y- and z-values according to (7.4), for instance with $c_q = 0.01$

as used in chapter 8, we also avoid accounting for voxels that are wrongly identified as belonging to the school, so that the variables L_S^p, W_S^p, H_S^p, C_x^P, C_y^P and C_z^P are less sensitive to the errors in the segmentation. The squared coefficient of variation in the B-values does not show any significant change from the first 6 ping to the last 6 pings, as other variables like the $V_p^{(T)}$ do, so we assume that the effect on $\mathrm{Var}(B)_p/\bar{B}_p^2$ of errors in the segmentation is limited to "some sensitivity". Finally, the mean autocorrelation of sequences along voxels might not change if only a part of the school is identified in the segmentation.

Analyzing these variables for many schools of known or unknown species is needed to establish which of the variables, if any, that can be used to identifying the species.

Future analysis.

The problems encountered in the statistical analysis, linked to the errors in the segmentation of the school, show the importance of a segmentation procedure that is as robust and accurate as possible. From a statistical point of view, the flood-fill algorithm presented in (Balabanian et al., 2007), and used in this thesis, might be too crude. Developing an algorithm based on statistical theory, with the ability to detect errors in the segmentation, should be one of the key subjects for future analysis. All the variables labeled sensitivity$= 2$ are not to be trusted completely, until such a robust segmentation exists.

However, there is a possibility that the errors in the segmentation of the school can be partially blamed on the instrument itself. In Figure 7.5 the regenerated school is plotted together with regenerated positions not identified as belonging to the school. Retracing the school from ping 12 backwards to ping 5, there seems to be a fading of the right third of the school, also when assuming that the black dots at the right end of the school actually belong to the school. Such a fading is hard to explain, and might possibly be linked to errors in the data from the instrument. The particular survey treated in this thesis was done using a pulse duration $\tau_p = 5.12 \cdot 10^{-4}$ s, which is outside the recommended range of pulse durations given in (AS, 2006) to be $(2 \cdot 10^{-3}, 10^{-2})$ s. There is thus reason to believe that the data treated in this thesis actually are not trustworthy.

The MS70 sonar provide a resolution in acoustic school data that is high enough to possibly allow for the detection of local properties of the school. Examining the time development of segments of the regenerated school, is a tool that may prove to be useful when analyzing local changes. Sudden local fluctuations in the acoustical backscattering can only be explained by changes in mean orientation, which gives information to the behaviour of individual fish in the given segment. In section 8.3 we saw that sudden local changes actually do occur, to a degree that cannot be explained by natural random changes. An overall goal in fisheries acoustics is to link the individual behaviour rules in IBMs to group level features of schools, or even populations. The analysis of data from the MS70 multibeam sonar might be a step towards this goal.

Appendix A

Rotation matrices.

Transformation of a point vector $\mathbf{v}$ from a cartesian coordinate system C to another cartesian coordinate system C', rotated around the mutual origin of C and C' can be done by multiplying $\mathbf{v}$ by an orthogonal rotation matrix $\mathbb{A}$:

$$\mathbf{v}' = \mathbb{A}\mathbf{v}, \qquad \mathbb{A}^T\mathbb{A} = \mathbb{I}.$$

If C' is rotated by an angle γ around the x-axis, we call the rotation matrix $\mathbb{A}_x(\gamma)$, and a similarly for y- and z-rotations:

$$\mathbb{A}_x(\gamma) = \begin{bmatrix} 1 & 0 & 0 \\ 0 & \cos\gamma & \sin\gamma \\ 0 & -\sin\gamma & \cos\gamma \end{bmatrix}$$

$$\mathbb{A}_y(\gamma) = \begin{bmatrix} \cos\gamma & 0 & -\sin\gamma \\ 0 & 1 & 0 \\ \sin\gamma & 0 & \cos\gamma \end{bmatrix}$$

$$\mathbb{A}_z(\gamma) = \begin{bmatrix} \cos\gamma & \sin\gamma & 0 \\ -\sin\gamma & \cos\gamma & 0 \\ 0 & 0 & 1 \end{bmatrix}$$

A combination of rotations is done by multiplying single rotation matrices from right to left. For instance, we write a z-x-y-rotation by the angles a, b and c as

$$\mathbb{A}_{zxy}(a,b,c) = \mathbb{A}_y(c)\mathbb{A}_x(b)\mathbb{A}_z(a).$$

An example of a z-x-y-rotation is shown in Figure A.1.

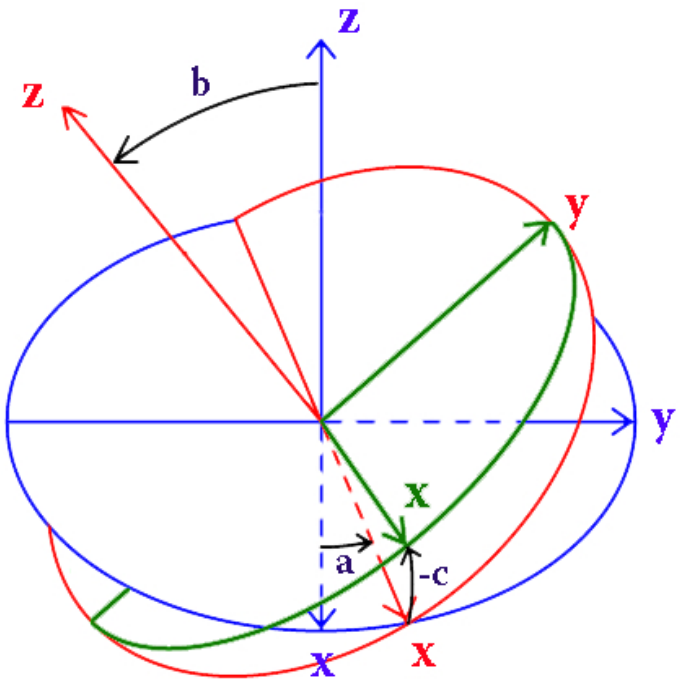

Figure A.1: Euler rotation (a, b, c) of the coordinate system of the fish with respect to the vessel.

Using the orthogonality of the rotation matrices, we can reverse the rotation of a point vector $\mathbf{v}$ given by

$$\mathbf{v}' = \mathbb{A}_{zxy}(a, b, c)\mathbf{v}.$$

We first solve for $\mathbf{v}$:

$$\mathbf{v} = \mathbb{A}_{zxy}^{-1}(a, b, c)\mathbf{v}',$$

and then use the orthogonality to obtain

$$\mathbf{v} = \left[\mathbb{A}_y(c)\mathbb{A}_x(b)\mathbb{A}_z(a)\right]^T \mathbf{v}' = \mathbb{A}_z^{-1}(a)\mathbb{A}_x^{-1}(b)\mathbb{A}_y^{-1}(c)\mathbf{v}' = \mathbb{A}_z(-a)\mathbb{A}_x(-b)\mathbb{A}_y(-c)\mathbf{v}' = \mathbb{A}_{yxz}(-c, -b, -a)\mathbf{v}'.$$

A reversed rotation is thus a rotation in the reversed order by the inverse angles:

$$\mathbb{A}_{zxy}^{-1}(a, b, c) = \mathbb{A}_{yxz}(-c, -b, -a). \tag{A.1}$$

Appendix B

Notation.

This appendix contains a full list of the variables used in the thesis, devinded into the chapters in which they appear. Variables that are defined in previous chapters but important enough to be restated, are written in grey. Vectors are written in bold face, and matrices are written in blackboard bold face. Throughout the thesis ˆ(hat) is used to denote estimates.

Chapter 1, Introduction.

Variable	Description
L_S	Length of schools observed by (Gerlotto et al., 1999).
W_S	Width of schools observed by (Gerlotto et al., 1999).
H_S	Height of schools observed by (Gerlotto et al., 1999).

Chapter 2, Relevant acoustics.

Variable	**Description**
$\mathbf{X} = (x, y, z)$	Position in space.
r	Distance from the source.
$p(\mathbf{X}, t)$	Pressure as a function of space and time.
P	Pressure amplitude.

Variable	Description
A	Pressure amplitude for a plane wave.
f	Frequency of the sound.
ω	Angular frequency of the sound.
λ	Wavelength of the sound.
c	Speed of sound.
T	Period of the wave.
k	Wave number of the sound.
z	Acoustic Impedance.
u	Particle speed.
U_0	Particle speed amplitude.
ρ_0	Equilibrium density of the radiation medium.
ϕ_r	Argument to complex acoustic impedance for a spherical wave. Subscript referring to the distance r.
I	Acoustic intensity.
F	Force in mechanics.
a	Radius of a simple source, a cylindrical source or a circular piston.
ϕ_a	Argument to complex acoustic impedance for a spherical wave evaluated at $r = a$.
$\kappa_a = \cos\phi_a e^{-i(ka+\phi_a)}$	Constant involving the complex acoustic impedance.
Q	Source strength.
$\mathbf{n}$	Unit normal vector of the surface of the source.
L	Length of the line source.
γ	Incident angle to the line source or the circular piston.
$P_{\mathrm{ax}}(r)$	Axial pressure from a line source or a circular piston.
$H(\gamma)$	Directional factor from a line source or a circular piston.
$I(r,\gamma)$	Acoustic intensity from the line source/circular piston.
$I_{\mathrm{ax}}(r)$	Axial acoustic intensity, i.e. acoustic intensity for $\gamma = 0$.
$B(\gamma)$	Directional factor for the acoustic intensity.
$j_0(x)$	Zeroth order spherical Bessel function of the first kind.
J_1	First order Bessel function.
c_a	Absorption constant for acoustic pressure.
$k_{complex} = k + ic_a$	Complex wave number.
$\alpha = 2c_a/\ln 10 \approx 0.87c_a$	Absorption constant for acoustic intensity.
$c(T_W, S_W, P_W)$	Speed of sound in sea water as a function of temperature T_W, salinity S_W and hydrostatic pressure P_W of the sea.

Variable	**Description**
g	Gravitational acceleration in Norway.
$c(z) = \eta z$	Linear approximation of the depth dependency of speed of sound, with slope η.
$I_S(r', \theta', \phi')$	Acoustic intensity from an object in the direction (θ', ϕ') at the distance r' from the source.
$I_T(r)$	Acoustic intensity from the trasducer, striking an object at the distance r.
$\big(I_S(r' = 1)\big)_{\text{ax}}$	Axial acoustic intensity ($\gamma' = 0$) from the source at the distance $r' = 1$.
$B_S(\theta', \phi')$	Directional factor for the acoustic intensity from the source.
$\sigma(\theta', \phi')$	Differential scattering cross section in m^2.
σ_0	Optimal scattering cross section in m^2.
$\sigma_{sp} = \sigma(\theta'_R, \phi'_R)$	Spherical backscattering cross section in m^2.
(θ'_R, ϕ'_R)	Angles in the direction of the receiver.
$TS = 10\log(\sigma_{sp}/4\pi)$	Target strength of an object.
$A_s(\theta', \phi')$	The cross sectional area of the scattering sphere replacing the object.
$\Pi_s = I_T A_s(\theta', \phi')$	The acoustic power scattered by the simple source.
V	A volume from which backscattering is measured.
S_v	Logarithmic density of backscattering cross section in the volume V.
b	Cross sectional area of small bubbles of air representing the backscattering ability in a volume.
N	Number of bubbles of cross sectional area b in the volume V.
$B \equiv N/V = 4\pi/b \cdot 10^{S_v/10}$	Linear S_v-values or density of bubbles of size b.

Chapter 3, Materials.

Variable	Description
x, y, z	Point in the coordinate system of the research vessel.
$\alpha_i,\ i = 1, \ldots, I = 25$	Horizontal rotation angle for the beams.
$\Delta\alpha = 60°/24$	Resolution in α.
$\beta_j,\ j = 1, \ldots, J = 20$	Vertical rotation angle for the beams.
$\Delta\beta = 45°/19$	Resolution in β.
τ	Tilt angle of the sonar.
$\mathbf{d}_{i,j}$	Unit vector for the axis of maximum acoustic intensity of beam number (i, j),
$-\mathbf{e}_x = (-1, 0, 0)$	Unit vector in the negative direction of the x-axis.
$\mathbb{A}_{zy}(-\alpha_j, \beta_j)$	Rotation matrix for the z-y-rotation from vessel to beam.
$\mathbb{A}_{yz}(-\beta_j, \alpha_i)$	Rotation matrix for the y-z-rotation from beam to vessel.

Chapter 4, Interpretation of data.

Variable	Description
S_v	Logarithmic density of backscattering cross section in the volume V.
b	Cross sectional area of small bubbles of air representing the backscattering ability in a volume.
$B = 4\pi/b \cdot 10^{S_v/10}$	Linear S_v-values.
$(t, t + \Delta t)$	Arbitrary time interval.
τ_p	Duration of the acoustic pulse (ping) from the MS70 sonar.
h	Distance from the sonar to an arbitrary object.
$h' = h\%(c\tau_p/2)$	Distance for convenience.
$r_k,\ k = 1, \ldots, K = 1319$	Distance from the sonar of midpoints in voxels.
$\Delta r = c\tau_p/2$	Radial resolution.
$\alpha_i,\ i = 1, \ldots, I = 25$	Horizontal rotation angle for the beams.
$\Delta\alpha = 60°/24$	Resolution in α.
$\beta_j,\ j = 1, \ldots, J = 20$	Vertical rotation angle for the beams.
$\Delta\beta = 45°/19$	Resolution in β.
$z_{jk} = r_k \sin\beta_j$	Depth of spherical strip.
$V_{\text{sph.sct.}}(r_k)$	Volume of an open spherical sector of radius r_k and opening $(\sin(\beta_j + \Delta\beta/2), \sin(\beta_j - \Delta\beta/2))$.
V_{ijk}	Volume of voxel number (ijk).

Chapter 5, Noise.

Variable	Description
S_v	Logarithmic density of backscattering cross section in the volume V.
b	Cross sectional area of small bubbles of air representing the backscattering ability in a volume.
$B = 4\pi/b \cdot 10^{S_v/10}$	Linear S_v-values.
Y, Z and W	Stochastic variables in the HIB-algorithm.
C	Cut point for identifying high intensity beams (HIBs).
$q = \bar{Y}$	Empirical probability of having a B-value $> C$.
N	Total number of voxels examined by the HIB-algorithm.
$B_i,\ i = 1, \ldots, N$	B-value for voxel number i.
h	Minimum number of consecutive events $B_i > C$ along beams, classifying the sequence as HIB.
L	Length of beams.

Variable	Description
n	Length of the considered part of sequences of B-values $> C$.
s	Additional voxels in sequences of B-values $> C$.
N_B	Number of beams.
M	Maximum accepted number of sequences incorrectly classified as HIBs.
b	Overlap value for the replacement of HIBs.

Chapter 6, Backscattering from individual fish.

Variable	Description
S_v	Logarithmic density of backscattering cross section in the volume V.
b	Cross sectional area of small bubbles of air representing the backscattering ability in a volume.
$B = 4\pi/b \cdot 10^{S_v/10}$	Linear S_v-values.
$(t, t + \Delta t)$	Arbitrary time interval.
$(r, \theta, \phi) = (X, Y, Z)$	Point in the coordinate system of the vessel.
γ	Incident angle with respect to the transducer.
$\mathbf{X} = (X_X, Y_X, Z_X)$	Position of the fish.
$(r', \theta', \phi') = (X', Y', Z')$	Point in the coordinate system of the fish.
γ'	Incident angle with respect to the fish.
$\Omega = (\alpha^F, \beta^F)$	Orientation of the fish.
τ	Tilt angle of the swim bladder.
S	Length of the fish.
(a, b)	Rotations of the fish.
$\mathbf{v}$	Vector in the coordiane system of the vessel.
$\mathbf{v}'$	Vector in the coordiane system of the fish.
$\mathbb{A}_{zx}\left(\alpha^F - \pi/2, \pi/2 - \beta^F\right)$	Rotation matrix from the coordinate system of the vessel to the coordinate system of the fish.
$\mathbf{d} = (1, \theta, \phi)$	Unit direction vector of the fish in the coordinate system of the vessel.
$\mathbf{d}'_0 = -\mathbf{d}$	Unit direction vector of the vessel in the coordinate system of the fish.
$\mathbf{d}^\star$	Point vector for finding the angle of incident γ' with respect to the fish.

Variable	Description
$\mathbb{A}_\gamma$	Rotation matrix for finding the angle of incident γ' with respect to the fish.
$p\left(r', \gamma'\right)$	Acoustic pressure field from a line source or a circular piston.
ρ_0	Equilibrium density.
c	Speed of sound.
U_0	Particle speed amplitude.
ω	Angular frequency of the sound.
k	Wave number of the sound.
a	Radius of the line source (as a cylinder).
L	Length of the line source.
$\kappa_a = \cos\phi_a e^{-i(ka+\phi_a)}$	Constant involving the complex acoustic impedance.
ϕ_a	Argument to complex acoustic impedance for a spherical wave evaluated at $r = a$.
$H_F\left(\gamma'\right)$	Theoretical directional factor of the line source representing the fish.
$H_F(\theta', \phi')$	Empirical directional factor of the fish.
P	Acoustic pressure amplitude
$I = P^2/\rho_0 c$	Acoustic intensity.
$B_F(\theta', \phi')$	Empirical directional factor for the *acoustic intensity* of the fish.
$B_F(\gamma')$	Theoretical directional factor for the *acoustic intensity* of the fish.
$P_{\text{ax}}\left(r\right)$	Axial pressure of line source or a circular piston.
E	Acoutic energy striking the fish in the time interval Δt.
$\Pi = E/\Delta t$	Power of the sound scattered in the fish.
$I_F\left(r, \theta', \phi'\right)$	The acoustic intensity from the fish.
$I_{max}(r)$	Maximum intensity in the scattered sound from the fish (optimal direction).
$\psi(k, S) = \oint_{r=1} B(\theta', \phi', k, S)ds$	Scaling for integrated directional factor on r=1.
α	Absorption constant for acoustic intensity.
$I_T(r)$	Acoustic intensity from the transducer at the fish.
$A_s(Z_X, \Omega) = A_0\eta_c\eta_\Omega$	Cross sectional area of an object of air scattering an equal amount of sound as the fish.
A_0	Optimal cross sectional receiving area at depth $Z_X = 0$.
η_c	Depth compression factor.
η_Ω	Orientation factor or aspect factor.
$\sigma_0 = 4\pi A_0\eta_c\eta_\Omega/\psi$	Optimal scattering cross section.
f_1	First resonance frequency of the swim bladder.

Variable	Description
$c_{\text{swimbladder}}$	Speed of sound in the swim bladder.
ε	Coefficient linking squared fish length S^2 and A_0.
$V(Z_X)$	Volume of the swim bladder at depth Z_X.
V_0	Volume of the swim bladder at zero depth
$p(Z_X)$	Hydrostatic pressure at depth Z_X
p_0	Hydrostatic pressure at zero depth.
$a(Z_X)$	Radius of a cylindrical swim bladder at depth Z_X.
a_0	Radius of a cylindrical swim bladder at zero depth.
$L(Z_X)$	Length of a cylindrical swim bladder at depth Z_X.
L_0	Length of a cylindrical swim bladder at zero depth
g	Gravitational acceleration in Norway.
γ_a	Transverse compression factor.
γ_L	Longitudinal compression factor.
$\gamma_A = \gamma_a\gamma_L$	Cross sectional compression factor.
$\mathbf{h} = (X_h, Y_h, Z_h)$	Vector representing the length of the cylindrical part of a swim bladder.
$b = L/a$	Oblongness of the swim bladder.
$A(\alpha^F, \beta^F, \tau, \theta, \phi)$	Cross sectional area of the swim bladder.
J_1	First order Bessel function.
$I_T = I_T\left(r, \theta^T, \phi^T\right)$	Acoustic intensity from the transducer at the fish position.
θ^T and ϕ^T	Angles in the spherical coordinate system of the transducer.
$B_T(\theta^T, \phi^T) = [H_T(\theta^T, \phi^T)]^2$	Directional factor for the *acoustic intensity* of the transducer.
$B_T(\gamma) = [H_T(\gamma)]^2$	Theoretical directional factor for the *acoustic intensity* of the transducer.
I_0	Acoustic intensity at the distance 1 m from the transducer.
$I_E(S, \mathbf{X}, \Omega)$	Acoustic intensity in the echo at the receiver from the fish.
σ^2 and μ	Variance and expected value of a stochastic variable.
$v^2 = \sigma^2/\mu^2$	Squared coefficient of variation of a stochastic variable.
$\alpha_i,\ i = 1, \ldots, I = 25$	Horizontal rotation angle for the beams.
$\Delta\alpha = 60°/24$	Resolution in α.
$\beta_j,\ j = 1, \ldots, J = 20$	Vertical rotation angle for the beams.
$\Delta\beta = 45°/19$	Resolution in β.
$r_k,\ k = 1, \ldots, K = 1319$	Distance from the sonar of midpoints in voxels.
$\Delta r = c\tau_p/2$	Radial resolution.

Variable	Description
η_r	Factor for radial weighting.
$g(\gamma)$	Parabola approximation of the directional factor of the transducer.
ϵ	Coefficient in the parabola approximation of $B_T(\gamma)$.
S_{ijk}	Subvolume number (ijk).
γ_{max}	Maximum angle γ of a fish in subvolume S_{ijk}.
$F(\gamma)$ and $f(\gamma)$	Cumulative and probability density function of γ.
$v_S = \sigma_S/\mu_S$	Squared coefficient of variation of the length S of the fish.
$\lambda = \mu_S^2/\sigma_S^2$	Non-centrality parameter in the non-central chi-squared distribution of A_0.
k	Degrees of freedom in the non-central chi-squared distribution of A_0.
(A)	Factor in the sonar equation for absorption and attenuation.
(B)	Factor in the sonar equation for the beam pattern of the transducer.
(C)	Factor in the sonar equation for the product of beam pattern and aspect factor of the fish.
(D)	Factor in the sonar equation for the backscattering cross section.
(E)	Factor in the sonar equation for the depth compression.
(F)	Factor in the sonar equation radial weighting.
$\mu_A, \ldots, \mu_F$	Expected value of the 6 factors (A) through (F) in the sonar equation.
$\sigma_A^2, \ldots, \sigma_F^2$	Variance of the 6 factors (A) through (F) in the sonar equation.
$v_A^2, \ldots, v_F^2$	Squared coefficient of variation of the 6 factors (A) through (F) in the sonar equation.
$v_{A:F}$	Total squared coefficient of variation of the sonar equation.
$\bar{B}_F\left(\gamma'\right)$	Smoothed directional factor of line sources representing the fish.
σ_L^2	Variance of the line sources used to produce the smoothed directional factor $\bar{B}_F\left(\gamma'\right)$.
μ_L	Expected value of the line sources used to produce the smoothed directional factor $\bar{B}_F\left(\gamma'\right)$.
$\bar{\sigma}_{sp}$	Mean spherical backscattering cross section of the fish in a school.
n	Number of fish in subvolume S_{ijk}.
X	Superimposed acoustic pressure.
Y	Superimposed acoustic intensity.
A_l	Pressure amplitude of the l'th superimposed fish.
$\lambda_Y = \sum_l I_l$	Expected value of the acoustic intensity from superimposed fish.
μ_{α^F} and $\sigma_{\alpha^F}^2$	Expected value and variance when drawing the orientation angle α^F.

Chapter 7, Statistical analysis.

Variable	Description
S_v	Logarithmic density of backscattering cross section in the volume V.
b	Cross sectional area of small bubbles of air representing the backscattering ability in a volume.
$B = 4\pi/b \cdot 10^{S_v/10}$	Linear S_v-values.
(G)	Global coordinate system.
(V)	Coordinate system of the vessel.
(S)	Coordinate system of the school.
$D_p^v = (t_p, x_p^v, y_p^v, z_p^v, a_p^v, b_p^v, c_p^v)$	Time, position and orientation angles of the vessel for pings $p = 1, \ldots, P$.
$\mathbf{v}_G$	Position vector in (G).
$\mathbf{v}_V$	Position vector in (V).
$\mathbf{v}_S$	Position vector in (S).
$\mathbf{s} = (x_p^v, y_p^v, z_p^v)$	Vessel position at ping p.
$\mathbb{A}_{\mathrm{G}\to\mathrm{V}} = \mathbb{A}_{zy}(a_p^v, c_p^v)$	Rotation matrix from (G) to (V).
$\mathbb{A}_{\mathrm{V}\to\mathrm{G}} = \mathbb{A}_{yz}(-c_p^v, -a_p^v)$	Rotation matrix from (V) to (G).
$\mathbb{A}_{\mathrm{G}\to\mathrm{S}} = \mathbb{A}_{zx}(\theta_\xi - \pi/2, \pi/2 - \phi_\xi)$	Rotation matrix from (V) to (S).
$\mathbb{A}_{\mathrm{V}\to\mathrm{S}} = \mathbb{A}_{\mathrm{G}\to\mathrm{S}}\mathbb{A}_{\mathrm{V}\to\mathrm{G}}$	Rotation matrix from (G) to (S).
f, d and t	Variables in the flood-fill algorithm in (Balabanian et al., 2007).
$\xi = (\xi_1, \ldots, \xi_P)$ $p = 1, \ldots, P$	Center of mass of the school at the different pings.
V_{ijk}	Volume of voxel number (ijk).
B_{ijk}	B-value of voxel number (ijk).
v	Coefficient of variation.
$(r_{\mathrm{mid}}, \alpha_{\mathrm{mid}}, \beta_{\mathrm{mid}})$	Midpoints of voxels.
$\mathbf{p}$ and $\mathbf{q}$	Points in (G).
L_j	Line number j, running through $\mathbf{p}_j$ along the unit vector $\mathbf{u}_j$.
$\mathbf{d}$	Distance vector from $\mathbf{q}$ to L.
S_j	Sum of squared distances from $(\xi_1, \ldots, \xi_P)$ to line number j to be fitted to $(\xi_1, \ldots, \xi_P)$.
n^4	Number of lines to fitted to $(\xi_1, \ldots, \xi_P)$.
(θ_ξ, ϕ_ξ)	Angles for the direction of the school found from ξ, in the spherical global coordinate system (G).
$V_p^{(T)}$	Total volume of the school at ping p.
B_{pijk}	B-value number (i, j, k) for ping number p.

Variable	Description
$\sigma_p^{(T)} = \sum_{M_p} V_{ijk} B_{pijk}$	Total backscattering ability of the school at ping p.
$B_p^{(T)} = \sigma_p^{(T)} / V_p^{(T)}$	Ratio of total backscattering ability and total volume of the school at ping p.
$\bar{B}_p$	Empirical mean of all B-values of the school at ping p.
$\mathrm{Var}(B)_p$	Empirical variance of all B-values at ping p.
$\mathrm{Var}(B)_p / \bar{B}_p^2$	Empirical squared coefficient of variation of all B-values at ping p.
$\hat{\rho}_{ijp}(h)$	Empirical autocorrelation for lags h along beam number (i, j) for ping p.
$\mathbf{X} = X_1, \ldots, X_g$	Arbitrary random vector to be analyzed by principal component analysis (PCA).
$\mathbf{e}_1, \ldots, \mathbf{e}_g$	Eigenvectors of the covariance matrix of the arbitrary random variables $X_1, \ldots, X_g$.
$\lambda_1, \ldots, \lambda_g$	Eigenvalues of the covariance matrix of the arbitrary random variables $X_1, \ldots, X_g$.
$Y_i = e_{i1} X_1 + \ldots + e_{ig} X_g$	Principal component number i of $\mathbf{X}$, $i = 1, \ldots, g$.
$\xi_p^{(d)} = m_p + \zeta_p$	Centers of mass projected onto $\mathbf{e}_1$.
$m_p = v_\xi t_p$	Linear trend component of $\xi_p^{(d)}$.
v_ξ	speed of $\xi_p^{(d)}$.
ζ_p	Random fluctuations in $\xi_p^{(d)}$.
Z_p	Depth of the school at ping p, found from ξ_p.
M_p	The set voxels identified as belonging to the school at ping p.
$V^{(F)} = (\kappa S)^3$	Volume occupied by one fish.
$\bar{V}^{(F)}$	Mean volume occupied by one fish.
κ	Coefficient specific for each species.
$\bar{S}^2$	Mean squared length of all fish in the school.
$\bar{\sigma}_{sp} = \varepsilon \bar{S}^2$	Mean spherical backscattering cross section of all fish in the school.
ε	Coefficient specific for each species.
f	Frequency of the sound.
N_p	Number of fish in the school at ping p.
$\bar{I}$	Mean of $B_T\left(\theta^T, \phi^T\right) B_F\left(\theta', \phi'\right) \eta_\Omega \eta_c$ of all the fish in the school.
ν	Ratio of mean fish lengths $\bar{S}'$ and $\bar{S}$.
$(\theta_o'^p, \phi_o'^p)$	Direction of the *oblongness* of the school in (S) at ping p.
(θ_o^p, ϕ_o^p)	Direction of the *oblongness* of the school in (G) at ping p.
$(\bar{\theta}_o', \bar{\phi}_o')$	Mean direction of the *oblongness* of the school in (S) at ping p.
$(\bar{\theta}_o, \bar{\phi}_o)$	Mean direction of the *oblongness* of the school in (G) at ping p.
(S')	Coordinate system of the school rotated according to eigenvectors of projected midpoints.

Variable	Description
$\mathbb{A}_{\text{S}\to\text{S'}} = \mathbb{A}_{zx}(\bar{\theta}'_o - \pi/2, \bar{\phi}'_o - \pi/2)$	Rotation matrix from (S) to (S').
c^s	Roll angle of the school compared to horizontal, found from the eigenvectors of the projected midpoints of voxels.
L_S^p, W_S^p and H_S^p	Length, width and height of the school at ping p.
C_x^p, C_y^p and C_z^p	Degrees of centrality of the school in the x-, y- and z-direction at ping p.
$\hat{\rho}^{(T)}(h)$	Average autocorrelations of all beam of length > 40.
$(x_p^{(1)}, x_p^{(2)})$	Modified range of x-values.
c_q	Specification value of the modified range $(x_p^{(1)}, x_p^{(2)})$.
$q =$(LS)	Left half of the school.
$q =$(RS)	Right half of the school.
$q =$(T)	Tail part of the school (0,1/4).
$q =$(M)	Middle part of the school (1/4,3/4).
$q =$(F)	Front part of the school (3/4,1).
$q =$(L)	Lower half of the school.
$q =$(U)	Top half of the school.
$V_{p,q}^{(T)}$	Total volume of part q of the school at ping p, (q written without parenthesis).
$\sigma_{p,q}^{(T)} = \sum_{M_{p,q}} V_{ijk} B_{pijk}$	Total backscattering ability of part q of the school at ping p.
$B_{p,q}^{(T)} = \sigma_{p,q}^{(T)} / V_{p,q}^{(T)}$	Ratio of total backscattering ability and total volume of part q of the school, at ping p.
$\bar{B}_{p,q}$	Empirical mean of all B-values in part q of the school, at ping p.
$\text{Var}(B)_{p,q}$	Empirical variance of all B-values in part q of the school, at ping p.
$\text{Var}(B)_{p,q}/\bar{B}_{p,q}^2$	Empirical squared coefficient of variation of all B-values in part q of the school, at ping p.
$\hat{B}_{ijk}$	Moving average over 15 B-values along beam number (ijk).
σ_{fish}	Value representing the mean backscattering cross section from the fish in the school.
(S")	Coordinate system of the school rotated according to eigenvectors of the regenerated school.
N_p^S	Number of artificial fish in a spherical segment at ping p.

Chapter 8, Results.

Variable	Description
S_v	Logarithmic density of backscattering cross section in the volume V.
b	Cross sectional area of small bubbles of air representing the backscattering ability in a volume.
$B = 4\pi/b \cdot 10^{S_v/10}$	Linear S_v-values.
(G)	Global coordinate system.
(V)	Coordinate system of the vessel.
(S)	Coordinate system of the school.
$\xi = (\xi_1, \ldots, \xi_P)\ p = 1, \ldots, P$	Center of mass of the school at the different pings.
$\bar{Z}$	Mean depth of the school, found from ξ.
$(\theta_\xi, \phi_\xi)_{\text{acc}}$	Angles of the direction of the school found from ξ, by the accurate method.
$(\theta_\xi, \phi_\xi)_{\text{cru}}$	Angles of the direction of the school found from ξ, by the crude method.
$\bar{c}^s$	Mean roll angle of the school.

Some expressions.

MS70	Multibeam sonar manufactired by Simrad.
Ping	A three dimensional observation by the MS70 sonar.
IBM	Individual based model, concerning behaviour rules for individual fish in schools.
Segmentation	Indicator values deciding wether voxels are part of the school.
HIB	High intensity beam or a sequence of high intensity instrument noise.

Appendix C

Histograms of the different parts of the sonar equation from simulations.

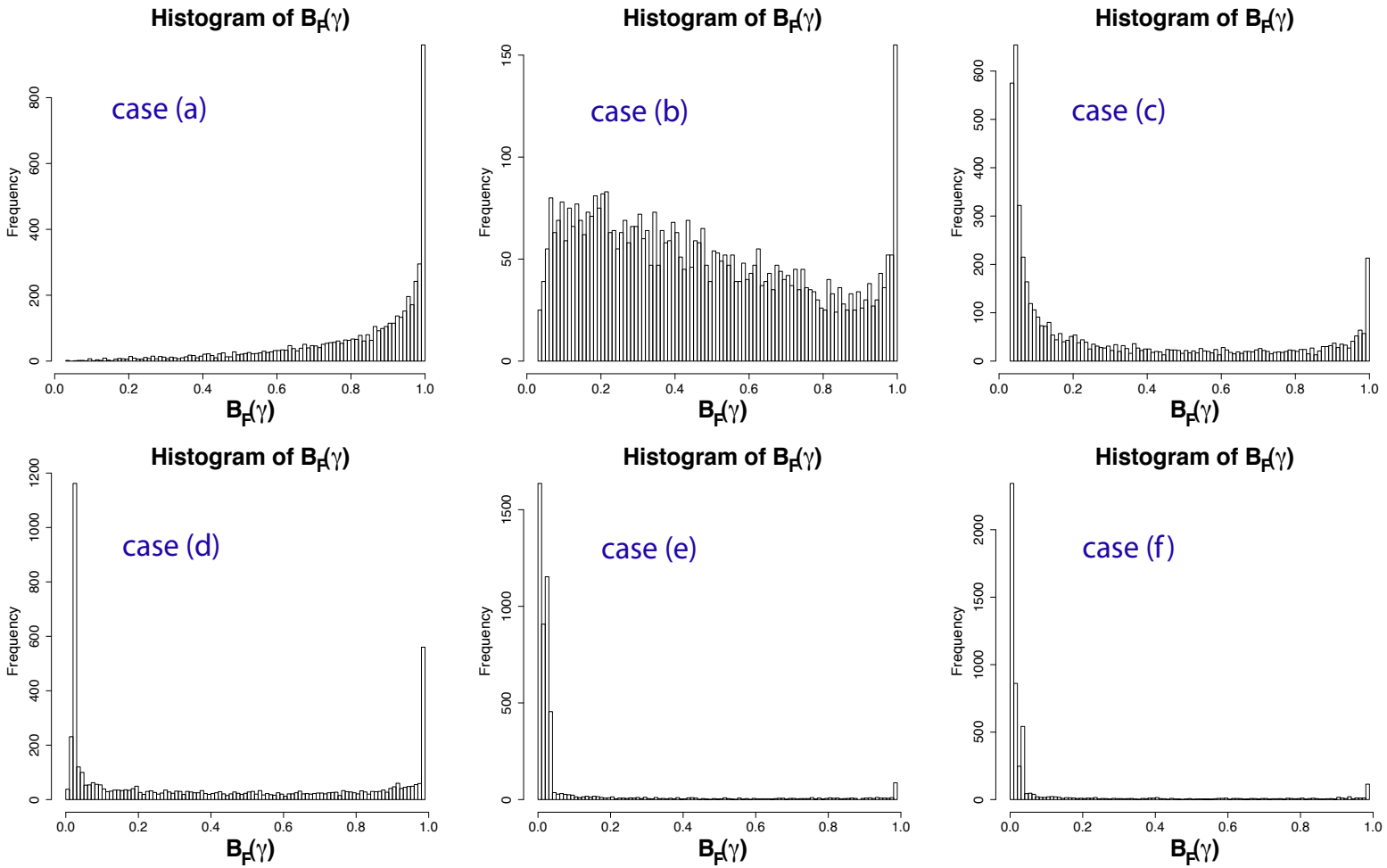

Figure C.1: Histogram of the directional factor $B_F(\gamma')$ in the direction of the transducer, of 5000 simulated fish with random size, position and orientation, as presented in chapter 6. The six plots are for the six situations in Table 6.3.2.

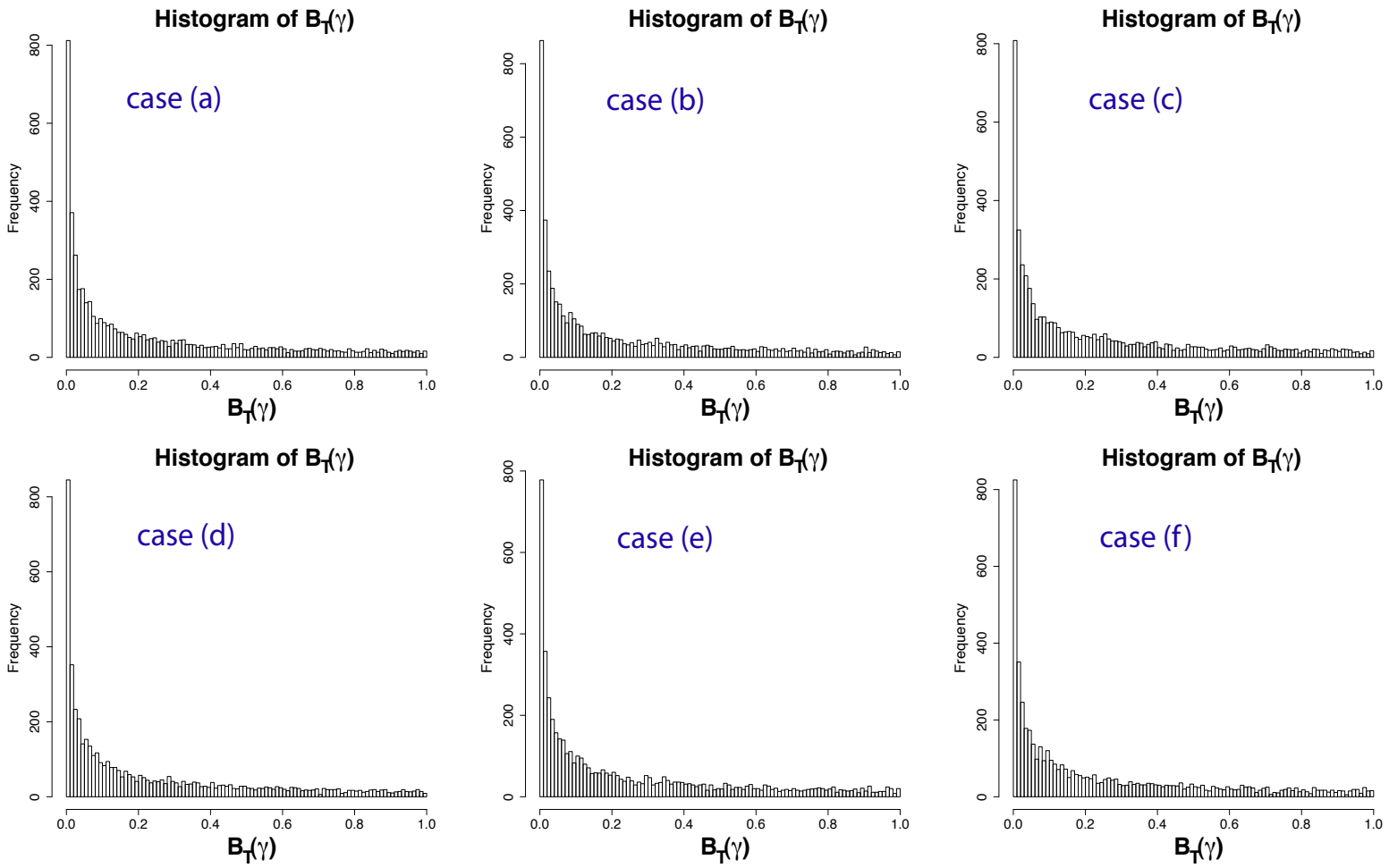

Figure C.2: Histogram of the directional factor $B_T(\gamma)$ in the direction of the fish, of 5000 simulated fish with random size, position and orientation, as presented in chapter 6. The six plots are for the six situations in Table 6.3.2.

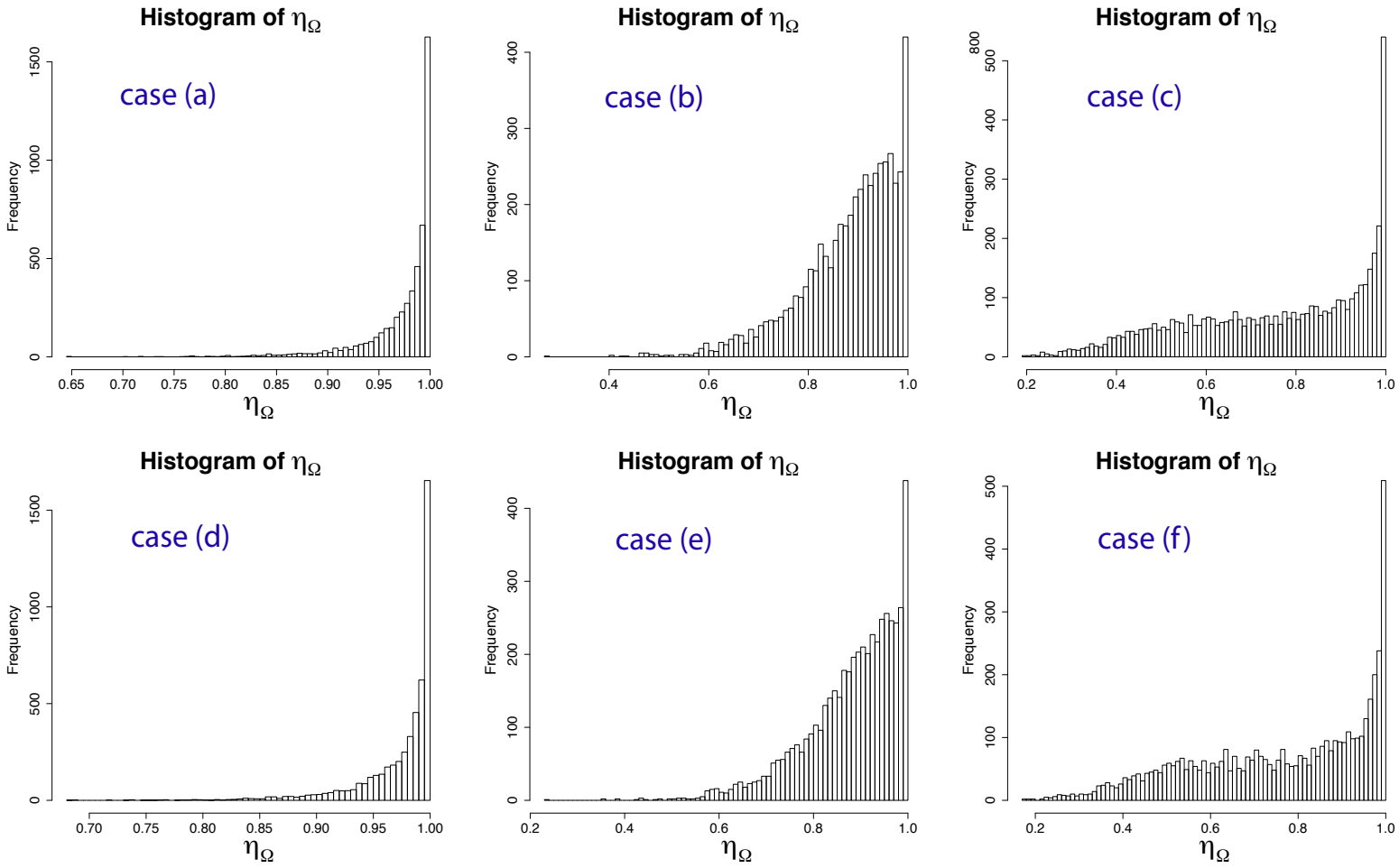

Figure C.3: Histogram of the aspect factor η_Ω of 5000 simulated fish, as seen from the transducer, having random size, position and orientation, as presented in chapter 6. The six plots are for the six situations in Table 6.3.2.

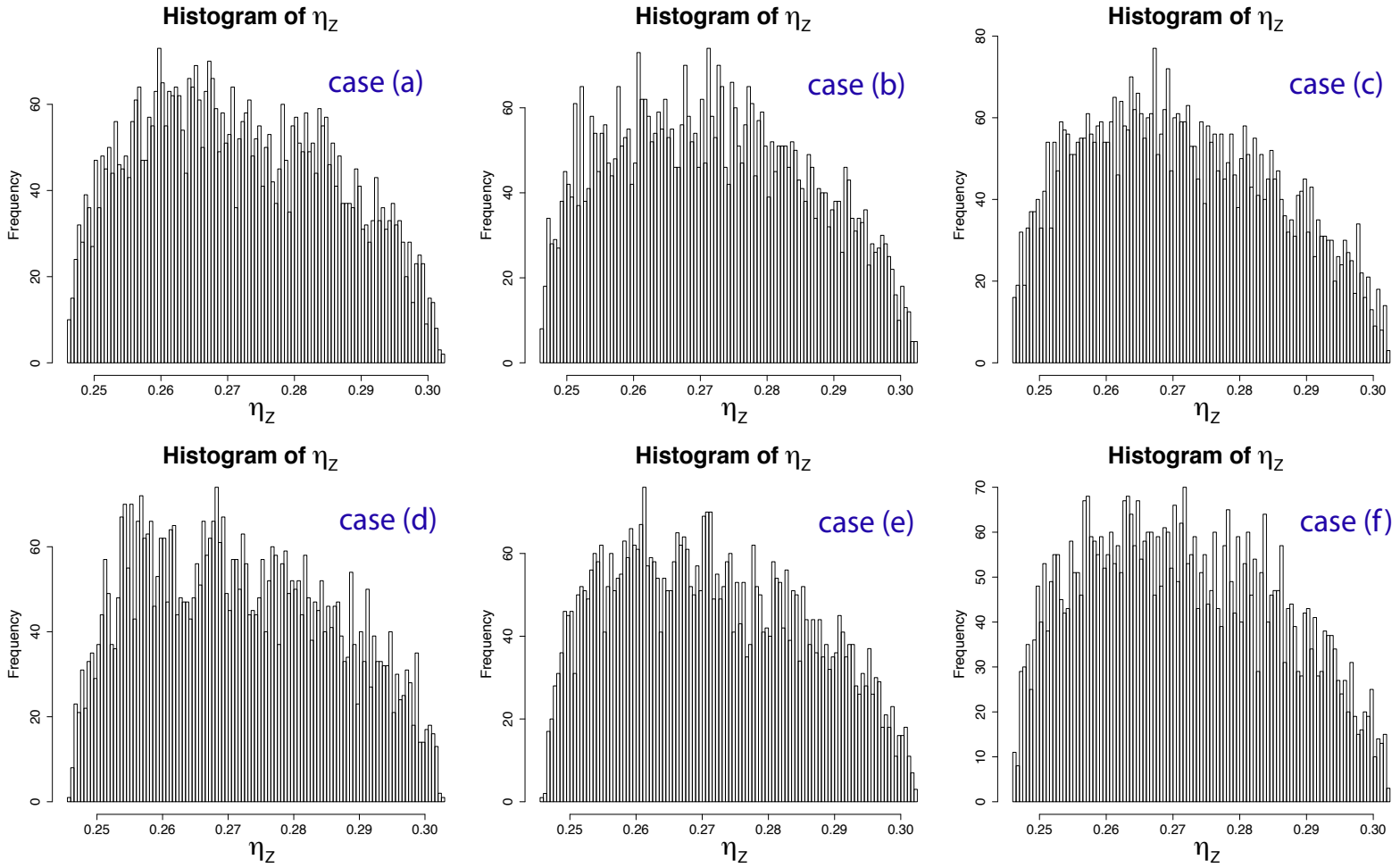

Figure C.4: Histogram of the depth factor η_Z of 5000 simulated fish with random size, position and orientation, as presented in chapter 6. The six plots are for the six situations in Table 6.3.2.

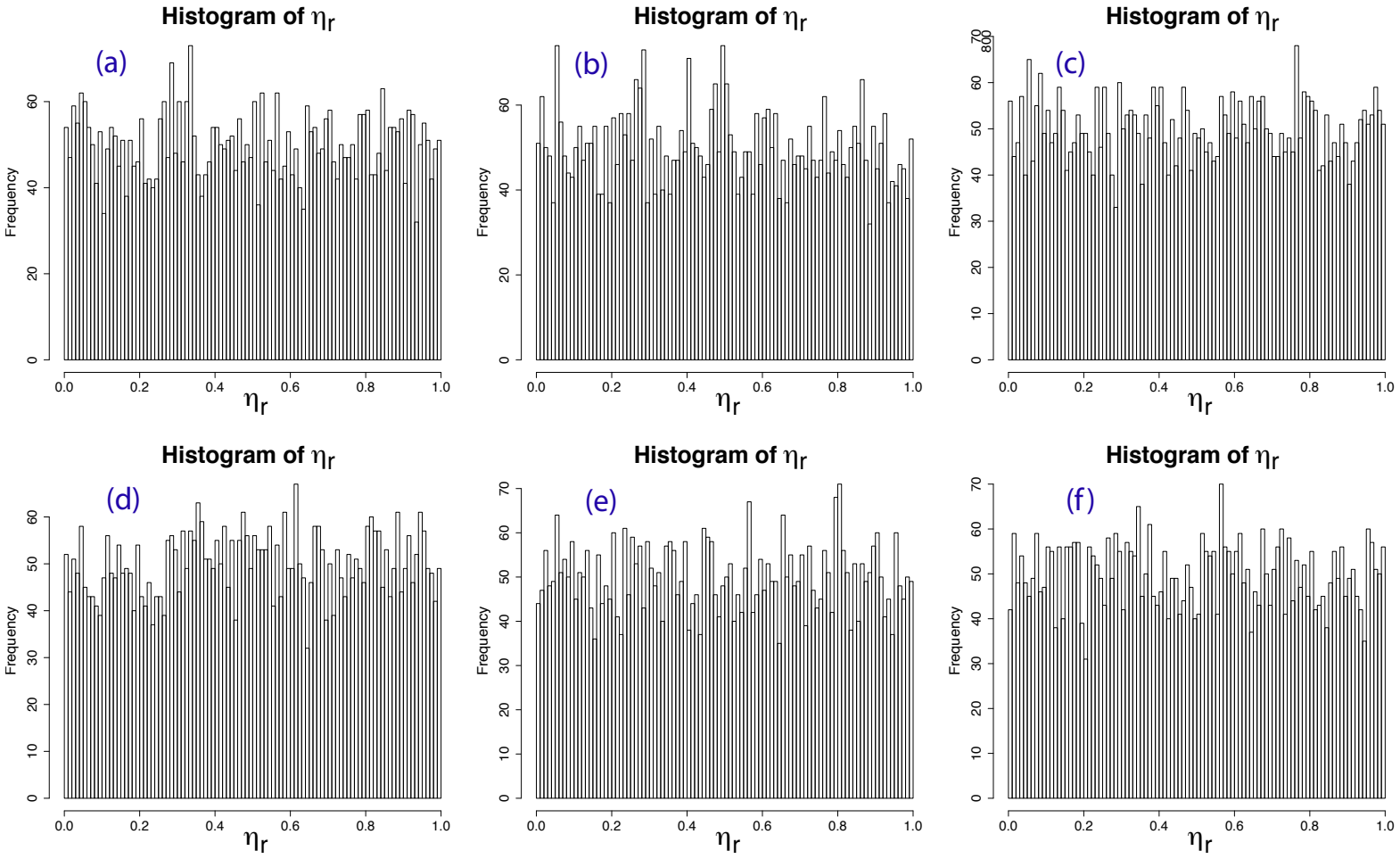

Figure C.5: Histogram of the radial overlap factor η_r of 5000 simulated fish with random size, position and orientation, as presented in chapter 6. The six plots are for the six situations in Table 6.3.2.

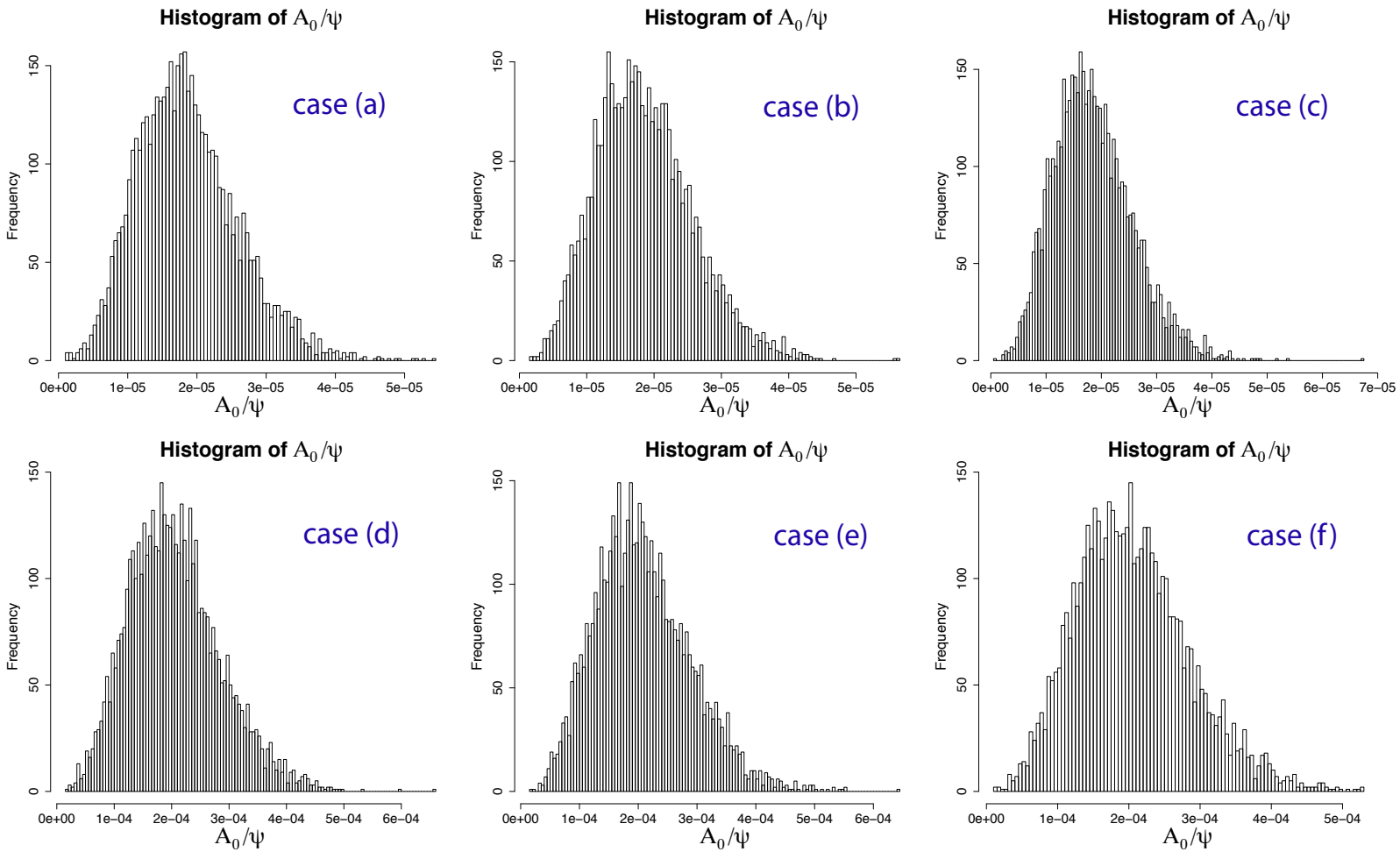

Figure C.6: Histogram of the backscattering cross sectional area at optimal incidence σ_0 of 5000 simulated fish with random size, position and orientation, as presented in chapter 6. The six plots are for the six situations in Table 6.3.2.

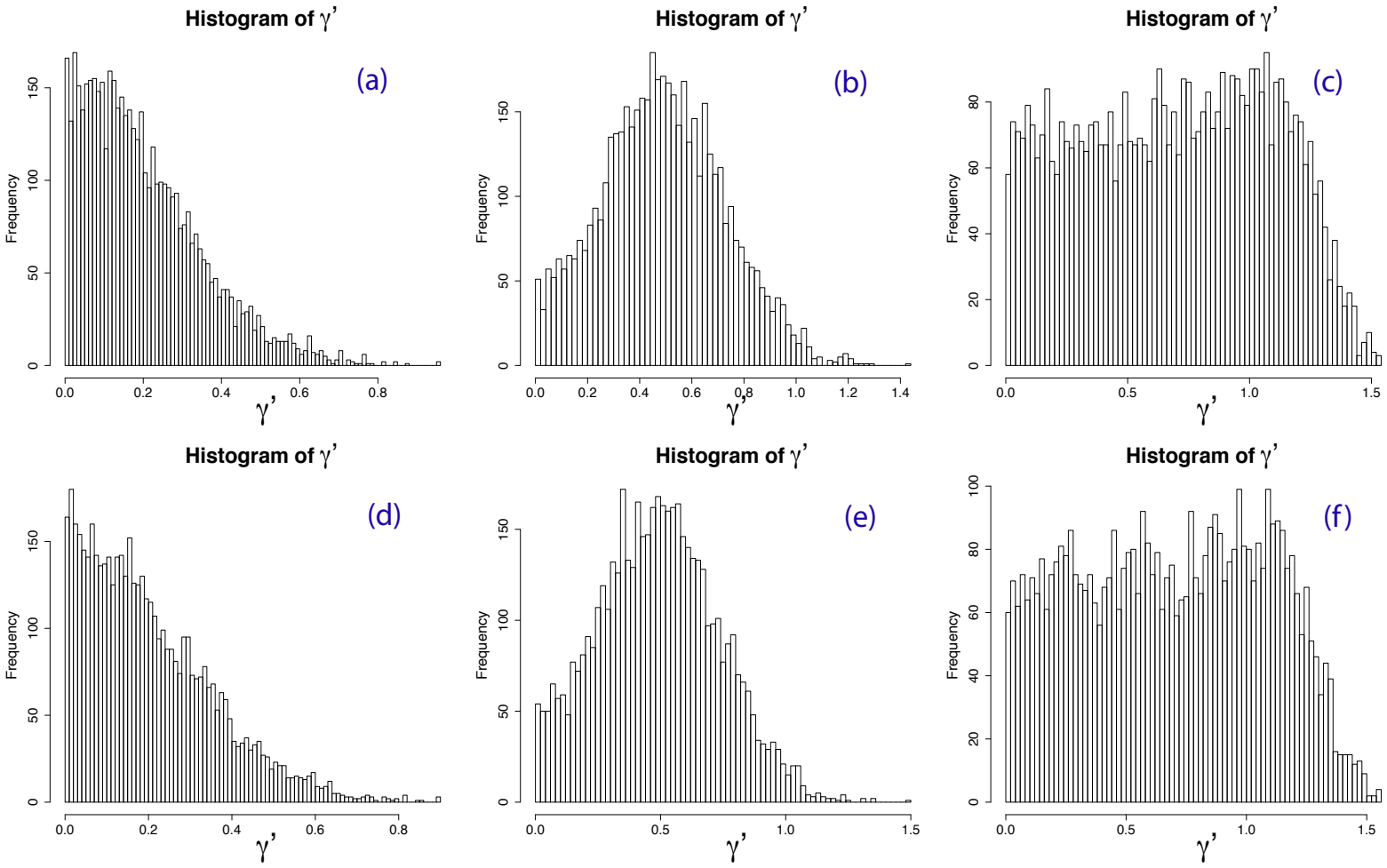

Figure C.7: Histogram of the angle of incidence γ' of the direction to the transducer with respect to the fish, of 5000 simulated fish with random size, position and orientation, as presented in chapter 6. The six plots are for the six situations in Table 6.3.2.

Bibliography

Simrad Horten AS. Simrad ms70 scientific multibeam sonar system. Technical report, Simrad Horten AS, 2006.

Jean-Paul Balabanian, Ivan Viola, Egil Ona, Ruben Patel, and Eduard Gröller. Sonar explorer: A new tool for visualization of fish schools from 3d sonar data. *Eurographics/ IEEE-VGTC Symposium on Visualization*, 2007.

Dirk Bumann, Jens Krause, and Dan Rubenstein. Mortality risk of spatial positions in animal groups: the danger of being in the front. *Behaviour*, 134(13-14):1063–1076, 1997.

Inge Eliassen, Yngve Heggelund, Daniel Patel, and Kjell Røang. Utvikling av ekstra moduler for ekkolodd ek60 fra simrad - versjon 2. Technical report, University of Bergen, Norway, 2003.

François Gerlotto, Marc Soria, and Pierre Fréon. From two dimensions to three: the use of multibeam sonar for a new approach in fisheries acoustics. *Canadian Journal of Fisheries and Aquatic Sciences*, 56:6–12, 1999.

Natalia Gorska and Egil Ona. Modelling the acoustic effect of swimbladder compression in herring. *Journal of Marine Science*, (60): 548–554, 2003a.

Natalia Gorska and Egil Ona. Modelling the effect of swimbladder compression on the acoustic backscattering from herring at normal or near-normal dorsal incidences. 2003b.

Charlotte K. Hemelrijk and Hanspeter Kunz. Density distribution and size sorting in fish schools: an individual-based model. *Behavioral Ecology*, 16(1):178–187, 2004.

Andreas Huth and Christian Wissel. The simulation of the movement of fish schools. *Journal of theoretical biology*, 156:365–385, 1992.

Jens Krause, Daniel J. Hoare, Darren Croft, James Lawrence, Ashley Ward, Greame D. Ruxton, Jean-Guy J. Godin, and Richard James. Fish shoal composition: mechanisms and constraints. *Proceedings of the Royal Society of London Series B-biological Sciences*, 267(4): 2011–2017, 1987.

Richard H. Love. An empirical equation for the determination of the maximum side-aspect target strength of an individual fish. *The Journal of the Acoustical Society of America*, 46:746–752, 1969.

Richard H. Love. Target strength of an individual fish at any aspect. *The Journal of the Acoustical Society of America*, 62(6):1397–1402, 1977.

David N. MacLennan, Paul G. Fernandes, and John Dalen. A consistent approach to definitions and symbols in fisheries acoustics. *ICES Journal of Marine Science*, 59:365–369, 2002.

Vincent Mirabet, Pierre Augera, and Christophe Lett. Spatial structures in simulations of animal grouping. *Ecological Modelling*, 201 (3–4):468–476, 2007.

Egil Ona. An expanded target-strength relationship for herring. *ICES Journal of Marine Science*, 60(3):493–499, 2003.

Egil Ona. Physiological factors causing natural variations in acoustic target strength of fish. *Journal of the Marine Biological Association of the United Kingdom*, (70):107–127, 1990.

Albert Eide Parr. A contribution to the theoretical analysis of the schooling behavior of fishes. *Occational papers of Birmingham Oceanographic College*, 1:1–32, 1927.

Julia K. Parrish, Steven V. Viscido, and Daniel Grünbaum. Self-organized fish schools: An examination of emergent properties. *Biological Bulletin*, 202(3):296–305, 2002.

T. J. Pitcher. Some ecological consequences of fish school volumes. *Freshwater Biology*, 10:539–544, 1980.

T.J. Pitcher and B.L. Partridge. Fish school density and volume. *Marine Biology*, 54(4):383–394, 1979.

Craig W. Reynolds. Flocks, herds, and schools: A distributed behavioral model. *Computer Graphics*, 21(4):25–34, 1987.

T. K. Stanton. Volume scattering: Echo peak pdf. *The Journal of the Acoustical Society of America*, 77:1358–1366, 1984.

R.L. Towler, J.M. Jech, and J.K. Horne. Visualizing fish movement, behaviour, and acoustic backscatter. *Aquatic Living Resources*, (16):277–282, 2003.